

*Digital Comprehensive Summaries of Uppsala Dissertations  
from the Faculty of Science and Technology 2287*

# Computational studies on 2D and 3D amorphous solids

*Investigation of structure-property relationship*

EMEL GÜRBÜZ



ACTA UNIVERSITATIS  
UPSALIENSIS  
2023

ISSN 1651-6214  
ISBN 978-91-513-1855-4  
urn:nbn:se:uu:diva-508514



UPPSALA  
UNIVERSITET

Dissertation presented at Uppsala University to be publicly examined in Room 4101, Ångströmlaboratoriet, Lägerhyddsvägen 1, Uppsala, Monday, 25 September 2023 at 13:15 for the degree of Doctor of Philosophy. The examination will be conducted in English. Faculty examiner: Professor Andreas Larsson (Department of Engineering Sciences and Mathematics, Luleå University of Technology).

### **Abstract**

Gürbüz, E. 2023. Computational studies on 2D and 3D amorphous solids. Investigation of structure-property relationship. *Digital Comprehensive Summaries of Uppsala Dissertations from the Faculty of Science and Technology* 2287. 101 pp. Uppsala: Acta Universitatis Upsaliensis. ISBN 978-91-513-1855-4.

Amorphous materials represent a large and diverse family, with many questions still remaining unanswered regarding their structure-property relationship. The structural complexity of these materials poses challenges for simulations in contrast to crystalline materials where density functional theory (DFT) can be used easily by exploiting the translation symmetry. The use of DFT often becomes intractable due to the large system sizes required for simulating amorphous materials. In this thesis, amorphous metallic glasses and 2D materials were comprehensively investigated through the combined application of classical molecular dynamics simulations (CMD) and DFT. Glassy structures were successfully generated followed by the study of thermal and vibrational properties using CMD, while DFT was used to explore their electronic, magnetic, and optical characteristics. The results demonstrated that nanostructured voids in metallic glasses can decrease the lattice thermal conductivity. The relationships between structure, local orderings, and material properties such as magnetism and superconductivity are also examined and analyzed in this thesis. Furthermore, the unique and intriguing structure-dependent properties in low-dimensional (2D) and layered structures have been comprehensively studied that could be potentially used in future functional devices. In summary, this thesis opens up a number of avenues to explore functional amorphous materials for various technological applications.

*Keywords:* Amorphous solids, Metallic glasses, Classical molecular dynamics simulations, Thermal transport, Density functional theory, 2D glasses, Vibrational properties, Magnetism, Optical properties

*Emel Gürbüz, Department of Physics and Astronomy, Materials Theory, Box 516, Uppsala University, SE-751 20 Uppsala, Sweden.*

© Emel Gürbüz 2023

ISSN 1651-6214

ISBN 978-91-513-1855-4

URN urn:nbn:se:uu:diva-508514 (<http://urn.kb.se/resolve?urn=urn:nbn:se:uu:diva-508514>)

*Dedicated to my beloved son KONT,  
my wise little man,  
my greatest teacher,  
my dearest friend, and  
my continuous unwavering support.  
I'll love you always and forever...*



# List of papers

This thesis is based on the following papers, which are referred to in the text by their Roman numerals.

- I **Tuning of lattice thermal conductivity of amorphous  $\text{Fe}_{0.85}\text{Zr}_{0.15}$  by nanostructured voids, pressure and temperature**  
E. Gürbüz and B. Sanyal  
*Journal of Non-Crystalline Solids*, 616, 122430 (2023)
- II **Structural and magnetic properties of amorphous  $\text{Co}_x\text{Zr}_{100-x}$  films**  
P. Rani, V. Kurichenko, E. Gürbüz, B. Sanyal, B. Hjörvarsson, and G. Andersson  
*In revision in Phys. Rev. B*
- III **Superconductivity in amorphous  $\text{Mo}_x\text{Ge}_{100-x}$ : insights from first principles**  
E. Gürbüz, I. Miranda, D. Karmakar, B. Sanyal, and O. Eriksson  
*Manuscript*
- IV **Observation of defect density dependent elastic modulus of graphene**  
H. Li, E. Gürbüz, S. Haldar, T. Hussain, X. Zheng, X. Ye, S. W. Makumi, T. Duan, S. H. M. Jafri, L. Daukiya, L. Simon, A. Karton, B. Sanyal and K. Leifer  
*Applied Physics Letters*, 123, 053102 (2023)
- V **Systematic study of amorphous 2D graphene, silicene and silicon carbide: Investigation of structural, electronic, optical and vibrational properties**  
E. Gürbüz and B. Sanyal  
*arXiv:2305.08134 (2023)*, in revision in *Phys. Rev. B*

Reprints were made with permission from the publishers.

## Statement on my contribution:

- In my first paper, I mainly took part in conceptualization, discussions, analysis of results, writing the original draft, managing the replies to the referees, and handling its submission.
- In my second paper, I performed all theoretical calculations and took part in conceptualization, discussions, analysis of results, writing the original draft, and managing the replies to the referees for the theoretical part.
- In my third paper, I took part in conceptualization, discussions, analysis of results, and writing the original draft for the amorphous part.
- In my fourth paper, I performed all theoretical calculations and took part in conceptualization, discussions, analysis of results, and writing the original draft for the theoretical part.
- In my fifth paper, I did calculations and took part in conceptualization, discussions, analysis of results, writing the original draft and managing the replies to the referees, and handling its submission.

# List of publications not included in the thesis

- I **Spin-polarized two-dimensional electron/hole gas at the interface of nonmagnetic semiconducting half-Heusler compounds: Modified Slater-Pauling rule for half-metallicity at the interface**  
E. Gürbüz, S. Ghosh, E. Şaşıoğlu, I. Galanakis, I. Mertig, and B. Sanyal  
*Phys. Rev. Materials*, 7, 054405 (2023)
- II **First-principles prediction of energy band gaps in 18-valence electron semiconducting half-Heusler compounds: Exploring the role of exchange and correlation**  
E. Gürbüz, M. Tas, E. Şaşıoğlu, I. Mertig, B. Sanyal, and I. Galanakis  
*Manuscript*





# Contents

Part I: Introduction and Theoretical Background .....	11
1 Introduction .....	13
2 Theoretical Background .....	16
2.1 Glass .....	16
2.1.1 Radial Distribution Function .....	18
2.1.2 Angular Distribution Function .....	19
2.1.3 Voronoi Tessellation .....	20
2.1.4 Ring Statistics .....	20
2.2 Molecular Dynamics Simulations .....	21
2.2.1 Thermostats .....	23
2.2.2 Berendsen Thermostat .....	23
2.2.3 Embedded Atom Method Potential .....	24
2.2.4 Tersoff Potential .....	25
2.2.5 Lattice Thermal Conductivity .....	26
2.2.6 Vibrational Density of States .....	27
2.3 Density Functional Theory .....	28
2.3.1 Kohn-Sham Equations .....	29
2.3.2 Exchange Correlation Energy .....	30
2.3.3 Bloch Equation and k-point Sampling .....	31
2.3.4 Pseudopotentials and PAW Method .....	32
2.3.5 Structure Definition .....	35
2.3.6 Van der Waals Interaction .....	35
2.3.7 Optical Properties .....	36
Part II: Summary of the Results .....	39
3 Tuning the Lattice Thermal Conductivity of Metallic Glasses .....	41
3.1 Structural Analysis .....	41
3.2 Nanostructuring Stable Voids .....	44
3.3 Lattice Thermal Conductivity .....	44
3.4 Vibrational Properties .....	48
3.5 Temperature and Pressure Effect on Lattice Thermal Conductivity .....	48
3.6 Temperature and Pressure Effect on Vibrational Properties of MGNV .....	52

3.7	Conclusion of Paper I	53
4	Structure Dependant Magnetic Properties of Amorphous $\text{Co}_x\text{Zr}_{100-x}$ films	55
4.1	Structural Analysis of $\text{Co}_x\text{Zr}_{100-x}$ Films	55
4.2	Magnetic Properties of $\text{Co}_x\text{Zr}_{100-x}$ Films	56
4.3	Conclusion of Paper II	57
5	Superconductivity of Amorphous $\text{Mo}_x\text{Ge}_{100-x}$ systems	59
5.1	Structural Modelling and Vibrational Analysis of $\text{Mo}_x\text{Ge}_{100-x}$ Systems	59
5.2	Superconductivity in Amorphous $\text{Mo}_x\text{Ge}_{100-x}$	62
5.3	Conclusion of Paper III	63
6	Amorphous Graphene Flake	64
6.1	Defect Density Dependent Elastic modulus of Graphene	64
6.2	Amorphous Graphene and Binding Energy	64
6.3	Conclusion of Paper IV	67
7	Systematic Atomistic Study of Amorphous 2D- Graphene, Silicene and Silicon Carbide	68
7.1	Structural Properties	68
7.2	Electronic Properties	69
7.3	Layered 2D Amorphous Structures: Bilayer, Trilayer	70
7.4	Optical Properties	71
7.5	Thermal Conductivity and Vibrational Properties	73
7.6	Conclusion of Paper V	75
	Part III: Final Summaries & Remarks	77
8	Conclusion and Outlook	79
9	Popular science summary	81
10	Populärvetenskaplig sammanfattning	84
11	Populer Bilim Özeti	87
12	Acknowledgements	90
	Bibliography	92

Part I:  
Introduction and Theoretical Background



# 1. Introduction

Amorphous materials, like silica, have captivated humanity for centuries, serving various purposes such as cutting, ornamentation, and construction. Remarkably, remnants of iron-rich siliceous glassy materials, billions of years old, were retrieved from the moon during the Apollo missions [1]. In a breathtaking discovery, Bouchy et al. unveiled the existence of an exoplanet called “*HD 189733 b*”, situated a staggering 64.5 light-years away from Earth, where molten glass rains from the skies [2, 3]. However, these enigmatic materials possess intricate structures that defy the ordered patterns of their crystalline counterparts. It was in 1932 that Zachariasen revolutionized our comprehension of glass by establishing a fundamental connection between its composition and structure [1, 4]. Nevertheless, verifying Zachariasen’s proposed structure remained elusive for decades due to the ineffectiveness of X-ray diffraction, the conventional method for determining material structure in the case of glasses and amorphous materials. It was only in 2012 that the breakthrough finally arrived, allowing precise atomic positioning within these intriguing substances [5, 6, 7]. The profound implications of this research extend beyond the realm of scientific curiosity, holding the potential to revolutionize the semiconductor field by enabling the production of amorphous silica with unprecedented precision and accelerating the discovery of novel and more potent catalysts. However, the journey toward understanding and manipulating these materials began much earlier than in 2012.

In 1959, a team of researchers at Caltech experimentally confirmed the production of the first metallic glass alloy with a composition of  $\text{Au}_{75}\text{Si}_{25}$  through splat quenching [8]. However, it was the first metallic glass (MG) and its production was expensive. In the 90s, cheaper binary metallic glasses (BMG) that included one of the excellent glass former, Zr, were discovered. It was mixed with cheaper ferrous materials such as iron (Fe), nickel (Ni), and chromium (Cr) to decrease the production cost and to open up their industrial usage such as those involving magnetic cycling where MGs exhibit smaller energy losses [8, 9, 10, 11, 12]. BMG have improved properties such as greater hardness, strength, and corrosion resistance, while still being easy to process. Additionally, their production costs are comparable to those of stainless steel [13].

Moreover, disordered materials have low thermal conductivity due to the localized nature of their heat carriers, making them useful in applications such as wearable electronics where flexibility and low heat transfer are desirable [14, 15, 16]. Amorphous semiconductors based on silicon are even being considered for use in advanced AI chips, as they may be better able to manage heat

dissipation [14, 17, 18]. Amorphous semimetallic and semiconductor materials may be also suitable for use in thermoelectric applications [19]. Metallic glasses and glassy alloys, which are often used in these applications, have been shown to have thermal conductivity below 9 W/Km, with lattice thermal conductivity below 2 W/Km [20, 21, 22]. It has been shown that Zr-based metallic glass thin films, when used in conjunction with an AgSbTe<sub>2</sub> substrate, can serve as an effective diffusion barrier [21]. Zr-based metallic glasses are good candidates to maintain a balance between the electronic component and thermoelectric materials in thermoelectric modules to increase the device efficiency.

Additionally, variations in local composition can affect atomic interactions, leading to changes in short-to-medium range structural order during the growth process of magnetic amorphous structures [23]. CoZr-based metallic glasses' saturation magnetization and magnetic ordering temperature were found to increase in a linear fashion with the Co content, starting from zero at a critical concentration that usually falls within the range of 40 - 60 at. % [24, 23]. Furthermore, the superconductivity of amorphous MoGe structures has been experimentally observed to be concentration-dependent [25, 26].

In the past decade, many stable two-dimensional (2D) amorphous inorganic materials with atomic layer thickness, such as amorphous-C, amorphous-BP, amorphous-TMD, amorphous-BN, amorphous-MoS<sub>2</sub>, etc., have been synthesized successfully with different techniques such as exfoliation, electron irradiation, chemical vapor deposition (CVD), or physical vapor deposition (PVD) [27, 28, 29, 30, 31, 32, 33, 34, 35, 36]. While some 2D amorphous structures have been synthesized, their characteristics and structures are not as well known as those of 2D crystalline materials. Molecular dynamics simulations have made it possible to predict low dimensional amorphous structures, such as amorphous-graphene [37, 38, 28, 39, 40, 41, 42], amorphous-silicene [43, 44, 45, 46, 47, 48], amorphous-silicon carbide [49, 50, 51], amorphous-germanene [52], amorphous-BN [53], etc. These simulations provide a deeper understanding of how the amorphous structure affects mechanical, thermal, and electronic properties. These low-dimensional amorphous materials, with their known and yet-to-be-discovered properties, can be used in various applications such as thermoelectric and thermal coatings, electronics, optoelectronics, and more.

Even though MG and 2D amorphous structures have been extensively investigated, their structure-dependent properties need to be enlightened. On the other hand, the reproducibility of experimental and theoretical results is only possible in statistical averages due to their complex structures [54]. Despite this limitation, classical molecular dynamics simulations (CMD) and density functional theory (DFT) remain accurate tools for studying amorphous structures. In this thesis, we use realistic modeling within the computational limits to analyze the structure-dependent properties of glass. Papers I, II, and III present our results on 3D amorphous metallic glasses. Paper I focuses

on  $\text{Fe}_{85}\text{Zr}_{15}$  MG, a non-magnetic and thermally low conductor. Tuning its lattice thermal conductivity is discussed from both a structural perspective and in terms of systems with nanostructured voids. Paper II investigates the concentration-dependent magnetization of  $\text{Co}_x\text{Zr}_{100-x}$  MG by incorporating the effects of local orderings. Paper III concludes the MG section by discussing the dependence of  $\text{Mo}_x\text{Ge}_{100-x}$ 's superconductivity on its structure and composition. Papers IV and V explore the properties of low-dimensional (2D) amorphous structures. Paper IV explains the experimentally observed decrease in graphene's elastic modulus with defect density by studying the binding energy change from crystal to amorphous structures. This study sheds light on graphene's mechanical properties. Paper V examines the structure-dependent thermal, vibrational, electronic, and optical properties of 2D amorphous graphene, silicene, and silicon carbide. They can serve as more durable, efficient, and cost-effective alternative materials to crystalline materials in functional devices with their structure-specific and tunable properties in the near future.

## 2. Theoretical Background

In this chapter, the theoretical foundation for the study is established, with a focus on essential concepts related to glass and molecular dynamics simulations, as well as a delve into density functional theory. The examination of the structure-dependent properties of glass begins with a discussion of the production and characterization of glassy systems. The glasses were produced by using molecular dynamics simulations which is a powerful computational technique for studying the behavior of atoms and molecules over time. Within this context, various thermostats are used to control the system's temperature, and different potential models are discussed. Subsequently, techniques for evaluating properties such as lattice thermal conductivity and the vibrational density of states are reviewed. Afterward, the background of density functional theory is investigated, which is used as a quantum mechanical method for studying the electronic structure and optical properties of materials. This chapter provides a solid foundation for the rest of the thesis by presenting a comprehensive theoretical background that paves the way for the investigations and analyses to come.

### 2.1 Glass

The process of glass formation can be likened to a time-sensitive endeavor, governed by thermodynamics. As the liquid is cooled below its melting temperature ( $T_m$ ), the countdown starts. As the temperature of the supercooled liquid drops, there is a concomitant drop in both its enthalpy and volume. When the glass transition temperature ( $T_G$ ), is reached, the atoms in the liquid become densely packed, inhibiting their ability to rearrange. This results in a glassy state where the system exhibits solids behavior, despite the presence of a frozen liquid-like disorder in its structure. To overcome the nucleation and growth of a crystalline phase, the liquid has to rapidly supercool from melting temperature  $T_m$ , to  $T_G$ . Rapid cooling results in glass structures resembling high-temperature liquids, due to entrapment at higher energy landscape levels. Even the slowest cooling rates result in entrapment at levels significantly higher than the lowest energy dip [55, 56, 57]. Metals, bound by conduction-band electrons that are freely shared, have no orientational requirement and only need to adopt translational order to crystallize. Consequently, supercooled metals tend to crystallize rapidly. However, specific metallic alloys



exhibit a significantly reduced tendency to crystallize compared to pure metals. Some of these alloys are composed of metal-metal combinations, including elements such as zirconium, copper, iron, and nickel. Others incorporate metals with near-metalloids like silicon, carbon, and phosphorus. This discovery started the rapidly expanding new category of materials referred to as metallic glasses (MG) [55]. The first MG ( $\text{Au}_{75}\text{Si}_{25}$ ), with a thickness of approximately  $10\text{ }\mu\text{m}$ , was produced at very high cooling rates of  $10^5 - 10^6\text{ K/s}$ . However, by carefully selecting and adjusting the composition of constituent elements, it is possible to create alloys with enhanced glass-forming ability (GFA). This allows for the mass production of MG using slower cooling rates and increased stability at room temperature [54, 58]. MG exhibit exceptional hardness and strength, rendering them highly desirable for use in applications where these properties are crucial. The mechanical properties of MG are known to be closely linked to the chemical and physical properties of their constituent elements. Variations in the chemical composition of MG result in significant differences in mechanical performance, such as strength and ductility, indicating an inherent connection between their mechanical properties and atomic, electronic structures [11]. Since amorphous materials lack long-range order, explanations for many phenomena, including mechanical and low thermal conductivity, depend on atoms' short-range ordering (SRO) and medium-range ordering (MRO) in the structure [59]. Classical molecular dynamics simulations (CMD) are significant tools for producing and calculating the equilibrium and non-equilibrium properties of materials of glasses and MG with the capability of involving millions of atoms. However, the time and length scales used in molecular dynamics simulations are usually much different from those used in laboratory experiments. CMD simulations can be performed by defining an interatomic potential, such as empirical potentials produced by fitting to experimental data [60, 61]. However, the most accurate approach to determining interatomic forces is through the use of first-principles calculations, whereas First Principles Molecular dynamics (FPMD) has limitations on the number of atoms and simulation time [62]. Both methods have their advantages and disadvantages in producing and calculating the properties of glasses. A benchmark calculation can be performed for both systems by employing a carefully selected cooling procedure that is fast enough to accurately produce the structural properties and the number of atoms in the simulation box. This can help produce the optimal glass structure and enable calculation using both methods through the use of transferable glass structures between them. In Fig. 2.1, we show a cooling procedure to produce a glass system that can be performed with both methods. In this thesis, *Large-scale Atomic/Molecular Massively Parallel Simulator* (LAMMPS) [63] was used for CMD calculations, and *Vienna Ab initio Simulations Package* (VASP) [64] was used for density functional theory calculations, including FPMD.

Characterization of the produced glass reveals its properties. The produced glass can be characterized using structural analysis methods such as radial and

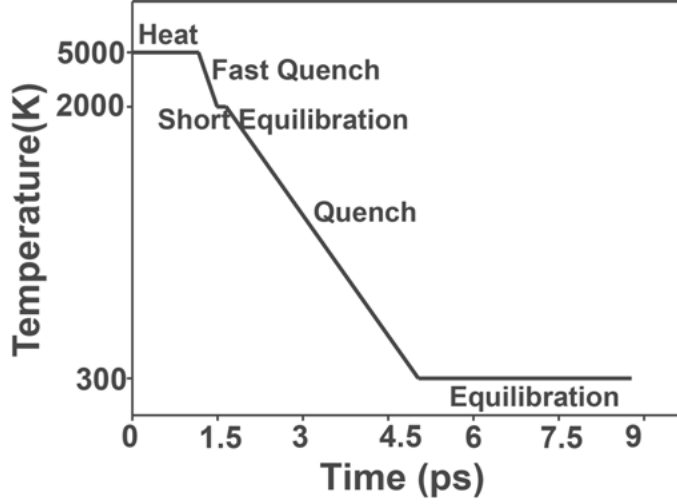


Figure 2.1. Cooling procedure which can be performed successfully by using CMD and FPMD methods.

angular distribution functions, Voronoi tessellation, and ring analysis. The structural analysis provides statistical information about local orderings, including SRO and MRO.

### 2.1.1 Radial Distribution Function

The radial distribution function (RDF) quantifies the probability of locating a particle at a specified distance, denoted as  $r$ , from a reference particle within a given system. The fundamental methodology entails calculating the number of particles situated within a radial range of  $r$  to  $r + dr$  from a reference particle. The volume of the spherical layer within a radial range of  $r$  to  $r + dr$  is equivalent to  $4\pi r^2 dr$ . RDF ( $g(r)$ ) can be written as

$$g(r) = \frac{1}{4\pi r^2 \rho N} \sum_{i=1}^N \sum_{j=1, j \neq i}^N \delta(r - |\mathbf{r}_{ij}|), \quad (2.1)$$

where  $N$  represents the total number of the atoms in the system,  $\rho$  is the number density, and  $|\mathbf{r}_{ij}|$  is the interatomic distance between atoms  $i$  and  $j$  [65]. The partial radial distribution function can be written as

$$g_{ab}(r) = \frac{N}{4\pi r^2 \rho N_a N_b} \sum_{i=1}^{N_a} \sum_{j=1}^{N_b} \delta(r - |\mathbf{r}_{ij}|), \quad (2.2)$$

where  $a$  and  $b$  represent atom types. The quantity of type  $a$  and  $b$  atoms are represented as  $N_a$  and  $N_b$  respectively. In Eq. 2.2,  $|\mathbf{r}_{ij}|$  is the interatomic distance between atoms  $i$  ( $a$  type) and  $j$  ( $b$  type).

RDF denotes the likelihood of the presence of atoms within a particular layer at a specified distance from any selected atom. At a distance equivalent to the first coordination sphere, the radial distribution function exhibits a peak, corresponding to the first nearest neighbor distance. This phenomenon is also observed at distances corresponding to the second, third, and subsequent coordination spheres. Apart from ideal crystalline materials, the fluctuations in the radial distribution function typically diminish after the fifth peak as in amorphous systems due to the existing short and medium-range ordering where long-range ordering cannot exist [1, 66, 67]. Amorphous solids, especially bulk metallic glasses radial distribution show a unique splitting on the second peak due to the special atomic configurations created by tetrahedra and/or quartotetrahedra [67, 68]. The short, and medium-range orderings can occur locally due to the electronic influence on the structure through spherical-periodic order [69]. Medium-range ordering can be constructed by a group of short-range ordering arrangements and/or one-dimensional translation of a locally favorable short-range ordering at the 1 - 2 nanometer range.

### 2.1.2 Angular Distribution Function

The angular distribution function is a measure of three-body correlations, providing insight into the spatial relationships between three adjacent atoms. The initial step involves identifying the nearest-neighbor atoms that are connected to the central atom through bonds. Subsequently, the angles between each pair of bonds are computed. This process is repeated for all atoms within the system to generate the overall distribution of bond angles. In particular, for a given atom  $i$  with  $N_i$  nearest neighbors, the bond length between neighbor  $j$  and atom  $i$  is denoted as  $r_{ij}$ , while the bond length between neighbor  $k$  and atom  $i$  is denoted as  $r_{ik}$ . The spatial separation between points  $j$  and  $k$  is denoted by  $r_{jk}$ . The bond angle ( $\theta_{ijk}$ ) between  $r_{ij}$  and  $r_{ik}$  can be written as

$$\theta_{ijk} = \cos^{-1} \left( \frac{r_{ij}^2 + r_{ik}^2 - r_{jk}^2}{2r_{ij}r_{ik}} \right). \quad (2.3)$$

The angular distribution function can be expressed as

$$g(\theta) = \frac{1}{\sum_{i=1}^N N_i(N_i - 1)} \sum_{i=1}^N \sum_{j=1}^{N_i} \sum_{k=j+1}^{N_i} \delta(\theta - \theta_{ijk}). \quad (2.4)$$

Eq. 2.4 reveals the positioning of bonded atoms and neighbors [54]. In contrast to the sharp peaks observed at specific angles in crystalline solids, the angular distribution function of amorphous solids displays a broad spectrum.

### 2.1.3 Voronoi Tessellation

Voronoi Tessellation is a structural characterization method that provides insight into the short-range ordering of amorphous structures by dividing the structure into three-dimensional polyhedra centered around each atom, similar to the Wigner-Seitz primitive cell. This is done by drawing lines from a given atom to its neighboring atoms and constructing perpendicular planes at the midpoint or at a point determined relative to the different radii of the constituent atoms. The method gives coordination numbers by considering the nearest neighboring atoms sharing a common cell surface, which is the definition of the number of atoms located within the nearest-neighbor shell of a specific central atom. Voronoi polyhedra can be expressed with a vector of Voronoi indexes  $\langle s_3, s_4, s_5, s_6 \rangle$  where  $s$  is the polyhedron's surfaces and subindexes represents the polyhedron's edges (e.g. triangles, polyhedron, pentagon, etc numbers in the polyhedron). A  $k$ -edged polygon between bonding atoms typically indicates the presence of  $k$  common neighbors surrounding the pair, forming a  $k$ -fold bond local environment [70, 71, 72]. A widely obtained local structures in amorphous solids exhibit a 5-fold rotational symmetry and can be seen in two forms, perfect icosahedron ( $\langle 0, 0, 12, 0 \rangle$ ) and distorted icosahedron ( $\langle 0, 2, 8, 2 \rangle$ ;  $\langle 0, 1, 10, 2 \rangle$ ;  $\langle 0, 1, 10, 4 \rangle$ ; etc.). Fcc-type ( $\langle 0, 2, 8, 4 \rangle$ , etc.) and bcc-type ( $\langle 0, 3, 6, 4 \rangle$ , etc.) of local orderings can also frequently exist in an amorphous solid. The Voronoi indices representing crystalline fcc/hcp and bcc are  $\langle 0, 12, 0, 0 \rangle$  and  $\langle 0, 6, 0, 8 \rangle$ , respectively.

### 2.1.4 Ring Statistics

Ring statistics is used to simplify the structures of topological networks. Atoms and bonds are represented as nodes and links, regardless of atom species or bond characteristics. A path is defined as a chain of continuously associated nodes and links without overlap, while a ring is defined as a closed path. Rings with  $n$  links are referred to as  $n$ -ring. Each node or link should have an associated local cluster of rings, known as a ring cluster. A ring can be described as primitive when it cannot be broken down into two smaller rings. To determine whether a ring structure is primitive, one can systematically analyze each pair of nodes on the ring to ascertain the presence or absence of a shortcut. If no shortcuts are found between any node pairs, the ring can be classified as primitive. A ring structure with a path connecting any two of its nodes can be considered as an example in Fig. 2.2.

As depicted in Fig. 2.2, a path designated as  $Y$  ( $i - Y - j$ ) connects nodes  $i$  and  $j$  within the ring labeled as  $X - Z$  ( $i - X - j - Z - i$ ). The length relation between paths  $X$ ,  $Z$ , and  $Y$  determines whether the ring is primitive or not according to whether it fits the three criteria. First, if the length between the paths is equal ( $X = Y = Z$ ), the rings  $XY$ ,  $XZ$ , and  $YZ$  are primitive rings. Second, if the two path lengths are equal and smaller than the third path's

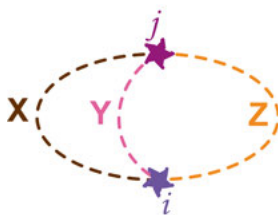


Figure 2.2. Primitive ring example.

length, there are one small and two bigger rings (e.g  $X = Y < Z$  means  $XY$  is the small ring and two  $XZ$ , and  $YZ$  are the bigger rings.). Because any of the three rings is the sum of two smaller rings, all three are classified as primitive rings. Third, if the path two paths' length is equal and bigger than the other, or if the path lengths are increasing respectively, there is one shortest path. For example; if the case is  $X < Y = Z$ , or  $X < Y < Z$ , then the shortest path is  $X$ . The ring labeled  $YZ$ , which is constructed without the shortest path, can be decomposed into the sum of two smaller rings,  $XY$ , and  $XZ$ . As a result, this ring is not considered a primitive ring [73].

## 2.2 Molecular Dynamics Simulations

Classical molecular dynamics simulations (CMD) is an effective method for simulating the thermodynamic, mechanical, and chemical properties of solids and liquids in a detailed and precise manner. The accuracy of the simulation is determined by the interatomic potential (force field), which calculates the potential energy of the system based on the positions of atoms and other factors. The time evolution of the system is calculated by numerically integrating Newton's equations of motion over a significant number of timesteps to track the positions and velocities of the atoms [74, 63]. Molecular dynamics (MD) simulations are characterized by their deterministic nature, where the outcome is dictated by the initial conditions and equations of motion. Conversely, Monte Carlo simulations are stochastic and depend on random sampling to generate results. The molecular dynamics (MD) technique comprises two primary forms: one for systems that are in equilibrium and another for systems that are out of equilibrium. Nonequilibrium molecular dynamics (NEMD) is an alternative to equilibrium molecular dynamics to calculate transport coefficients under an applied external force applied to the system. Equilibrium molecular dynamics is typically used for an isolated system with a fixed number of atoms ( $N$ ) in a fixed volume ( $V$ ). Since the system is isolated, the total energy ( $E$ ), which is the sum of the kinetic and potential energies, remains constant. This is known as a microcanonical ensemble (NVE). The thermodynamic state of the system is determined by the variables  $N$ ,  $V$ , and  $E$  and atomic position  $\mathbf{r}^N$  is found by solving Newton's equations of motion:

$$\mathbf{F}_i(t) = m\ddot{\mathbf{r}}_i(t) = -\frac{\partial U(\mathbf{r}^N)}{\partial \mathbf{r}_i}, \quad (2.5)$$

where  $\mathbf{F}_i$  represents the force on  $i^{th}$  atom created by the  $N-1$  other atoms.  $m$  is the mass molecular mass and  $U$  corresponds to interatomic potential energy. The double integral of Eq. 2.5 yields the atomic positions. By repeatedly integrating, individual atomic trajectories can be generated, enabling the calculation of time averages  $\langle A \rangle$  for macroscopic properties:

$$\langle A \rangle = \lim_{t \rightarrow \infty} \frac{1}{t} \int_{t_0}^{t_0+t} A(\tau) d\tau. \quad (2.6)$$

$\langle A \rangle$  in Eq.2.6 cannot rely on  $t_0$  at equilibrium. Because it stands for both static (e.g. thermodynamic) and dynamic (e.g. transport coefficients) properties, due to the positions and momenta being calculated. In accordance with the principles of the ergodic hypothesis, a Molecular Dynamics trajectory that satisfies certain criteria permits the equivalence of time and ensemble averages, thereby rendering MD averages a valuable tool. The ergodic hypothesis posits that, given sufficient time, a system will explore all microstates within a given energy range with equal probability. Therefore in an ergodic system, the time and ensemble averages should be the same. The velocity Verlet algorithm is one of the commonly used computational techniques for integrating Newton's equations of motion, to determine the trajectories of particles in molecular dynamics simulations [75, 76]. The Verlet algorithm forms the basis of molecular dynamics which is defined as

$$\mathbf{r}(t + \delta t) = \mathbf{r}(t) + \mathbf{v}(t)\delta t + \frac{1}{2}\mathbf{a}(t)\delta t^2, \quad (2.7)$$

where  $\delta t$  is the time increment of the system,  $\mathbf{r}$ ,  $\mathbf{v}$ , and  $\mathbf{a}$  represent respectively the position, velocity, and acceleration vectors at time  $t$  and  $t + \delta t$ . Velocity Verlet algorithm can be derived by using Taylor expansion of reverse motion of displacement vector from forward one as below

$$\mathbf{v}(t + \delta t) = \mathbf{v}(t) + \frac{\mathbf{a}(t) + \mathbf{a}(t + \delta t)}{2}\delta t. \quad (2.8)$$

In accordance with the law of energy conservation, the numerical solution can be satisfied by the instantaneous sum of kinetic and potential energy. The Verlet algorithm can produce realistic results when calculations are performed over a large number of time steps.

The microcanonical ensemble can serve as a thermal reservoir in simulations utilizing the canonical ensemble. Variables of the canonical ensemble are the number of atoms ( $N$ ), the volume of the system ( $V$ ), and temperature ( $T$ ). This is known as (NVT) also. In the canonical ensemble, probabilities are assigned to individual microstates of a system in accordance with the Boltzmann

distribution. The probability ( $P$ ) of a given microstate is proportional to the exponential of the ratio of its negative energy ( $E$ ) to the product of Boltzmann's constant ( $k_B$ ) and the system's temperature ( $T$ );  $P \propto e^{\frac{-E}{k_B T}}$ . Thermostats may be employed to regulate the temperature of an NVE simulation by linking it to a heat bath maintained at a constant temperature, thereby converting it into an NVT simulation. AIMD forces are derived from solutions to the Schrödinger equation.

### 2.2.1 Thermostats

Thermostat refers to the process of regulating the temperature of particles in an MD simulation. The goal of the thermostat is to bring the system to equilibrium at the desired temperature. The thermostat algorithm modifies the Newtonian MD scheme to generate a thermodynamic ensemble at a constant temperature. This is important for matching experimental data, studying temperature-dependent processes, evacuating heat in dissipative NEMD, enhancing the efficiency of conformational studies, and avoiding steady energy drifts caused by the accumulation of numerical errors. The initial requirements for thermostats include instantaneous temperature, reference temperature of the heat bath, and average internal kinetic energy, which is related to macroscopic temperature through the equipartition theorem. Several modeling methods are available for maintaining temperature or pressure, including stochastic (which constrains a system variable to present a distribution function, such as Andersen, Langevin thermostats), strong-coupling (which scales a system variable to give an exact present derived value, such as Nose-Hoover thermostat), weak-coupling (which scales a system variable in the direction of the desired derived value, such as Berendsen thermostat), and extended system dynamics (which extends degrees of freedom to include temperature or pressure terms, such as Parinello-Rahman (NPE), (Nose-Parinello-Rahman (NPT)). In CMD, we used Berendsen thermostat. In AIMD, we employed velocities rescaling which enables a gradual increase or decrease in kinetic energy. During the intermediate period, a micro-canonical ensemble is simulated. The velocities are adjusted at each  $N_B$  step, starting from the first step (i.e., when  $\text{MOD}(N_s, N_B)=1$ ), to match the temperature calculated as  $T = T_{Begin} + (T_{End} - T_{Begin}) \times N_s / N_{sim}$ .  $N_s$  represents the current step, starting from 1, while  $N_{sim}$  is the total simulation time in multiples of  $N_B$ .

### 2.2.2 Berendsen Thermostat

The Berendsen thermostat [77] is designed to alter the Langevin equation of motion ( $m_i \ddot{\mathbf{v}}_i = \mathbf{F}_i - m_i \gamma_i \mathbf{v}_i + \mathbf{R}_i$ ; where systematic force is  $\mathbf{F}_i$ ; friction term is  $\gamma_i$  and  $\mathbf{R}_i$  is Gaussian stochastic variable) by eliminating the local temperature coupling that occurs through random noise while keeping the global

coupling intact. This is done to minimize local disturbances. The Berendsen thermostat simulates the disturbance that would happen in a perfect physical non-equilibrium experiment. Additionally, the strength of the coupling can be adjusted, allowing for easy evaluation and control of its impact. It is a reliable method that enables smooth transitions to new pressure or temperature values without requiring any intermediate modifications. The Berendsen thermostat uses a time scale to update velocities, rather than scaling them to the desired temperature at each time step. This approach weakly couples the system to a heat bath, with the coupling constant or heat transfer time scale referred to as  $\tau$  and can be written as

$$\lambda^2 = 1 + \frac{\delta t}{\tau} \left( \frac{T}{T_{ins}} - 1 \right), \quad (2.9)$$

where the thermostat temperature is denoted by  $T$ , while the instantaneous kinetic temperature is denoted by  $T_{ins}$ ,  $\delta t$  is time step, and  $\lambda$  is the velocity rescaling factor. Although the Berendsen thermostat does not produce exact energy fluctuations, it closely approximates the real canonical ensemble.

### 2.2.3 Embedded Atom Method Potential

The embedded atom method (EAM) is a semi-empirical, interatomic potential approximation that describes the energy between atoms as a function of the sum of functions of the separation between an atom and its neighbors. These functions represent the electron density. EAM is related to the second moment approximation to tight-binding theory, also known as the Finnis-Sinclair model.  $i^{th}$  atom's total energy can be described as

$$E_i = F_\alpha \left( \sum_{j \neq i} \rho_\beta(r_{ij}) \right) + \frac{1}{2} \sum_{j \neq i} \phi_{\alpha\beta}(r_{ij}), \quad (2.10)$$

where the embedding energy, denoted as  $F_i$ , is a function of the atomic electron density represented by  $\rho_\beta$ . The interaction between pairs of atoms is described by the pair potential,  $\phi_{\alpha\beta}$ , with alpha and beta representing the element types of atoms  $i$  and  $j$ , respectively. The multi-body nature of the EAM potential arises from the inclusion of the embedding energy term. The formula includes summations over all neighboring atoms  $j$  within a specified cutoff distance from atom  $i$  [60].

EAM potential was derived by fitting experimental data and parameterizing it for a range of physical properties, including enthalpy of formation or mixing, lattice parameter, and elastic constant. It is particularly suitable for metallic systems with empty or filled d bands with large unit cells. EAM is widely used in molecular dynamics simulations to explore a wide range of topics, including point defects, melting, alloying, grain boundary structure and energy, dislocations, segregation, fracture, surface structure, and epitaxial growth.



## 2.2.4 Tersoff Potential

The Tersoff potential [61, 78] is a bond-order potential that belongs to a class of empirical interatomic potentials utilized in molecular dynamics and molecular statics simulations. It is a three-body potential function that incorporates an angular contribution from the force, allowing for the explicit modeling of three-body interactions. The total binding energy of a system is calculated as the sum of the binding energies of each individual bond. Each bond's energy consists of a repulsive pairwise contribution and an attractive contribution, with the latter being the product of the bond order and the pairwise energy. The bond order takes into account both the local coordination number and bond angles, allowing for the modeling of different geometries such as linear, trigonal, or tetrahedral configurations. This is particularly important for accurately representing covalent materials. The Tersoff potential takes into account the number of bonds between two atoms when calculating their interaction energy. It is composed of two-body terms that are influenced by the local environment surrounding the atoms. The potential energy can be represented as

$$E = \sum_i E_i = \frac{1}{2} \sum_{i \neq j} V_{ij} \quad (2.11)$$

$$V_{ij} = f_c(r_{ij})[f_R(r_{ij}) + b_{ij}f_A(r_{ij})] \quad (2.12)$$

$$f_R(r_{ij}) = A_{ij} \exp(-\lambda_{ij}r_{ij}) \quad (2.13)$$

$$f_A(r_{ij}) = B_{ij} \exp(-\mu_{ij}r_{ij}) \quad (2.14)$$

$$f_c(r_{ij}) = \begin{cases} 1 & r_{ij} < R_{ij} \\ \frac{1}{2} + \frac{1}{2} \cos\left(\pi \frac{r_{ij} - R_{ij}}{S_{ij} - R_{ij}}\right) & R_{ij} < r_{ij} < S_{ij} \\ 0 & r_{ij} > S_{ij} \end{cases} \quad (2.15)$$

$$b_{ij} = \xi_{ij}(1 + \beta_i^{n_i} \zeta_{ij}^{n_i})^{-1/2n_i} \quad (2.16)$$

$$\zeta_{ij} = \sum_{k \neq i, j} f_c(r_{ik}) \omega_{ik} g(\theta_{ij}) \quad (2.17)$$

$$g(\theta_{ij}) = 1 + c_i^2/d_i^2 - c_i^2/[d_i^2 + (h_i - \cos\theta_{ijk})^2] \quad (2.18)$$

$$\lambda_{ij} = \frac{\lambda_i + \lambda_j}{2}, \mu_{ij} = \frac{\mu_i + \mu_j}{2} \quad (2.19)$$

$$A_{ij} = (A_i + A_j)^{1/2}, B_{ij} = (B_i + B_j)^{1/2} \quad (2.20)$$

$$R_{ij} = (R_i R_j)^{1/2}, S_{ij} = (S_i S_j)^{1/2}, \quad (2.21)$$

where  $i, j$ , and  $k$  denote the atomic labels,  $r_{ij}$  represents the bond length between atoms where  $i$  and where  $j$ , and  $\theta_{ijk}$  signifies the bond angle formed by the  $ij$  and  $ik$  bonds. In Eq. 2.16, the  $\xi_{ij}$  variable serves to either weaken or reinforce heteropolar bonds. The  $\omega_{ik}$  variable in Eq. 2.17 allows for increased

adaptability when handling significantly dissimilar atomic species. The  $\lambda_{ij}$ ,  $\mu_{ij}$ ,  $A_{ij}$ ,  $B_{ij}$ ,  $R_{ij}$ , and  $S_{ij}$  variables are presumed to be represented by single-subscript parameters that rely solely on atomic types, as demonstrated in Eq. 2.19 through Eq. 2.21. The Tersoff potential can well describe the properties of liquid and amorphous phases of silicon.

## 2.2.5 Lattice Thermal Conductivity

The calculation of lattice thermal conductivity can be achieved through equilibrium molecular dynamics simulations utilizing the Green-Kubo theory. This method employs the autocorrelation function of heat flux in its calculations.

### Green-Kubo Thermal Conductivity Approach

The Green-Kubo thermal conductivity approach is used for determining the transport characteristics of systems, including thermal conductivity, using equilibrium molecular dynamics simulations. This method is founded on linear response theory and the fluctuation-dissipation theorem, which connects a system's response to external disturbances with its equilibrium fluctuations [79, 80]. The thermal conductivity tensor, denoted by  $\kappa$  ( $\kappa$ ), quantifies a material's ability to transfer heat energy through diffusion, as described by Fourier's law:

$$\mathbf{J} = -\kappa \nabla(T), \quad (2.22)$$

where  $\mathbf{J}$  represents the heat flux, measured in energy per area per time, while  $\nabla(T)$  denotes the temperature's spatial gradient. Thermal conductivity, often considered an isotropic scalar quantity, is expressed in units of energy per distance per time per degree Kelvin. The heat flux  $\mathbf{J}$  can be written for two-body interactions as

$$\begin{aligned} \mathbf{J} &= \frac{1}{V} \left[ \sum_i \epsilon_i \mathbf{v}_i + \sum_i \mathbf{S}_i \mathbf{v}_i \right] \\ &= \frac{1}{V} \left[ \sum_i \epsilon_i \mathbf{v}_i + \sum_{i < j} (\mathbf{F}_{ij} \cdot \mathbf{v}_j) \mathbf{r}_{ij} \right], \end{aligned} \quad (2.23)$$

where  $V$  is the volume,  $\epsilon_i$  is the total energy of the  $i^{th}$  atom (which is a summation of kinetic and potential),  $\mathbf{S}_i$  represents the per-atom stress tensor (which includes the  $i$ th atom's kinetic energy contribution, intra, and intermolecular interactions' virial contribution, and can be written in terms of  $\mathbf{r} \cdot \mathbf{F}$  as in the following equation).  $\mathbf{v}_i$  corresponds to the velocity of atom  $i$ ,  $\mathbf{F}_{ij}$  represents the force on atom  $i$  from atom  $j$  and  $\mathbf{r}_{ij}$  stands for the position vector of atom  $i$  relative to atom  $j$ . The first term represents the impact of convection, or the diffusion of atoms, while the second term accounts for energy transfer between

adjacent atoms [81]. In the case of non-diffusive atoms, the convection term is zero and negligible.

The Green-Kubo formulas establish a relationship between the thermal conductivity, denoted by  $\kappa$ , and the ensemble average of the heat flux's ( $\mathbf{J}$ ) auto-correlation as

$$\kappa = \frac{V}{3k_B T^2} \int_0^\infty \langle \mathbf{J}(t) \cdot \mathbf{J}(0) \rangle dt, \quad (2.24)$$

where  $k_B$  is the Boltzmann constant, and the angular brackets denote an auto-correlation function. The auto-correlation function is used to identify the similarity of functions or a series of values between a delayed version of itself. It calculates the correlation between the values of a function, based on the time lag separating them. So, Eq.2.24 can be written as

$$\kappa = \frac{V}{3k_B T^2} \Delta t \sum_{m=1}^M \frac{1}{N-m} \sum_{n=1}^{N-m} \mathbf{J}(n+m) \cdot \mathbf{J}(n), \quad (2.25)$$

where  $N$  represents the total time,  $\Delta$  is timestep, index  $n$  corresponds to the time-origins whereas index  $m$  corresponds to the time-lags and  $M$  is the maximum time-lag [82].

## 2.2.6 Vibrational Density of States

The vibrational density of states is a crucial characteristic of a solid system, as it influences both optical and thermodynamic properties [83]. For amorphous solids, the calculation of the vibrational density of states (VDOS) can be achieved through the application of a Fourier transform to the velocity autocorrelation function (VACF). At a given instant time ( $t$ ),  $\mathbf{v}_i(t)$  represents the random value of the particle's velocity, assuming that its initial velocity at  $t = 0$  was  $\mathbf{v}_i(0)$ , where the average is zero ( $\langle \mathbf{v}(t) \rangle = 0$ ). If the net force acting on the  $i^{th}$  particle is zero, its velocity will remain constant. Nonetheless, particle velocity is subject to variation due to inter-particle interactions, resulting in a significant loss of correlation between initial and subsequent velocities over time. The local density of states at an atom can be determined by performing a Fourier transform on the time-dependent velocity of the said atom. This process is repeated for all non-equivalent atoms within the solid. By definition VACF can be written as  $Z(t)$  and VDOS ( $g(\omega)$ ):

$$VACF = Z(t) = \frac{\langle \mathbf{v}_i(t) \cdot \mathbf{v}_i(0) \rangle}{\langle \mathbf{v}_i(0) \cdot \mathbf{v}_i(0) \rangle}, \quad (2.26)$$

$$g(\omega) = \frac{1}{3Nk_B T} \int_{-\infty}^{\infty} \sum_1^N Z(t) e^{i\omega t} dt, \quad (2.27)$$

where  $i$  denotes the  $i^{th}$  atom and  $N$  is the total number of atoms in the unit cell.

The calculated  $g(\omega)$  encompasses all possible excitations within the system, which are called ‘vibron modes’ in contrast to a crystal’s lattice vibrations (‘phonon modes’). Vibrons include ‘extendons’ and ‘locons’ modes. In amorphous solids, the main heat carriers are extendons, where the constituents are described as; ‘propagons’ and ‘diffusions’. Locon modes do not contribute to heat carrying [84]. By using molecular dynamics, it is not possible to make a quantitative comparison of these modes, but a qualitative comparison can be calculated with the participation ratio (PR) [85]. PR can be used to determine the contribution of each excited mode by using  $g(\omega)$  as

$$PR(\omega) = \frac{1}{N} \frac{(\sum_i g_i(\omega)^2)^2}{\sum_i g_i(\omega)^4}. \quad (2.28)$$

In the crystalline case, when PR is 1 according to Eq.2.28 this corresponds to a phonon mode to which all atoms contribute equally. Similarly, in amorphous solids, propagons are a kind of plane wave propagating modes like phonons at low frequencies. Although diffusions are propagating modes, they cannot be written as plane waves. Propagons are the dominant vibrational modes until the Ioffe-Regel limit. Between the Ioffe-Regel limit and the mobility edge, the vibrational modes are the diffusion modes. On the contrary, the locons can be thought of as localized modes confined to the atomic region without propagation at high frequencies. Beyond the mobility edge, locons are the dominant excitations [84]. The qualitative comparison used is that the decreasing value from ‘1’ in PR with increasing frequency shows the fingerprints of propagons, and diffusions, whereas the decreasing value from ‘0.2’ corresponds to locons in an amorphous system. We quantified the change in VDOS (Eq. 2.29) and PR (Eq. 2.30) in relation to a reference system (bulk referred to as ‘0’), in cases of systems with modifications such as voids, by dividing it by the referred system value as defined below

$$\Delta g(\omega) = \frac{g_0(\omega) - g_v(\omega)}{g_0(\omega)}, \quad (2.29)$$

$$\Delta PR(\omega) = \frac{PR_0(\omega) - PR_v(\omega)}{PR_0(\omega)}, \quad (2.30)$$

where  $v$  represents the system with voids.

## 2.3 Density Functional Theory

The density functional theory (DFT) uses Thomas and Fermi’s idea of electron density by describing the many-body in the ground state. This theory was

presented at the same time as Hartree-Fock's theory which was based on wave-functions. The DFT was named after the two equations' proposers; Hohenberg and Kohn (KH) [86] and Kohn-Sham (KS) [87]. Hohenberg and Kohn (KH) presented two theorems; the first was that the ground state particle density  $\rho_0(r)$  defines the external potential  $V_{ext}$  for a system including interacting particles under an  $V_{ext}$ , apart from an additive constant. Accordingly, the ground state expectation value is a function of the ground state particle density  $\rho_0(\mathbf{r})$  for each physical observable. The second was that it is possible to define the total energy as a function of  $\rho(r)$ , ( $E[\rho(\mathbf{r})]$ ), for an interacting system under an external potential, ( $V_{ext}$ ), as in the following Eq. 2.31:

$$E[\rho(\mathbf{r})] = F_{HK}[\rho(\mathbf{r})] + \int V_{ext}(\mathbf{r})\rho(\mathbf{r})d\mathbf{r}, \quad (2.31)$$

where  $F_{HK}[\rho(\mathbf{r})]$ , includes each internal energies in an interacting system under  $V_{ext}$ . It is also the same for each electron system autonomously from the applied external potential. When the condition of that the integral of  $\rho_0(\mathbf{r})$  maintains the total number of electrons is satisfied, the ground state energy can be calculated by minimizing  $E[\rho(\mathbf{r})]$  as below:

$$\frac{\partial}{\partial \rho} E[\rho(\mathbf{r})]|_{\rho=\rho_0} = 0, \quad (2.32)$$

$$E_0 = E[\rho_0(\mathbf{r})]. \quad (2.33)$$

In order to match the nature of the antisymmetric wavefunction in ground state energy and energy density calculations, some bounds must be placed on the subspace of all antisymmetric wavefunctions corresponding to the same energy density [88, 89]. These two theorem forms the basis of DFT. HK theory's kinetic energy representation was proposed in Kohn-Sham paper [87].

### 2.3.1 Kohn-Sham Equations

Transformation of an interacting electron system's ground state to a reference system with a non-interacting and equivalent electron density is suggested by Kohn-Sham (KS). Each electron in the transferred reference system moves freely under the potential applied by cores and all other electrons. By collecting all other many-body terms in exchange-correlation energy;  $E_{xc}$ , KS rewrote the  $F_{HK}[\rho(\mathbf{r})]$  as

$$F[\rho(\mathbf{r})] = T_0[\rho(\mathbf{r})] + \frac{1}{2} \int \frac{\rho(\mathbf{r})\rho(\mathbf{r}')}{|\mathbf{r} - \mathbf{r}'|} d\mathbf{r}d\mathbf{r}' + E_{xc}[\rho(\mathbf{r})], \quad (2.34)$$

where the kinetic energy term of independently moving electron is shown by  $T_0[\rho(\mathbf{r})]$ . Afterward, the Kohn-Sham density functional theory is

$$E_{KS}[\rho(\mathbf{r})] = T_0[\rho(\mathbf{r})] + \int V_{ext}(\mathbf{r})\rho(\mathbf{r})d\mathbf{r} + \frac{1}{2} \int \frac{\rho(\mathbf{r})\rho(\mathbf{r}')}{|\mathbf{r} - \mathbf{r}'|} d\mathbf{r}d\mathbf{r}' + E_{xc}[\rho(\mathbf{r})]. \quad (2.35)$$

Reduction of  $E_{KS}[\rho(\mathbf{r})]$  respect to  $\rho(\mathbf{r})$  by unchanging of the total number of electrons, is written as

$$\frac{\partial}{\partial \rho(\mathbf{r})}(E_{KS}[\rho(\mathbf{r})] - \mu \int \rho(\mathbf{r})d\mathbf{r}) = 0. \quad (2.36)$$

Thereupon, Kohn-Sham's effective potential is written as

$$V_{eff}(\mathbf{r}) = V_{ext}(\mathbf{r}) + \int \frac{\rho(\mathbf{r}')}{|\mathbf{r} - \mathbf{r}'|} d\mathbf{r}' + \frac{\partial E_{xc}}{\partial \rho(\mathbf{r})}. \quad (2.37)$$

When the defined  $V_{eff}(\mathbf{r})$  is added to the Schrödinger equation, it can be solved for the single electron orbital.

The interacting system in the Kohn-Sham framework is matched by the system which is non-interacting and has the same charge density. The ground state charge density  $\rho(\mathbf{r})$  and kinetic energy functional can be written by using Kohn-Sham orbitals  $\psi_n(\mathbf{r})$ :

$$\rho(\mathbf{r}) = 2 \sum_{n=1}^{N/2} |\psi_n(\mathbf{r})|^2, \quad (2.38)$$

and

$$T_0[\rho(\mathbf{r})] = -2 \frac{\hbar^2}{2m} \sum_{n=1}^{N/2} \int \psi_n^*(\mathbf{r}) \frac{\partial^2 \psi_n(\mathbf{r})}{\partial \mathbf{r}^2} d\mathbf{r}, \quad (2.39)$$

where  $N$  represents the total number of electrons in the non-magnetic system. Accordingly,  $N/2$  can verify the lowest orbital states which are occupied by two electrons with opposite spins;  $\rho_{\uparrow}(\mathbf{r}) = \rho_{\downarrow}(\mathbf{r})$ .  $n$  as a composite index describes the set of bands in a periodic system and the wave vector in the Brillouin zone (BZ). Moreover, the Kohn-Sham equation can be solved for collinear magnetic systems by writing electron density as the sum of two different spin densities.

Solving the Kohn-Sham equation to find the KS orbitals primarily begins with defining the  $V_{eff}$  with respect to the initial charge density. The following step is to use the calculated KS orbitals to calculate the new density after mixing it with the one calculated in the previous step and to use it in the next density calculation as well. Repetition of these two steps continues until the charge density is comparable to the previous step within the defined tolerance limit. This is referred to as self-consistent calculation.

### 2.3.2 Exchange Correlation Energy

The exchange-correlation energy ( $E_{xc}$ ) must be well defined for solving the Kohn-Sham equations accurately. There have been several approximations to

define the  $E_{xc}$  2.40. One of these approximations is known as local density approximation (LDA) [87]. LDA suggests calculating an electron's exchange-correlation energy  $\epsilon_{xc}(r)$  assuming the electron is in a homogeneous electron gas that has the same density at that point in the real system  $\epsilon_{xc}(r)$  as:

$$E_{xc}^{LDA}[\rho(\mathbf{r})] = \int \epsilon_{xc}[\rho(\mathbf{r})]\rho(\mathbf{r})d\mathbf{r}. \quad (2.40)$$

LDA produces reliable results in the calculation of structural, elastic, vibrational, electronic (except for electronic band gap), and magnetic properties. The weakness of LDA is in the calculation of activation energies and chemical interactions. Aside from LDA, generalized gradient approximation (GGA) is another efficient approximation that we used in our works in this thesis.

The GGA method could overcome the overbinding problem of LDA. The GGA is more advanced compared to LDA because while GGA is still a local function, it includes both density and its gradient at each point in the same coordinate system. The inclusion of gradient corrections supports an enhanced exchange of energy by the increased charge density. GGA is able to precisely forecast the molecular geometries and ground state energies by both enlarging lattice constant and reducing bulk moduli. Nonetheless, it is not successful in precisely predicting the band gap and the interactions between layers that result from Van der Waals forces. The inclusion of vdW corrections into GGA calculations makes it possible to calculate vdW. One of the most commonly used GGA-functional is the PBE method which was introduced by Perdew, Burke, and Ernzerhof in 1996 [90]. PBE suggests the following exchange functional,

$$E_{xc}^{PBE}[\rho(\mathbf{r})] = \int \rho(\mathbf{r})\epsilon_x^{hom}[\rho(\mathbf{r})]F_{xc}(r_s, \tau, s)d\mathbf{r}, \quad (2.41)$$

where  $\epsilon_x^{hom}$  denotes exchange term of uniform density system and is equivalent to  $-3e^2k_F/4\pi$ ,  $s$  is dimensionless density gradient,  $\tau$  stands for the spin polarization, and  $F_{xc}$  represents the enhancement factor relative to the local Seitz radius;  $r_s$ . PBE functional can successfully calculate bond lengths, angles while it can not accurately estimate the electronic energy band gap.

### 2.3.3 Bloch Equation and k-point Sampling

A crystal structure is built by the regular placement of its unit cell in specific crystal directions. It can be inferred that the total number of electrons in the crystal is infinite due to the bulk form of the structure containing a significantly larger quantity of atoms. Accordingly, the calculation of the crystal properties including relevant electronic interactions in a single unit cell is feasible by utilizing Bloch's theorem. Bloch theorem denotes the wavefunction at  $\mathbf{r}$  in the following form:

$$\psi_n = e^{i\mathbf{k}\cdot\mathbf{r}} f_n(\mathbf{r}). \quad (2.42)$$

The periodic component can be augmented using a basis set of plane waves in the following way;

$$f_n(\mathbf{r}) = c_{n,\mathbf{G}} e^{i\mathbf{G}\cdot\mathbf{r}}, \quad (2.43)$$

where  $\mathbf{G}$  represents a reciprocal lattice vector. The wavefunction of each electron can be expressed in the following manner;

$$\psi_n(\mathbf{r}) = \sum_{\mathbf{G}} c_{n,\mathbf{k}+\mathbf{G}} e^{i(\mathbf{k}+\mathbf{G})\cdot\mathbf{r}}. \quad (2.44)$$

In a bulk solid, the restricted boundary conditions of electronic states are only specified at certain  $k$  points. The number of allowed  $k$  points is determined by the volume of the crystal in reciprocal space. With Bloch's theory, it is possible to determine a finite quantity of electron wavefunctions in contrast to a limitless number of wavefunctions at an infinite number of  $k$  points. As the number of  $k$  points increases, the total energy becomes more precise. At the same time, this also results in a higher demand for computational resources. Therefore, we increment the number of  $k$  points until the required precision is attained. The selection of  $k$  points is based on the approach developed by Monkhorst-Pack [90].

The expansion of the plane wave is terminated at a specific cut-off energy  $E_{cut}$  as illustrated below

$$\frac{\hbar|\mathbf{k} + \mathbf{G}|^2}{2m} \leq E_{cut}. \quad (2.45)$$

Utilizing plane waves with energies exceeding  $E_{cut}$  yields a more precise calculation of the system's total energy, however, results in a higher demand for computational resources. The achieved accuracy may not be considered significant compared to the extensive computational resources required.

The Kohn-Sham equation by using plane waves is shown below

$$\begin{aligned} \sum_{\mathbf{G}'} \left[ \frac{\hbar^2}{2m} |\mathbf{k} + \mathbf{G}|^2 \delta_{\mathbf{G}\mathbf{G}'} + V_{ion}(\mathbf{G} - \mathbf{G}') + V_H(\mathbf{G} - \mathbf{G}') + V_{XC}(\mathbf{G} - \mathbf{G}') \right] c_{n,\mathbf{k}+\mathbf{G}'} \\ = \epsilon_n c_{n,\mathbf{k}+\mathbf{G}}, \end{aligned} \quad (2.46)$$

where the electronic kinetic energy is represented diagonally when expressed through Fourier transformation. The size of the eigenvalue matrix is defined by the selected cut-off energy.

### 2.3.4 Pseudopotentials and PAW Method

The pseudopotential method is essential in illustrating the interactions between electrons and ions. Valence electrons have a higher level of importance compared to core electrons. The pseudopotential theory [91] relies on the use of



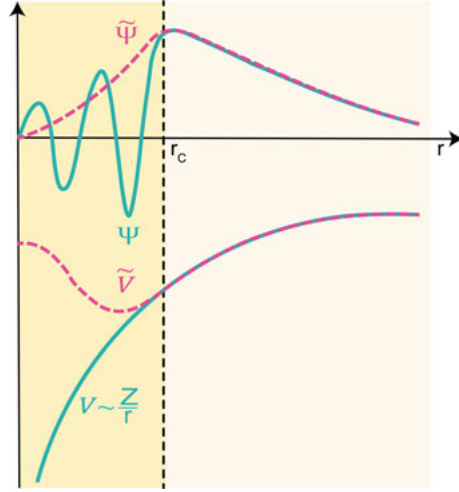


Figure 2.3. A schematic representation shows the behavior of wavefunctions near ( $r < r_c$ ) and far from ( $r > r_c$ ) atomic nuclei, where  $r_c$  is the cutoff radius. The cyan curve and magenta represent all-electron ( $|\Psi\rangle$ ,  $V$ ) and pseudo ( $|\tilde{\Psi}\rangle$ ,  $\tilde{V}$ ) wavefunctions, and potentials, respectively.

softer pseudopotentials that are described with pseudo wavefunctions, which are mainly contributed by valance electrons.

Employing pseudopotentials results in a highly similar total energy value in the case of all-electron potential (full-potential) use. A well-defined pseudo wavefunction ( $\tilde{\psi}$ ) and the accurate all-electron wavefunction ( $|\Psi\rangle$ ) are related through a linear transformation:

$$|\Psi\rangle = T |\tilde{\Psi}\rangle. \quad (2.47)$$

Fig. 2.3 illustrates that the two wavefunctions are the same beyond  $r_c$ . In Eq. 2.47,  $T$  is the transformation operator adjusting the smooth pseudo wavefunction inside each atomic region. Inside the core regions, the transformation operator is considered a summation of an identity operator with the addition of atomic orbital-based modification:

$$T = 1 + \sum_R \hat{T}_R, \quad (2.48)$$

where  $\hat{T}_R$  is only non-zero within a specific spherical region, called the augmentation region  $\Omega_R$ , that surrounds atom  $R$ .

The projector augmented wave (PAW) method, which combines ultrasoft pseudopotentials and all-electron methods, was derived by Bloch [92]. PAW method reduces the number of required plane wave basis sets by superimposing atomic orbital wavefunctions in the core region. The related canonical basis

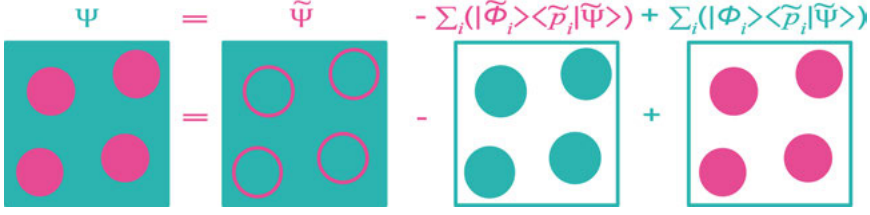


Figure 2.4. The (PAW) method technique for constructing an all-electron wavefunction.

sets of the PAW can be written as

$$|\tilde{\Psi}\rangle = \sum_i |\tilde{\phi}_i(r)\rangle c_i, \quad (2.49)$$

where  $\tilde{\Psi}_i(r)$  represents the pseudo partial wave solutions of the Schrödinger equation for an isolated atom,  $c_i$  denotes expansion coefficients, and  $i \equiv (R, l, m, n)$ .  $l, m$  are orbital and magnetic quantum numbers, respectively, and  $n$  denotes the plane wave index. The relationship between the pseudo-partial wave and the partial wave can be expressed as follows

$$\begin{aligned} |\phi_i\rangle &= T |\tilde{\phi}_i\rangle, r < r_c \\ |\phi_i\rangle &= |\tilde{\phi}_i\rangle, r > r_c. \end{aligned} \quad (2.50)$$

$T$  is a linear operator and  $c_i$  can be expressed as

$$c_i = \langle \tilde{p}_i | \tilde{\Psi} \rangle, \quad (2.51)$$

where  $|\tilde{p}_i\rangle$  are a group of projector functions satisfying the following criteria:

$$\langle \tilde{p}_i | \tilde{\phi}_j \rangle = \delta_{ij}, \quad (2.52)$$

and

$$\sum_i |\tilde{\phi}_i\rangle \langle \tilde{p}_i| = 1. \quad (2.53)$$

The specification of the transformation operator  $T$  relies on three key elements: the all-electron partial waves, denoted by  $|\phi_i\rangle$ , the pseudo partial waves, represented by  $|\tilde{\phi}_i\rangle$ , and the projector functions, symbolized by  $|\tilde{p}_i\rangle$ , which can be represented as

$$T = 1 + \sum_R \hat{T}_R = 1 + \sum_i (|\phi_i\rangle - |\tilde{\phi}_i\rangle) \langle \tilde{p}_i|. \quad (2.54)$$

Fig. 2.4 displays the all-electron wavefunction which can be described as

$$\Psi = T\tilde{\Psi} = \tilde{\Psi} + \sum_i (|\phi_i\rangle \langle \tilde{p}_i | \tilde{\Psi} \rangle - |\tilde{\phi}_i\rangle \langle \tilde{p}_i | \tilde{\Psi} \rangle). \quad (2.55)$$

By using Eq. 2.54 and Eq. 2.55, the density and the energy can be written respectively as in Eq. 2.56, and Eq. 2.57:

$$n(\mathbf{r}) = \tilde{n}(\mathbf{r}) + n^1(\mathbf{r}) + \tilde{n}^1(\mathbf{r}), \quad (2.56)$$

$$E = \tilde{E} + E^1 - \tilde{E}^1. \quad (2.57)$$

All elements are possible to be expressed as a particular PAW pseudopotential.

### 2.3.5 Structure Definition

The minimum energy state of a structure can be attained by reducing the Hellman-Feynman force [93] applied on each individual atom located in the unit cell. In terms of the force exerted on the  $I^{th}$  nuclei in an electronically steady state, the Hellman-Feynman force can be expressed as follows

$$\mathbf{F}_I = -\frac{\partial E(\mathbf{R})}{\partial \mathbf{R}_I} = -\left\langle \psi \left| \frac{\partial H}{\partial \mathbf{R}_I} \right| \psi \right\rangle, \quad (2.58)$$

where  $\mathbf{R}$  denote the coordinates of nuclei,  $H$  is Hamiltonian, and  $E(\mathbf{R})$  express the total energy. The Kohn-Sham electronic wavefunction at the ground state is represented as  $\psi$ . A nucleus is considered to be in equilibrium when the forces acting upon it are zero:

$$\mathbf{F}_I = -\frac{\partial E(\mathbf{R})}{\partial \mathbf{R}_I} = 0. \quad (2.59)$$

### 2.3.6 Van der Waals Interaction

Van der Waals (vdW) forces are long-range attractive interactions that are particularly significant in materials with a layered structure similar to graphite. The inclusion of vdW corrections results in a reduction of lattice constants and bond lengths. Several different approximations have been developed to date [94, 95, 96, 97]. We chose to perform our research using Grimme's DFT-D3 correction method [95] as described below

$$E_{DFT-D} = E_{DFT} + E_{disp}, \quad (2.60)$$

where  $E_{DFT}$  represents self-consistent DFT energy and  $E_{disp}$  serve as the correction term;

$$E_{disp} = -\frac{1}{2} \sum_{i=1}^N \sum_{j=1}^N \sum_{\mathbf{L}}' \left( f_{d,6}(r_{ij,\mathbf{L}}) \frac{C_{6ij}}{r_{ij,\mathbf{L}}^6} + f_{d,8}(r_{ij,\mathbf{L}}) \frac{C_{8ij}}{r_{ij,\mathbf{L}}^8} \right). \quad (2.61)$$

where  $N$  represents all atoms in the simulation cell, and  $\mathbf{L}$  is all translations of unit cell where  $i \neq j$  for  $\mathbf{L} = 0$ .  $r_{ij,\mathbf{L}}$  is the distance between atom  $i$ , which is

situated in the reference cell  $L = 0$ , and atom  $j$ , which is located in cell  $\mathbf{L}$ . In this approach, the dispersion coefficients ( $C_{6ij}$  and  $C_{8ij}$ ) vary depending on the geometry around  $i$  and  $j$  atoms. The Becke-Johnson (BJ) damping function can be written as

$$f_{d,n}(r_{ij}) = \frac{s_n r_{ij}^n}{r_{ij}^n + (a_1 R_{0ij} + a_2)^n}, \quad (2.62)$$

where (order  $n = 6, 8, 10, \dots$ ),  $s_6$  is set to the value 1, and  $a_1$ ,  $a_2$ , and  $s_8$  are adjustable parameters.

### 2.3.7 Optical Properties

DFT has emerged as a groundbreaking approach that facilitates the discovery of optical materials without the necessity of physical experimentation. Methods for calculating optical functions using DFT have been established and a plethora of optical spectra have been derived from DFT calculations[98]. However, the selection of an approximation method can have a significant impact on the resulting DFT spectra. As such, it is imperative to validate DFT calculation results against experimental data [99].

#### Independent Particle Approximation

The independent-particle approximation (IPA) is used for determining the optical response of materials using first-principles calculations. This method assumes that electrons within the material act as individual particles and do not interact with one another through many-body interactions when calculating the material's optical properties [100]. Although IPA can be computationally expensive, this cost can be reduced by only considering interband transitions where exchange and correlation are not taken into account and by neglecting local field effects (LFE) arising from density variations in the Hartree potential [101]. The imaginary part of the frequency-dependent dielectric functions at the long-wavelength limit, denoted as  $(\epsilon_2^{ij})$  tensor, is calculated using Eq. 2.63:

$$\epsilon_2^{ij} = \frac{4\pi^2 e^2}{\Omega} \lim_{q \rightarrow 0} \frac{1}{q^2} \sum_{v,c,\mathbf{k}} 2w_{\mathbf{k}} \delta(\epsilon_{c\mathbf{k}} - \epsilon_{v\mathbf{k}} - \omega) \times \langle u_{c\mathbf{k}+q\mathbf{e}_i} | u_{v\mathbf{k}} \rangle \langle u_{v\mathbf{k}} | u_{c\mathbf{k}+q\mathbf{e}_j} \rangle, \quad (2.63)$$

where  $\Omega$  represents the volume of the cell, and  $\mathbf{e}_{i,j}$  are the unit vectors along three directions. In Eq. 2.63,  $q$  stands for one direction of the unit vector defined as  $\hat{\mathbf{q}} = \mathbf{q}/|\mathbf{q}|$ , where  $\mathbf{q}$  is the Bloch vector of the incident wave, and  $w_{\mathbf{k}}$  is the  $k$ -point weights.  $c$  and  $v$  refer to the conduction and valence states, respectively. The conduction band energy is denoted by  $\epsilon_{c\mathbf{k}}$ , while the valence band energy is denoted by  $\epsilon_{v\mathbf{k}}$ . The cell periodic part of the orbitals at the  $k$ -point  $\mathbf{k}$  is represented by  $u_{c\mathbf{k}}$ . The real part, denoted as  $(\epsilon_1^{ij})$ , is obtained through the Kramers-Kronig transformation using Eq. 2.64:

$$\varepsilon_1^{ij} = 1 + \frac{2}{\pi} \int_0^\infty \frac{\varepsilon_2^{ij}(\omega')\omega'}{\omega'^2 - \omega^2} d\omega'. \quad (2.64)$$

Both perpendicular (in-plane polarization, represented as  $ij = xx$ ) and parallel (out-of-plane polarization, represented as  $ij = zz$ ) components are calculated by considering a single k-point at  $\Gamma$  point ( $1 \times 1 \times 1$ ).

The complex dielectric function is associated with both the refractive index ( $n$ ) and the extinction coefficient ( $\kappa$ ) as  $n(\omega) + i\kappa(\omega) = \sqrt{\varepsilon(\omega)}$ . Thus, the extinction coefficient can be expressed as  $\kappa(\omega) = \left( \frac{\sqrt{\varepsilon_1(\omega)^2 + \varepsilon_2(\omega)^2} - \varepsilon_1(\omega)}{2} \right)^{1/2}$ . The absorption coefficient is related to the extinction coefficient through the equation  $\alpha(\omega) = 2\omega\kappa(\omega)/c$ , where  $c$  represents the speed of light in a vacuum [102]. As a result, the refractive index can be defined as Eq. 2.65:

$$n(\omega) = \left( \frac{\sqrt{\varepsilon_1(\omega)^2 + \varepsilon_2(\omega)^2} + \varepsilon_1(\omega)}{2} \right)^{\frac{1}{2}}. \quad (2.65)$$

The electron energy loss spectrum (EELS) can be computed using the imaginary component of the dielectric function as shown in Eq. 2.66:

$$L(\omega) = -Im\left(\frac{1}{\varepsilon(\omega)}\right) = \frac{\varepsilon_2(\omega)}{\varepsilon_1(\omega)^2 + \varepsilon_2(\omega)^2}. \quad (2.66)$$



## Part II:

### Summary of the Results





### 3. Tuning the Lattice Thermal Conductivity of Metallic Glasses

Metallic glasses are materials that lack long-range order in their atomic structure. They have a wide range of industrial applications due to their remarkable stiffness, durability, and low thermal conductivity [8, 9, 10]. One way to enhance their performance is by forming nanostructures to manipulate lattice thermal conductivity [14, 103, 104, 105, 17, 18]. Pressure and temperature are other external factors that can affect thermal conductivity [106, 107]. In my first paper, I focused on tuning the lattice thermal conductivity of  $\text{Fe}_{0.85}\text{Zr}_{0.15}$  metallic glasses by introducing nanostructured spherical voids with varying radii. We studied the effects of temperature and pressure on these void-including structures, as well as the contributions of perfect and distorted icosahedra in these structures.

#### 3.1 Structural Analysis

We used the same glass-production procedure defined in page 18 in Fig. 2.1. Equilibrium simulations were conducted using both FPMD and CMD methods. A supercell of BCC-Fe with 432 atoms was used, with 64 Fe atoms randomly replaced by Zr atoms to achieve a Zr content of 14.81 %, close to the target of 15 %. Benchmark calculations were performed to compare the results produced by FPMD and CMD. A 432-atom cell was chosen as a balance between accuracy and efficiency. RDF and Voronoi Tessellation were used to analyze the structures Fig. 3.1.

The RDF plots in Fig. 3.1 (b) display a reduction in long-range order and a double peak, which is a common trait of a random closed-packed structure, such as metallic glasses. A Gaussian fit to the first RDF peak reveals a nearest neighbor distance of 2.33 Å which is consistent with the calculated Fe-Fe nearest neighbor distance. The Fe-Zr nearest neighbor distance is found to be 2.67 Å.

In Fig. 3.1(c), displays the calculated Voronoi tessellations for structures produced by using CMD and FPMD simulations. The highest fraction of Voronoi tessellation corresponds to the perfect icosahedron,  $\langle 0, 0, 12, 0 \rangle$ , with a coordination number of 12. The next highest fraction has a distorted icosahedral,  $\langle 0, 1, 10, 2 \rangle$ , with one additional neighbor atom. On average, Fe atoms have 12-13 geometrical neighbors, while Zr atoms have 15-16, which

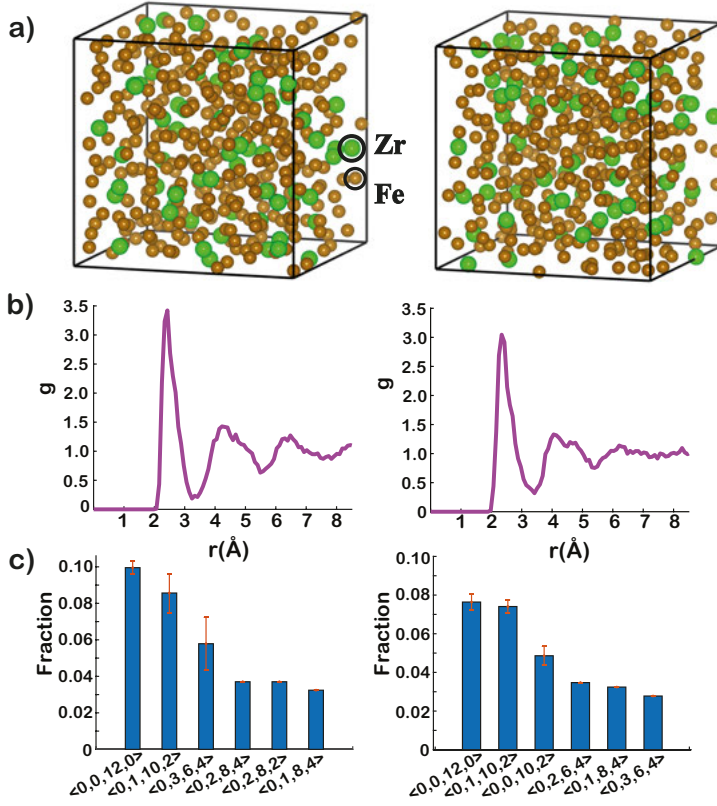


*Figure 3.1.* a) The image on the left shows the simulated structure of  $\text{Fe}_{0.85}\text{Zr}_{0.15}$  metallic glass using CMD, while the image on the right shows the structure using FPMD. Brown and green balls represent Fe and Zr atoms, respectively. b) The Radial Distribution Function (RDF) of the glass at 300 K is shown for both CMD (left) and FPMD (right). c) The final glass structures produced with CMD and FPMD are shown using Voronoi tessellations on the left and right, respectively.

is consistent with previous findings that Zr has a larger free volume than 3d atom [108]. The calculated fractions of Voronoi tessellations differ slightly between CMD and FPMD. CMD results in a higher fraction of perfect icosahedron. The calculated equilibrium lattice constant for (Fe<sub>0.85</sub>Zr<sub>0.15</sub>) is 5 % larger for CMD than for FPMD. In CMD simulations, the EAM pairwise potential results in a larger atomic sphere radius for Fe and Zr than in FPMD. CMD calculations give a higher filling factor than Wang et al. [109] calculated filling factor of 0.637 for the random closed packed structure where the occurrence of the perfect icosahedron is at maximum.

The structure was also tested as a function of system size using 6750 atoms by using CMD.

System (N)	Types	CN	VP	Fraction
432	Full icosahedral	12	< 0, 0, 12, 0 >	0.088
	Distorted icosahedral	13	< 0, 1, 10, 2 >	0.088
		12	< 0, 2, 8, 2 >	0.044
		15	< 0, 1, 10, 4 >	0.019
		13	< 0, 2, 8, 3 >	0.019
		14	< 0, 1, 10, 3 >	0.016
		16	< 0, 1, 10, 5 >	0.016
	Distorted BCC	14	< 0, 3, 6, 4 >	0.076
	Distorted BCC	14	< 0, 2, 8, 4 >	0.051
	Distorted FCC	14	< 0, 4, 4, 6 >	0.016
6750	Full icosahedral	12	< 0, 0, 12, 0 >	0.088
	Distorted icosahedral	13	< 0, 1, 10, 2 >	0.087
		12	< 0, 2, 8, 2 >	0.035
		14	< 0, 1, 10, 3 >	0.018
		15	< 0, 1, 10, 4 >	0.016
		13	< 0, 2, 8, 3 >	0.015
		16	< 0, 1, 10, 5 >	0.001
	Distorted BCC	14	< 0, 3, 6, 4 >	0.067
	Distorted BCC	14	< 0, 2, 8, 4 >	0.033
	Distorted FCC	14	< 0, 4, 4, 6 >	0.001

**Table 3.1.** The short-range ordering fractions of large and relatively smaller cells are compared using the Voronoi tessellation method. CN and VP stand for coordination number and Voronoi polyhedra, respectively.

We found that RDF peak positions are in good agreement with the larger system size. A detailed analysis of local structures for two system sizes is shown in Table 3.1, where the coordination numbers and fraction of Voronoi polyhedra are similar for both sizes. When comparing the MG produced by FPMD and CMD, the FPMD is slightly better in terms of both the lack of long-

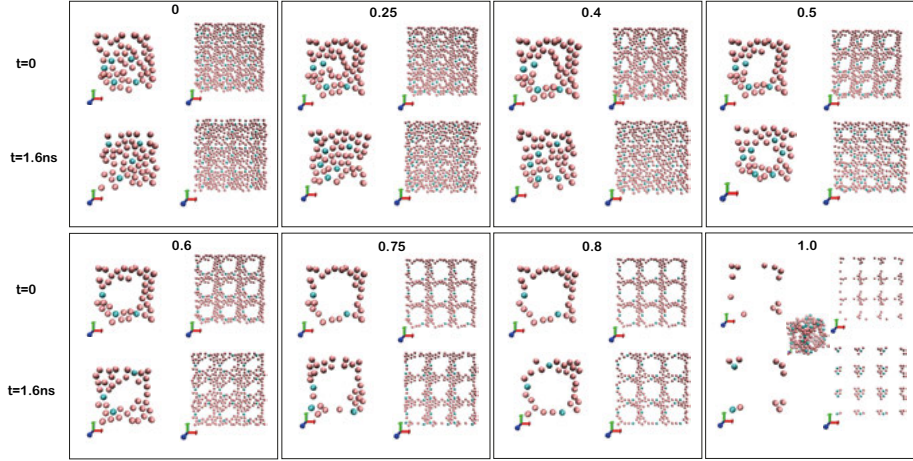


*Figure 3.2.* We calculated slices of the MGNV with a thickness of 2 Å for various void diameters using NVT-CMD. For each void size, we display the initial configuration ( $t=0$ ) in the top panel and the atomic positions within the same slice after  $t=1.6$  ns in the bottom panel. The slice of the unit cell is shown on the left, while the slice of the  $3 \times 3$  periodically repeated unit cell is shown on the right. For the void diameter of 1.0, we also include a plot of the full cell in the middle to highlight that the void structure remains connected.

range order and the splitting of the second peak. Therefore FPMD produced structure is used for the nanostructuring of voids.

### 3.2 Nanostructuring Stable Voids

Metallic glasses with nanostructured voids (MGNV) were generated by forming spherical voids through the removal of atoms within a shell of radius  $R_{void}$  at the cell's center, following the relaxation of the bulk system's volume (where the lattice vector was calculated as ( $a_{CMD} = 17.58$  Å) at the end). We then carried out NVT simulations at a constant temperature of 300 K to assess the stability of the voids. Our findings indicate that void stability is dependent on void size. The two smallest voids, with  $2R_{void}$  values of  $0.25a$  and  $0.4a$ , corresponding to the removal of 1 % and 3 % of atoms, respectively, were found to be unstable. Furthermore, all stable voids altered their shape from spherical to prolate ellipsoidal, but they remained clearly visible after 1.6 ns of MD simulation, as depicted in Fig. 3.2

### 3.3 Lattice Thermal Conductivity

We also followed the same NVT steps applied for voids at 300 K for the bulk system. Then, we followed the 2 ns NVE thermal equilibration step and used

Ensemble	Density( $\text{u}/\text{\AA}^3$ )	Volume( $\text{\AA}^3$ )	N	$\kappa$ (W/m·K)
NVT	4.86	5435.13	432	$1.26 \pm 0.08$
NVT	4.86	84923.89	6750	$1.26 \pm 0.08$
NPT	$\sim 4.84$	$85198.23 \pm 11.45$	6750	$1.27 \pm 0.08$

**Table 3.2.** Thermal conductivity comparison between large and smaller cells using NVT and NPT ensembles with a constant composition of  $\sim 85\%$  Fe and  $\sim 15\%$  Zr at 300 K.

sphere diameter ( $a_{CMD}$ )	$N_0$	Fe %	Zr %	b	$\kappa_{GK}$ (W/m·K)
0	432	85.19	14.81	0	$1.27 \pm 0.10$
0.25	428	85.28	14.72	0.01	$1.20 \pm 0.09$
0.4	419	84.96	15.04	0.03	$1.11 \pm 0.10$
0.5	405	85.19	14.81	0.06	$0.97 \pm 0.08$
0.6	388	85.31	14.69	0.10	$0.96 \pm 0.08$
0.75	338	85.21	14.79	0.22	$0.71 \pm 0.08$
0.8	318	84.91	15.09	0.26	$0.72 \pm 0.07$
1.0	206	83.01	16.99	0.52	$0.28 \pm 0.04$

**Table 3.3.** MGNV were designed from  $\text{Fe}_{0.85}\text{Zr}_{0.15}$  MG (represented with 0) by extracting atoms from the unit cell to form central spherical voids of different diameters, measured in units of the lattice vector length  $a_{CMD}$  (in the first column). The following columns show the remaining atoms ( $N_0$ ), the glass composition of MGNV with Fe ( $N_{Fe}$ ) and Zr ( $N_{Zr}$ ) atoms, porosity as the ratio of extracted atoms to the total number of atoms in the MG without a void inside, and calculated thermal conductivities with uncertainties.

the Green-Kubo thermal conductivity method for all of the systems. First, the thermal conductivity of the bulk MG was calculated as  $\kappa = 1.27 \pm 0.10$  (W/m·K). We obtained the same value of  $\kappa$  for both the CMD quenching-produced MG structure, MG (CMD), and the FPMD quenching-produced MG structure, MG (FPMD). We investigated the effect of system size on the calculated thermal conductivity by increasing the system size 2.5 times while maintaining constant density and following the steps outlined in the production and MD procedures. Our results indicated that system size has a negligible impact on thermal conductivity. We further analyzed our small system by comparing its thermal conductivity with that of a larger system calculated using NPT, in order to continue using a small system size. All of our analyses support the conclusion that thermal conductivity can be reliably calculated using our obtained volume, which includes 432 atoms, as shown in table 3.2.

In Fig. 3.3 and Table 3.3, calculated lattice thermal conductivity of MGNV's is represented by  $b = n/N_0$ , where  $n$  is the number of atoms removed to create the initial void and  $N_0$  is the number of atoms in the MG without a void. Fig. 3.3, the vertical bars indicate uncertainty. The solid line represents

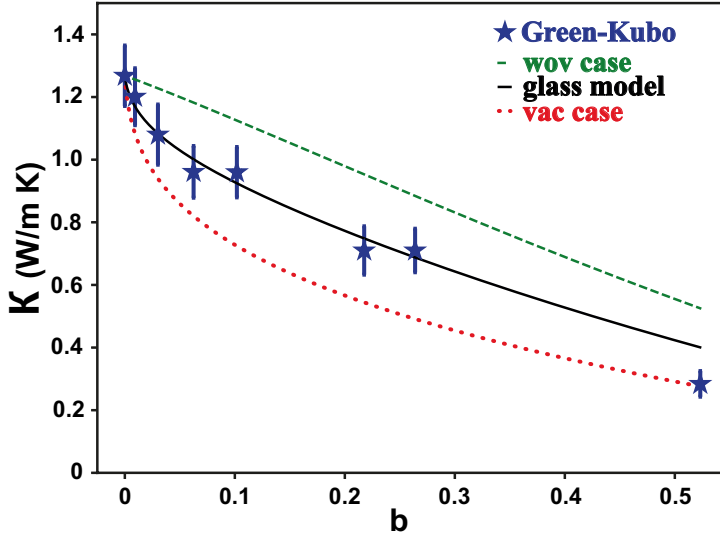


Figure 3.3. Calculated Green-Kubo thermal conductivity (blue) is shown as a function of  $b = n/N_0$ , where  $n$  is the number of extracted atoms creating the initial void and  $N_0$  is the number of atoms in the voidless MG. Uncertainty is represented by vertical bars. The solid line represents the glass model (Eq.3.3), the dashed line displays one limit case without voids (*wov*) (Eq.3.1), and the dotted line displays the other limit case with a continuous vacuum (*vac*) (Eq.3.2).

the glass model (Eq.3.3), while the dashed line shows one limit, without voids (wov) (Eq.3.1), and the dotted line shows the other limit, vacuum continuous (vac) (Eq.3.2). The first limiting case is without voids (wov), where the atoms are packed with a vacuum between them (wov case), and the second limit is vacuum continuous (vac), where no atoms exist (vac case). For the wov case,  $\kappa_{wov}$  is expressed as a function of voids:

$$\kappa_{wov}(b) = \kappa_0 \frac{b^{\frac{2}{3}} + \frac{\kappa_0}{\kappa_V} (1 - b^{\frac{2}{3}})}{b^{\frac{2}{3}} - b + \frac{\kappa_0}{\kappa_V} (1 - b^{\frac{2}{3}} + b)}, \quad (3.1)$$

where  $\kappa_V = 0.0$  (W/m·K) represents the thermal conductivity of vacuum, while  $\kappa_0$  is a scaling factor equal to the calculated value of  $\kappa$  for the  $\text{Fe}_{0.85}\text{Zr}_{0.15}$  MG. The wov case is depicted as a green dashed line in Figure 3.3. For the vac case model,  $\kappa_{vac}$  is defined as follows:

$$\kappa_{vac}(b) = \kappa_0 \frac{b^{\frac{2}{3}} - b + \frac{\kappa_V}{\kappa_0} (1 - b^{\frac{2}{3}} + b)}{b^{\frac{2}{3}} + \frac{\kappa_V}{\kappa_0} (1 - b^{\frac{2}{3}})}. \quad (3.2)$$

The vac case of the model is represented by the red dotted line in Figure 3.3. For small voids,  $\kappa_{vac}$  exhibits a steep linear decrease that eventually levels off. In contrast to the wov case, the vacuum and without void structures are reversed. As Russel noted, this is unstable, but we can assume that the structures are connected at corners or a limited number of points. The model accurately predicts the limiting behavior for both cases (wov and vac), with  $\kappa_{wov} = \kappa_{vac} = \kappa_0$  when  $b = 0$  and  $\kappa_{vac} = \kappa_{wov} = \kappa_V$  when  $b = 1$ . This model does not contain any fitting parameters. The two cases of the model define the range within which we expect thermal conductivities to fall. For a given void size, a material cannot have a lower thermal conductivity than the vacuum model, as this lower bound implies a situation where the material is in a vacuum and the number of conduction pathways through the material is minimal. Conversely, for a given porosity, a material cannot have a higher thermal conductivity than the voidless model, as this upper bound implies a situation where the vacuum is immersed in the system and the number of conduction pathways through the material is maximized. Consistent with this interpretation, all of our calculated values of  $\kappa$  fall within the range defined by the two limiting cases of the models. This can be seen in Fig.3.3, where all of the blue stars (representing calculated values of  $\kappa$ ) lie between the dashed and dotted lines. Furthermore, the calculated values of  $\kappa$  are best described by a linear combination of the solid continuous (wov) and air continuous (vac) cases which we described as a ‘glass model’:

$$\kappa(b) = \frac{1}{2}(\kappa_{wov} + \kappa_{vac}). \quad (3.3)$$

The glass model accurately predicts the dependence of thermal conductivity on voids. As expected,  $\kappa$  decreases as void size (Table 3.3). The calculated value

of  $\kappa$  with the largest void ( $b=0.52$ ) is more consistent with the *vac* case of the Brick model. From Figure 3.2, we can see that the structure with the largest void (void diameter 1.0) is indeed disconnected along the shown slice, unlike the other voids. However, it is important to note that the structure remains connected along the frame, and the MG is stable. We can conclude that in the *wov* case, conduction is determined solely by pathways through the material, with more pathways existing at higher densities. In contrast, in the *vac* case, conduction is primarily determined by the few remaining pathways between the remaining material, with very few pathways through the air and none in the limit of vacuum. An ordered material will have more pathways than a disordered material. Therefore, the inclusion of voids in a disordered material can be viewed as a case between the *wov* and *vac* cases of the models. The glass model, Eq.3.3, suggest a superposition of two limit cases that may be applicable to a wide range of ordered and disordered materials that include voids.

### 3.4 Vibrational Properties

The number of atoms in the cell directly affects the thermal conductivity of MGNV. The decrease in thermal conductivity is due to the localized modes formed by voids. Analyses of vibrational density of states ( $g(\omega)$ ),  $PR$  and  $\Delta PR$  were performed for four cases with void diameters of 0.25, 0.5, 0.75, and 1.0 times the lattice vector. The  $g(\omega)$  and  $\Delta g(\omega)$  plots show a red-shift with a decreasing number of atoms in the cell and an increase until 7 THz followed by a decrease. The detailed analyses can be seen in the  $PR$  and  $\Delta PR$  plots. Locons become largely dominant from 8 to 14 THz. Large voids with diameters of 0.75 and 1.0 show more distinct behavior in increasing locon modes than systems with smaller voids.

### 3.5 Temperature and Pressure Effect on Lattice Thermal Conductivity

The sensitivity of lattice thermal conductivity of the systems relative to the system size was studied under three different pressures at 300 K. The volume of the 432 atom system at ambient pressure, denoted as 0P), was 5433.21 Å<sup>3</sup>. Positive pressure (PP) caused a volume shrink of approximately  $\sim 4.65\%$ , while negative pressure (NP) resulted in a volume increase of approximately  $\sim 1.72\%$ .

Table 3.4 indicates that thermal conductivity is not significantly affected by system size. Both large and small systems exhibit similar trends of decreasing conductivity under negative pressure and increasing conductivity under positive pressure. Our findings also show that temperature does not impact thermal



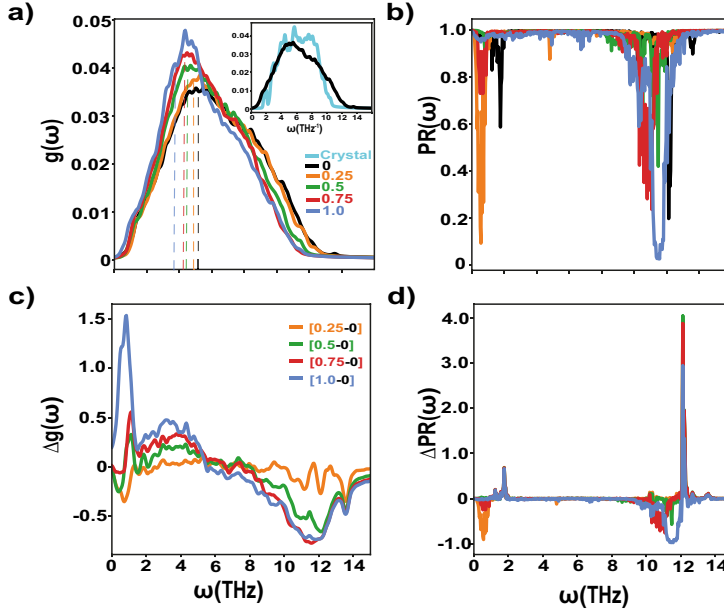


Figure 3.4. a) Vibrational densities of states for voids of varying diameters: 0; 0.25; 0.5; 0.75 and 1.0. Dashed lines indicate dominant peaks. b) Calculated participation ratios for the voids. Normalized vibrational densities of states, obtained by subtracting the ‘0-VDOS’ and dividing by ‘0-VDOS’, showing a red shift with increasing void diameter. d) Normalized participation ratios, obtained by subtracting the ‘0-PR’ and dividing by ‘0-PR’, showing an increase in localized modes with increasing void diameter.

System (N)	Pressure	Volume ( $\text{\AA}^3$ )	$\kappa$ (W/m·K)
432	PP	5180.45	$1.41 \pm 0.08$
	0P	5435.13	$1.26 \pm 0.08$
	NP	5526.46	$1.13 \pm 0.08$
6750	PP	80944.51	$1.41 \pm 0.08$
	0P	84923.89	$1.26 \pm 0.08$
	NP	86350.89	$1.17 \pm 0.08$

**Table 3.4.** Thermal conductivity values for large and smaller cells under positive (PP), zero (0P), and negative (NP) pressures, causing respective volume changes of approximately  $\sim 4.65\%$  decrease, no change, and  $\sim 1.72\%$  decrease at 300 K.

System (N)	Temperature	$\kappa$ (W/m·K)
432	200	$1.19 \pm 0.08$
	300	$1.26 \pm 0.08$
	500	$1.28 \pm 0.08$
	700	$1.26 \pm 0.08$
6750	200	$1.21 \pm 0.08$
	300	$1.26 \pm 0.08$
	500	$1.26 \pm 0.08$
	700	$1.29 \pm 0.08$

**Table 3.5.** Thermal conductivities for two system sizes under zero pressure (0P) at temperatures of 200 K, 300 K, 500 K, and 700 K.

conductivity. As shown in Tables 3.4 and 3.5, the small systems' thermal conductivity is influenced by pressure, but not temperature. We selected the small system to study the effects of voids, pressure, and temperature while maintaining constant density and void size for reliable comparison.

Table 3.6 shows that the thermal conductivity of MGNV is affected by pressure and less so by temperature. This suggests that thermal conductivity can be tailored by creating nanostructured voids of different diameters. We aimed to fine-tune thermal conductivity by combining pressure and voids, using the same void diameters and three defined pressure values (PP, 0P, and NP). The results are presented in Table 3.6 and Fig. 3.5. At 300 K and under PP, all structures show an increase in thermal conductivity of approximately  $\sim 0.2$ (W/K.m), while under NP some structures (0.5, 0.75, 1.0) show a small decrease due to less local structural changes. Thus, it can be concluded that thermal conductivity can be adjusted by creating voids and applying external pressure, resulting in a change of roughly  $\pm 10 - 15$  %.

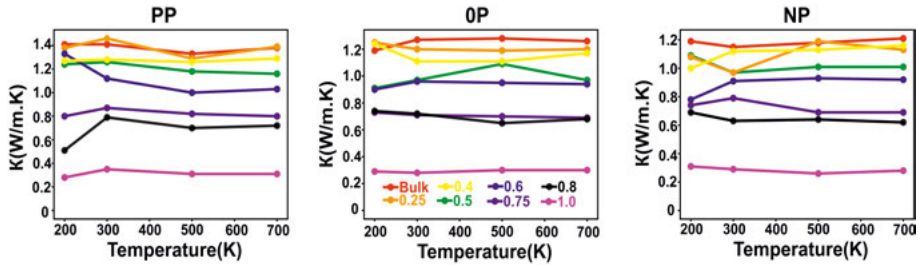


**Figure 3.5.** Thermal conductivity as a function of temperature for systems with voids under a) positive pressure of 137 GPa, b) zero pressure, and c) negative pressure of -5 kBar.

Void Diameter	Pressure	$\kappa(W/m \cdot K)$			
		200 K	300 K	500 K	700 K
bulk	PP	1.41	1.41	1.33	1.38
	OP	1.19	1.26	1.28	1.26
	NP	1.19	1.15	1.18	1.21
0.25	PP	1.38	1.46	1.29	1.39
	OP	1.25	1.20	1.19	1.20
	NP	1.08	0.97	1.19	1.13
0.4	PP	1.27	1.28	1.26	1.29
	OP	1.24	1.11	1.11	1.17
	NP	1.0	1.12	1.13	1.16
0.5	PP	1.24	1.26	1.18	1.16
	OP	0.91	0.97	1.09	0.97
	NP	1.09	0.97	1.01	1.01
0.6	PP	1.33	1.12	1.00	1.03
	OP	0.90	0.96	0.95	0.94
	NP	0.78	0.91	0.93	0.92
0.75	PP	0.80	0.87	0.82	0.80
	OP	0.73	0.71	0.70	0.69
	NP	0.74	0.79	0.69	0.69
0.8	PP	0.51	0.79	0.70	0.72
	OP	0.74	0.72	0.65	0.68
	NP	0.69	0.63	0.64	0.62
1.0	PP	0.28	0.35	0.31	0.31
	OP	0.29	0.28	0.30	0.30
	NP	0.31	0.29	0.26	0.28

**Table 3.6.** Thermal conductivities as a function of void size under PP, OP, and NP pressures at varying temperatures.

### 3.6 Temperature and Pressure Effect on Vibrational Properties of MGNV

We demonstrated that temperature has little effect on thermal conductivity. This can be further examined by analyzing the vibrational density of states (VDOS) and the corresponding participation ratio (PR). Our calculations show that the VDOSs for two different system sizes (432 atoms and 6750 atoms including systems at 300 K) are qualitatively similar. We determined that the smaller system size is suitable for further analysis of vibrational characteristics. We also calculated the mode participation ratio to determine the contribution of specific atoms to heat transport. To do this, we selected atoms located in spherical shells of increasing diameter from the center of the cell. We found that the frequency of heat carriers shifted and the number of localized modes decreased in all shells from 200 to 700 K under NP, PP. At 200 K, both positive and negative pressures caused an increase in localized modes. Positive pressure resulted in a slight blue shift in the frequencies of the modes, while negative pressure caused a relatively larger blue shift. Interestingly, temperature-dependent changes did not result in an increase in thermal conductivity with increasing temperature. On the other hand, pressure had a more significant impact on both VDOS and PR in shells. While PP caused a spread in frequency in the diffusion regime for all shells, NP resulted in the creation of more locon peaks. This supports the idea that thermal conductivity can be fine-tuned with pressure. The shift in frequency and sharp changes in the modes of the outer shell with pressure show the effect of local structural ordering. At 200 K, where localized modes are prominently visible, the modes at around 10 to 12 Hz mainly arise from perfect icosahedra, distorted icosahedra, and distorted BCC structures. However, the dominance of localized modes decreases with increasing temperature. The selected SROs are mostly present outside the 0.5 shell radius and contribute to non-propagating modes, resulting in a decrease in heat conductivity. To observe locons modes in MGNV, we chose to work at 200 K under PP. In Fig. 3.6, The presence of voids causes a red-shift in VDOS frequency, which in turn increases the intensity of the first peak, similar to the VDOS observed at NP. This effect becomes more pronounced as the void size increases from bulk to 0.75 voids. In the case of 0.25 voids, the PR indicated that inner shell atoms, rather than outer shell atoms, contributed to localized modes. This transition between atoms disappears as the void size increases. The observed transition may be due to the reorientation of inner atoms relative to the void size. The PR indicates that the contribution of SROs supports the idea that Distorted Icos and BCCs contribute to localized modes as their density increases relative to the bulk. Interestingly, at 200 K, the outer shells of 0.5 voids give rise to soft localized modes, which is unexpected at high temperatures. This effect is not observed in the SROs' PR. However, the contribution of different SROs to localized modes increases with size, while the full icosahedral contribution becomes visible. In the case of 0.75 voids, the density of

perfect and distorted icosahedra increases because they are mostly located in the outer shell, and their contribution to localized modes also red-shifts.

### 3.7 Conclusion of Paper I

We investigated the potential for tailoring thermal conductivity by introducing nanostructured voids and assessed the stability of these structures. Our findings show that thermal conductivity decreases with increasing  $b$ , but not with void size directly. Our calculated thermal conductivities fall within the range defined by the glass model. For a given  $b$ , the atomic structural details determine the thermal conductivity relative to the glass model. We also analyzed vibrational modes and participation ratios to establish a link between an increase in localized vibrational modes and a decrease in thermal conductivity as void size increases.

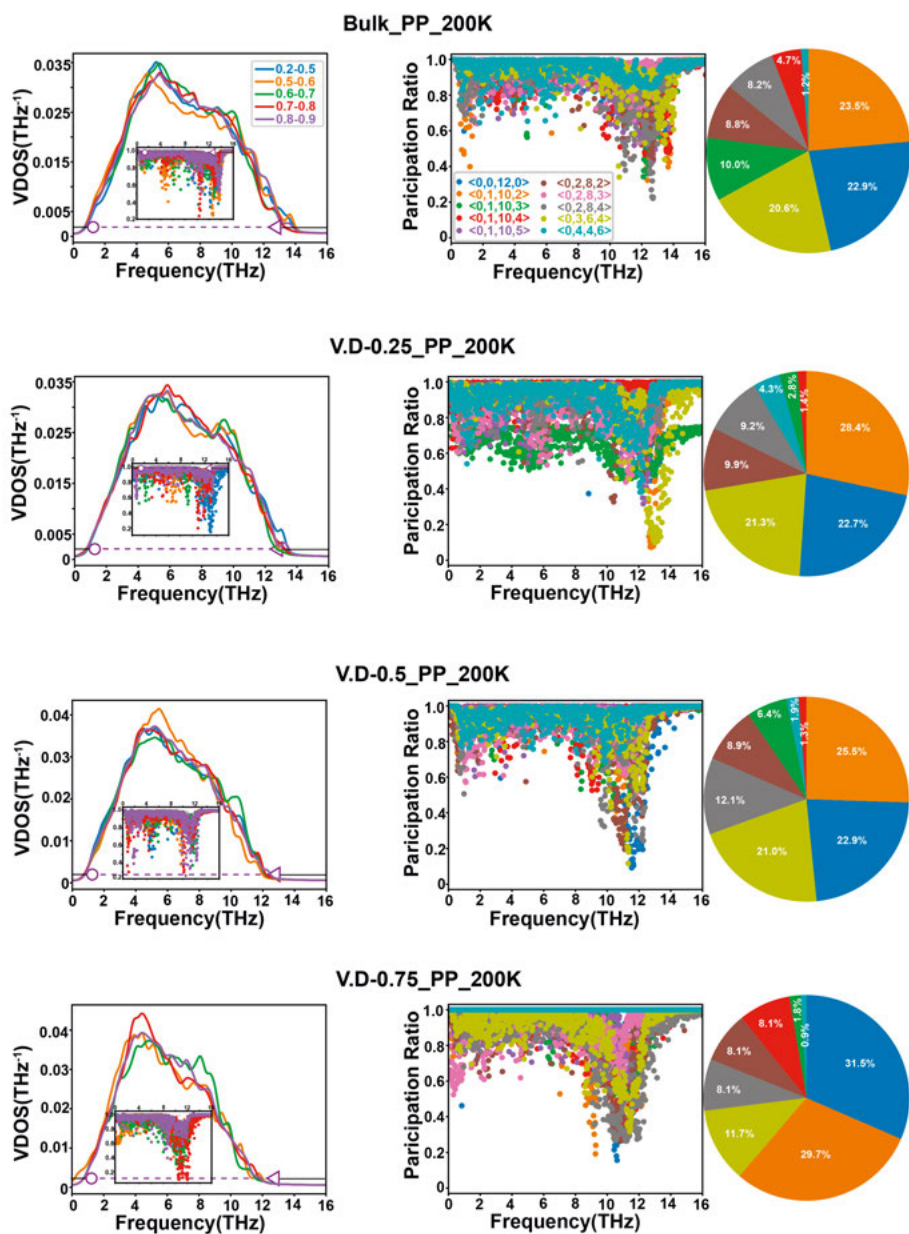


*Figure 3.6.* Shell-wise VDOS (left) and PR (right) plots for selected atoms in bulk and void systems of 0.25, 0.5, and 0.75 diameters at 200 K under positive pressure (PP). Insets present corresponding shell-wise PRs. Pie plots show the distribution of SROs, with colors matching the PR plots on the right.

## 4. Structure Dependant Magnetic Properties of Amorphous $\text{Co}_x\text{Zr}_{100-x}$ films

The use of amorphous alloys as precursors for the production of magnetically soft nanocrystalline materials has become a common practice in various applications [24, 110]. In amorphous Co-Zr-based alloys, the magnetic ordering temperature  $T_c$  and saturation magnetization  $M_s$  generally exhibit a linear increase with the concentration of Co. This increase begins at a critical concentration, typically between 40 – 60 at. % Co atomic percent [24, 23]. It is intriguing to consider if the magnetic properties of pure amorphous Co can be identified by extrapolating the Co content to 100 at. % atomic percent for this system. In my second paper, We investigated how the composition of amorphous  $\text{Co}_x\text{Zr}_{100-x}$  thin films, with  $60 \leq x \leq 70$  at. %, affects their magnetic moment, ordering temperature, and effective interaction strength. We used DFT calculations to interpret our experimental observations and to understand how local order and composition influence the macroscopic properties of these amorphous alloys.

### 4.1 Structural Analysis of $\text{Co}_x\text{Zr}_{100-x}$ Films

We produced glasses by following the recipe, randomly distributing 432 atoms in a cubic lattice relative to the experimentally obtained densities for each system with 40 – 95 at. % Co concentration, using CMD and EAM potential. The quality of the produced metallic glasses structure was verified using the  $\text{Co}_{65}\text{Zr}_{35}$  as a test case, through FPMD. The RDF plots showed the first peak

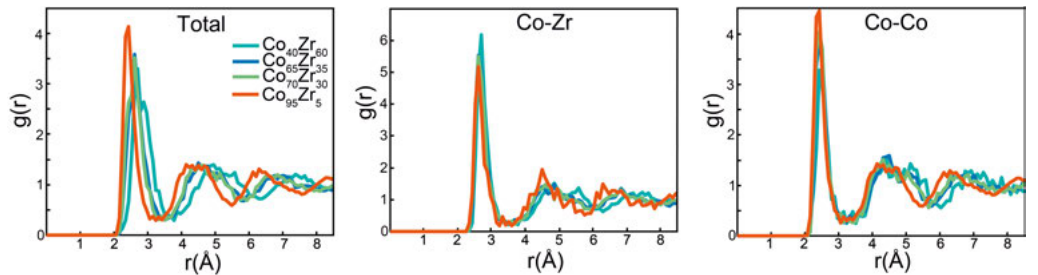


Figure 4.1. Analysis of total and partial RDF of selected compositions from the structures.

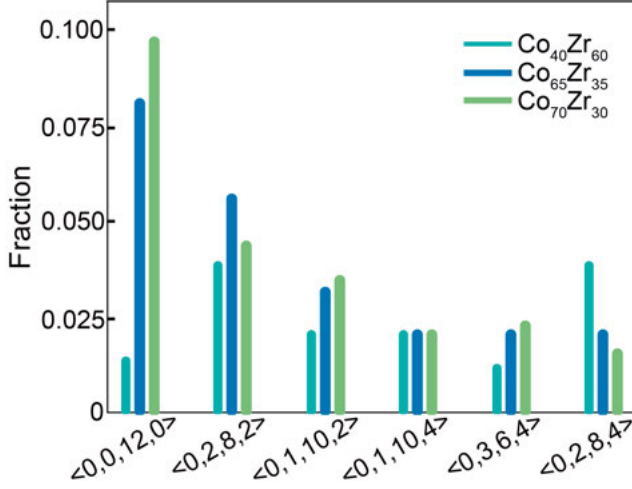


Figure 4.2. Voronoi tessellation of MG structures with 40, 65, and 70 at. % Co content.

position for both at  $\sim 2.60$  Å, whereas CMD voronoi tessellation showed the perfect icosahedron ratio 0.33 more than FPMD produced glass. Therefore, we selected the CMD method for  $\text{Co}_x\text{Zr}_{100-x}$  MG films. The total and partial RDF plots for 40, 65, 70, and 95 at. % Co content are represented in Fig. 4.1. As the Co content increases,  $g(r)$  shifts towards smaller distances, consistent with the GIXRD findings. This shift enhances the visibility of the double-peak feature in  $g(r)$ , a fingerprint of Zr-based metallic glasses.

The short-range local ordering analysis was performed on structures with 40, 65, and 70 at. % Co for selected SROs. These include perfect icosahedra ( $\langle 0, 0, 12, 0 \rangle$ ); distorted icosahedra ( $\langle 0, 2, 8, 2 \rangle$ ;  $\langle 0, 1, 10, 2 \rangle$ ;  $\langle 0, 1, 10, 4 \rangle$ ; etc.); FCC-types ( $\langle 0, 2, 8, 4 \rangle$ ; etc.); BCC-types ( $\langle 0, 3, 6, 4 \rangle$ ; etc.), as shown in Fig. 4.2. Perfect icosahedra and distorted icosahedra motifs increase with increasing Co content from 65 to 70 at. % Co content Fig. 4.2. A detailed motif analysis is presented in Fig. 4.3.

The presence of various motifs at different Co concentrations results in significant variations. This suggests that alterations in the material's physical properties can be attributed to changes in its local configuration. It's important to mention that the change in local structure patterns based on the amount of Co may not be seen clearly in this case. This is partly because of the magnetic properties and partly because the size of the samples used in the simulations is limited.

## 4.2 Magnetic Properties of $\text{Co}_x\text{Zr}_{100-x}$ Films

The saturation magnetization,  $M_s$ , as a function of Co content,  $x$ , is presented in Fig. 4.4, with both experimental (SQUID) and theoretical (DFT) results.



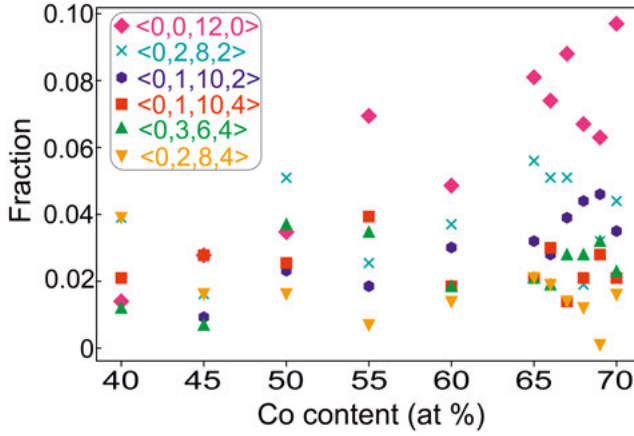
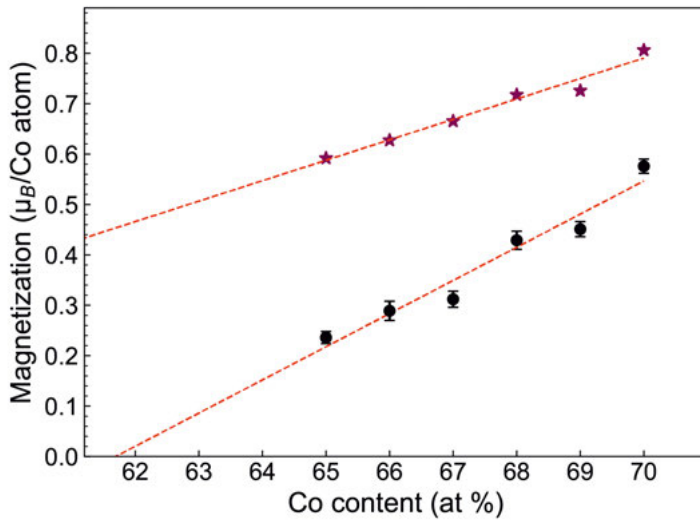


Figure 4.3. Analysis of Voronoi polyhedra of selected compositions from the structures obtained from CMD simulations.

The discrepancy between the theoretical and experimental results could be due to the choice of exchange and correlation functional in DFT or the limited size of the sample used in our simulations. Nonetheless, both data sets show a linear increase in  $M_s$  with  $x$  within the studied composition range. Extrapolating the linear dependence to pure Co ( $x = 100$  at. %) yields an effective moment per Co atom of  $2.5 \mu_B$  from experiments and  $2.0 \mu_B$  from DFT calculations, both of which are higher than the hcp Co moment ( $1.55 \mu_B$ ) [111]. The experimental data's linear fit intersects the point where  $M_s = 0$  at an atomic percentage of  $x = 61.5$  at. % ( $x = 50.6$  at. % for calculated  $M_s$ ), which is consistent with the observation that the sample with an atomic percentage of  $x = 60$  at. % is nonmagnetic at a temperature of 5 K.

### 4.3 Conclusion of Paper II

In the  $\text{Co}_x\text{Zr}_{100-x}$  alloys, a linear relationship was observed between the saturation moments and the Co concentration, for concentrations ranging from ( $65 \leq x \leq 70$  at. %) atomic percent. Using Voronoi polyhedra analysis, we found that the coordination numbers of Co atoms vary with concentration. We observed a correlation between changes in effective coupling and coordination number of Co with composition. However, we cannot establish a causal relationship between these observations.



*Figure 4.4.* The relationship between saturation magnetization  $M_s$ , expressed as the magnetic moment per Co atom, and Co content is shown. Data points are represented by stars which were calculated using DFT at 0 K, and circles which were measured using SQUID at 5 K), while linear fits are indicated by dashed red lines.

## 5. Superconductivity of Amorphous $\text{Mo}_x\text{Ge}_{100-x}$ systems

The lattice periodicity of crystalline materials allows for the utilization of reciprocal space, leading to a well-established theoretical understanding of phonon-mediated superconductivity in these materials. However, amorphous materials can exhibit superconductivity despite their disordered nature. Kim et al. [25], have shown that amorphous  $\text{Mo}_x\text{Ge}_{100-x}$  can be a superconductor. In amorphous alloys, the absence of crystal symmetries necessitates a thorough comprehension of local geometries and their role in the coupling between electronic and vibrational degrees of freedom. Our aim in this paper is to investigate superconductivity in amorphous  $\text{Mo}_x\text{Ge}_{100-x}$  by calculating electron-phonon coupling parameters within the context of local electronic structures.

### 5.1 Structural Modelling and Vibrational Analysis of $\text{Mo}_x\text{Ge}_{100-x}$ Systems

We produced amorphous  $\text{Mo}_x\text{Ge}_{100-x}$ , where  $x$  was selected as 70, 50, and 30, by using first-principles molecular dynamics. A total of 432 atoms were used to create three different concentrations of Mo-Ge alloys. The initial structure was a BCC unit cell with randomly distributed Ge atoms. The unit cell volumes remained constant after the structural optimizations. The amorphous structures are produced by following the defined recipe in the glass section.

RDF ( $g(r)$ ) and Voronoi tessellations were used as structural analysis tools as shown in Fig. 5.1. The first RDF peak of  $\text{Mo}_{70}\text{Ge}_{30}$  was found at 2.61 Å, which is in line with the first peak of the Mo-Ge distance. The second RDF peak is a double peak, a common feature in many binary metallic glasses where there is a difference in mass between the constituent elements [54]. The double peak positions for  $\text{Mo}_{70}\text{Ge}_{30}$  are located at approximately 4.59 and 5.32 Å, where the total and partial RDF plots are in agreement. For  $\text{Mo}_{50}\text{Ge}_{50}$ , the first peak is located at approximately 2.60 Å, whereas the double peak is located at 4.77 and 5.58 Å. Compared to  $\text{Mo}_{70}\text{Ge}_{30}$ , the first peak location is conserved, but an increase in Ge concentration causes a shift in the double peak position and distortion into large, slightly merged peaks. For  $\text{Mo}_{30}\text{Ge}_{70}$ , the first peak is located at 2.61 Å and the double peak nature is lost, replaced by a large second peak at 4.77 Å. The first nearest neighbor distance is preserved in all structures, with total and Mo-Ge partial distribution functions giving agreeing results. The

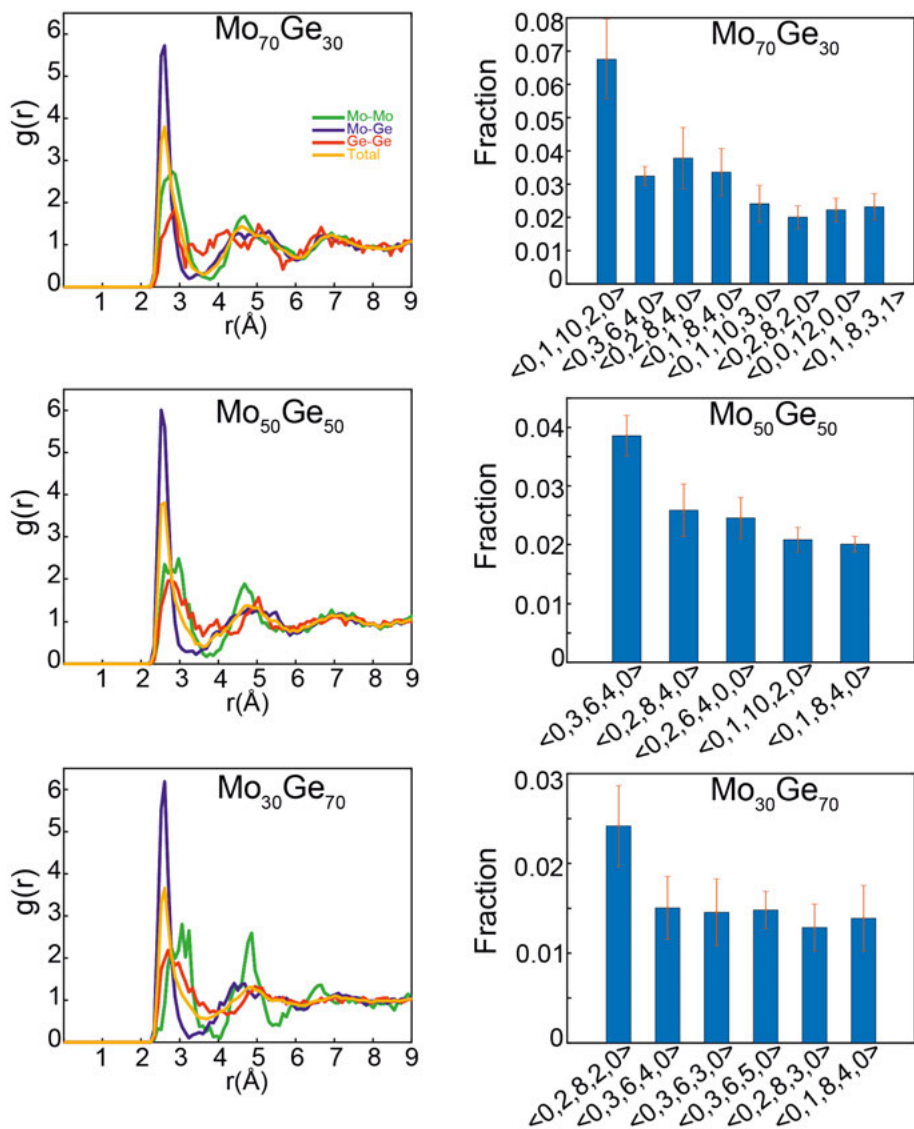


Figure 5.1. Partial RDF plots (left) and Voronoi tessellations (right) are shown for  $\text{Mo}_{70}\text{Ge}_{30}$ ,  $\text{Mo}_{50}\text{Ge}_{50}$ ,  $\text{Mo}_{30}\text{Ge}_{70}$ .

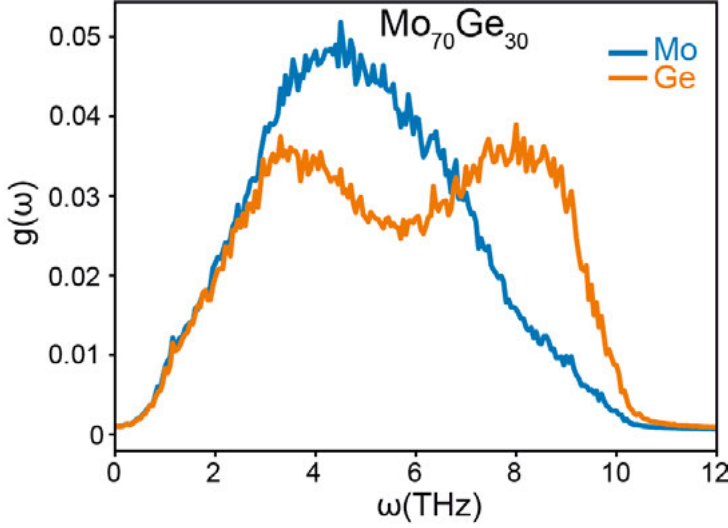


Figure 5.2. Projected vibrational density of states of  $\text{Mo}_{70}\text{Ge}_{30}$ .

smoothness and shifting of partial radial distribution functions of Mo-Mo and Ge-Ge change relative to atomic concentrations, with the second peak strongly affected by Mo concentration.

We focused on local structures with a fraction greater than 0.01. The Voronoi tessellation of  $\text{Mo}_{70}\text{Ge}_{30}$  revealed a variety of local structures, a characteristic feature of metallic glasses. The highest fraction, ( $< 0, 1, 10, 2, 0 >$ ), is known as a distorted icosahedron, while ( $< 0, 0, 12, 0, 0 >$ ) is a perfect icosahedron. These two types SROs are related to the double peak. As seen in the RDF plots, the metallic glass nature of  $\text{Mo}_{50}\text{Ge}_{50}$  decreases in connection with the local structures. However, an increase in Ge content results in a decrease in the fraction of distorted icosahedra by approximately 31 %, consistent with the distortion observed in the double peak on the total RDF plot. In contrast, the unified double peak nature of  $\text{Mo}_{30}\text{Ge}_{70}$  caused a steep decrease in SROs fraction. As Kim et al. [25] demonstrated superconductivity in amorphous  $\text{Mo}_{70}\text{Ge}_{30}$  and our produced  $\text{Mo}_{70}\text{Ge}_{30}$  exhibited similar structural properties with an abundance of perfect and distorted icosahedra, we were encouraged to use this concentration for the analysis of superconductivity.

We studied the analysis of VDOS ( $g(\omega)$ ) of  $\text{Mo}_{70}\text{Ge}_{30}$  as displayed in Fig. 5.2 for using in Eq. 5.1. The VDOS of Ge atoms has a broad frequency spectrum with two merging peaks at around 3 and 8.5 THz, while the Mo atoms' spectrum has a single broad but sharper peak at around 4 THz. The Ge atoms' spectrum was 0.4 THz broader and ended around 11 THz, while both atoms' spectra ended in almost the same frequency range between 10 - 11 THz. The accuracy could be improved by performing longer molecular dynamics simulations, which are limited to first-principles molecular dynamics.

## 5.2 Superconductivity in Amorphous $\text{Mo}_x\text{Ge}_{100-x}$

The superconducting temperature is calculated using McMillan's formula, which is proposed for one electron in the rigid-ion approximation, as shown in Eq. 5.1

$$\lambda = \sum_i \lambda_i = \sum_i \frac{\eta_i}{M_i \langle \omega_i^2 \rangle}, \quad (5.1)$$

in which  $\eta_i$ , the Hopfield parameter captures the information of electronic structure at the  $i^{\text{th}}$  atom (inside the cell),  $M_i$  is the atomic mass, and  $\langle \omega_i^2 \rangle$  is the average phonon frequency. Gaspari and Gyorffy (GG) approach can be used for calculating the Hopfield parameter:

$$\eta_i = \sum_l \frac{2(l+1)N_{i,l}(E_F)N_{i,l+1}(E_F)}{(2l+1)(2l+3)N(E_F)} |\beta_{l,l+1}|^2, \quad (5.2)$$

where  $N_{i,l}(E_F)$  represents the partial density of states at the Fermi level of the  $i^{\text{th}}$  atom ( $l$  being the azimuthal quantum number),  $N(E_F)$  is the total DOS at the Fermi level per primitive cell and  $\beta_{l,l+1}$  is the electron-phonon matrix element that contains the information about the potential and regular solutions of the radial Schrödinger equation inside each muffin-tin sphere [112]. The superconducting temperature can be evaluated using the McMillan expression, [113] by inserting the calculated value of  $\lambda$ :

$$T_c = \frac{\theta_D}{1.45} \exp \left[ -\frac{1.04(1+\lambda)}{\lambda - \mu^*(1+0.62\lambda)} \right], \quad (5.3)$$

where  $\theta_D$  represents the Debye temperature related to some average phonon frequency and  $\mu^*$  denotes the Coulomb coupling constant, which can be approximated by the commonly accepted value of  $\mu^* = 0.13$  [114]. The input parameters for Eq. 5.2 was computed using the tight-binding linear muffin-tin orbital (TB-LMTO) method within the atomic sphere approximation (ASA) [115].

As a test case, we selected one of the simplest Mo-Ge materials with superconducting properties,  $\text{Mo}_3\text{Ge}$ . Experimental results have shown that the superconducting temperature for this material is approximately  $T_c \sim 1.45$  K, and it has been observed to increase with the disorder, as reported in [116, 117].

The calculated electronic density of states of  $\text{Mo}_3\text{Ge}$ 's near  $E_F$  is found to be composed of Mo  $d$ -states hybridized with  $p$ -states and  $d$ -states from the Ge sites and localized in a valley.  $\eta$  is dominated by the Mo- $df$  and Mo- $pd$  channels, as represented in Table 5.1. To determine the site-decomposed contribution to the electron-phonon coupling, represented by  $\lambda_i$ , it is necessary to calculate the average phonon frequency, denoted as  $\langle \omega_i^2 \rangle$ . The results of this calculation are presented in Table 5.2 for the case of the empirical relationship suggested by Butler [118], which states that  $\sqrt{\langle \omega^2 \rangle} \sim 0.69\theta_D$ , in conjunction

	$S_i$	$N_{i,s}(E_F)$	$N_{i,p}(E_F)$	$N_{i,d}(E_F)$	$N_{i,f}(E_F)$	$\eta_{i-sp}$	$\eta_{i-pd}$	$\eta_{i-df}$	$\eta_i$
Mo	2.72	0.18 (0.15)	0.40 (0.37)	7.38 (7.43)	0.25 (0.24)	1.2 (0.9)	6.6 (5.9)	17.2 (17.1)	25.0 (23.9)
Ge	3.36	0.34 (0.25)	1.32 (1.27)	2.02 (1.92)	— (0.54)	0.2 (0.2)	0.3 (0.3)	— (0.8)	0.5 (1.3)

**Table 5.1.** Site-dependent electronic properties of  $\text{Mo}_3\text{Ge}$  are presented.  $S_i$  represents the Wigner-Seitz radius of each atom  $i$  considered in the calculation (in Bohr).  $N_{i,l}(E_F)$  refers to the  $l$ -th partial density of states at the Fermi level, expressed in units of  $\text{Ry}^{-1}/\text{atom}$ . In turn,  $\eta_i$  denotes the Hopfield parameter at site  $i$ , in  $\text{mRy}/\text{Bohr}^2$ . Values in parenthesis indicate the results obtained when using a *spdf*-basis for Ge.

	$M_i \langle \omega_i^2 \rangle$	$\sqrt{\langle \omega_i^2 \rangle}$	$\lambda_i$
Mo	257	5.6	0.098 (0.093)
Ge	194	5.6	0.003 (0.007)

**Table 5.2.** Site-dependent phonon and electron-phonon parameters for  $\text{Mo}_3\text{Ge}$  are presented.  $M_i \langle \omega_i^2 \rangle$  is in  $\text{mRy}/\text{Bohr}^2$ , while  $\sqrt{\langle \omega_i^2 \rangle}$  is in THz (see text). Values in parenthesis correspond to the same meaning as in Table 5.1.

with the experimentally determined value of  $\theta_D$ . According to these results, Mo plays a significant role in the superconducting properties of the  $\text{Mo}_3\text{Ge}$ , which aligns with experimental findings that  $\text{Mo}_x\text{Ge}_{100-x}$  alloys tend to exhibit an increased  $T_c$  with higher Mo content [119].

### 5.3 Conclusion of Paper III

The structural analysis of  $\text{Mo}_x\text{Ge}_{100-x}$  showed that increasing the Mo content enhances the production of both perfect and distorted icosahedra throughout the sample. The implications of these structural changes were investigated by analyzing the crystalline  $\text{Mo}_3\text{Ge}$  system as a test case. It was demonstrated that the Hopfield parameter is primarily composed of Mo-*df* and (to a lesser extent) Mo-*pd* scattering channels. This suggests that the local changes in the electronic structure of Mo sites, specifically related to *p* and *d* orbitals, are crucial for understanding the contribution of short-range order to superconductivity in amorphous  $\text{Mo}_x\text{Ge}_{100-x}$ .

## 6. Amorphous Graphene Flake

Graphene has gained a lot of attention as a material with many potential uses in electronics, magnetics, mechanics, and quantum physics since it was first isolated. Its unique two-dimensional honeycomb lattice structure is responsible for its unusual properties [120, 121, 122, 123, 124, 125, 126, 127, 128]. Despite being a crucial physical characteristic, the effect of changes on the nanomechanical traits of graphene is still mostly unknown to this day. While it is widely believed that the mechanical properties of graphene may be compromised by defects disrupting the  $sp^2$  hybridized carbon network, the reality is more nuanced. In my fourth paper, we demonstrated that the elastic modulus of graphene decreases with increasing defect density due to structural changes.

### 6.1 Defect Density Dependent Elastic modulus of Graphene

Focused Ion Beam (FIB) irradiated graphene's defect density shows a clear increasing trend as ion dosages increase. The highest level of ion dose irradiation resulted in a defect density of  $3.3 \times 10^{12} \text{ cm}^{-2}$ , which caused a significant reduction in the crystallite lattice contrast in the graphene areas. Previous Raman studies on defected graphene have shown that a sample with an  $I_D/I_G$  (intensity ratio of the D and G bands or intensity ratio of  $sp^3/sp^2$  bonds) as low as 0.7, is typically classified as amorphous graphene. AFM (Atomic Force Microscopy) based elastic modules measurements of defect density dependant elastic modules are shown in Fig. 6.1.

The plot exhibits a plateau region where the elastic modulus is relatively constant at defect density below  $10^{12} \text{ cm}^{-2}$ . However, when the defect density exceeds  $10^{12} \text{ cm}^{-2}$ , there is a significant decrease in the elastic modulus as the defect density continues to rise. The reduction in the elastic modulus can be primarily attributed to the emergence of amorphous graphene, which begins to occur when the defect density exceeds  $10^{12} \text{ cm}^{-2}$ .

### 6.2 Amorphous Graphene and Binding Energy

The binding energy and elastic modulus of graphene have been shown to have a linear correlation through theoretical calculations [130], suggesting that theoretical methods can be used to qualitatively study the mechanical properties



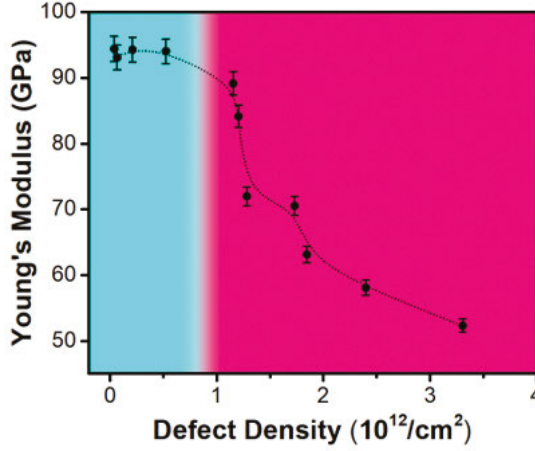


Figure 6.1. Evolution of the elastic modulus of the graphene on SiO<sub>2</sub> substrate with different defect densities. The white dotted line indicates the elastic modulus of the SiO<sub>2</sub> substrate. Reproduced from [129], with the permission of AIP Publishing.

of graphene. To further verify the impact of amorphous graphene on the elastic modulus of graphene, MD simulations were conducted on nanocrystalline and amorphous graphene of varying sizes. Graphene flakes were created by introducing a 10 Å space in the  $x - y$  directions in the supercells;  $(18 \times 18)$ ,  $(20 \times 20)$ ,  $(23 \times 23)$ ,  $(25 \times 25)$ ,  $(30 \times 30)$ ,  $(35 \times 35)$ ,  $(40 \times 40)$ ,  $(45 \times 45)$ ,  $(50 \times 50)$  where we set lattice parameter of the unit cell as 2.46 Å and we set the vacuum region at 40 Å by using CMD with Tersoff potential. Amorphous graphene structures were then generated by randomly distributing atoms within the defined 2D crystalline graphene supercells and the defined glass production steps (in theoretical background section) were performed. The amorphous graphene flakes were created by adding a 10 Å space in the  $x - y$  plane to the periodic 2D amorphous structures. The nanocrystalline graphene and amorphous graphene flakes were then subjected to force minimization at  $T = 0$  K, with an energy tolerance of  $1 \times 10^{-8}$  eV for stopping. In Fig. 6.2 the produced stable  $(20 \times 20)$  and  $(50 \times 50)$  amorphous and nanocrystalline sheets are shown, which correspond respectively to 4.94 and 12.34 nm in size. The binding energies of the systems were calculated using the below formula,

$$BE = - \left[ \frac{E_{system} - nE_C}{n} \right], \quad (6.1)$$

where  $E_{system}$  represents the total energy of the system,  $E_C$  is the energy of an individual carbon atom, and  $n$  is the total number of atoms in the system.

Fig. 6.3 displays the binding energy plots, which reveal that amorphous graphene has a significantly lower binding energy compared to nanocrystalline graphene. This supports our argument that amorphousness negatively impacts the mechanical properties of graphene.

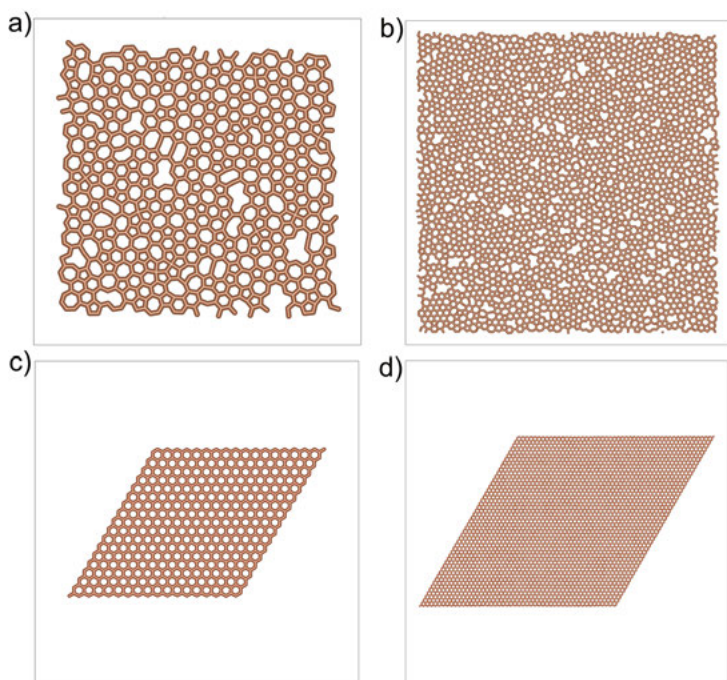


Figure 6.2. Amorphous (a, b) and nanocrystalline graphene (c, d) sheets are shown, where (a and c) are 4.94 nm in size and (b and d) are 12.34 nm in size.

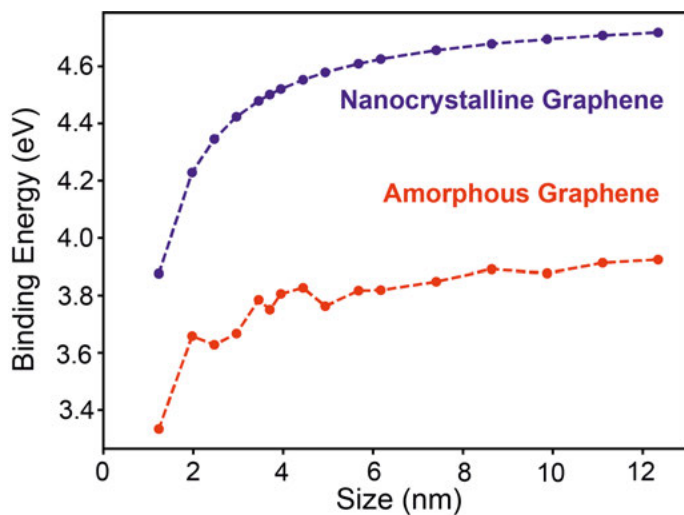


Figure 6.3. The variation of binding energy is displayed in relation to the size of both amorphous and nanocrystalline graphene sheets.

### 6.3 Conclusion of Paper IV

The variation of elastic modulus variation relative to the defect density of the graphene sheet was studied experimentally. It was found that the elastic modulus of graphene remains relatively unchanged when the defect density is below  $10^{12} \text{ cm}^{-2}$ . However, when the defect density exceeds  $10^{12} \text{ cm}^{-2}$ , the elastic modulus begins to decrease significantly and the structure becomes amorphous. Our CMD simulations support the idea that the structural changes in the system lead to a decrease in the elastic modulus, as explained by the calculated binding energies.

## 7. Systematic Atomistic Study of Amorphous 2D- Graphene, Silicene and Silicon Carbide

Low-dimensional materials have gained prominence in the electronics industry since the discovery of graphene in 2004, through the functionalization of 2D materials or the creation of combinations of these structures [131, 132, 133]. On the other hand a variety of stable, inorganic amorphous 2D materials with an atomic layer thickness, including amorphous-C; amorphous-BP, amorphous-TMD, amorphous-BN, amorphous-MoS<sub>2</sub>, etc., have been successfully synthesized using techniques such as exfoliation, electron irradiation, chemical vapor deposition (CVD), and physical vapor deposition (PVD) [27, 28, 29, 30, 31, 32, 33, 34, 35, 36]. However, the structures and properties of these materials are not as well understood as those of 2D-crystalline materials. In my fifth paper, we performed a systematic analysis of amorphous 2D-graphene (A-Gra); silicene (A-Si), and silicon carbide (A-SiC). These structures' electronic, optical, and low thermal conductivity properties may make them promising candidates for use in future thermoelectric and thermal coatings, electronics, optoelectronics, and a variety of other application areas.

### 7.1 Structural Properties

2D A-Gra, A-Si, and A-SiC structures were respectively created in two supercell sizes: one with 200 atoms in a 10×10 arrangement and another with 5000 atoms in a 50×50 arrangement with CMD. The lattice parameters for the unit cell of these structures were chosen to be 2.46 Å, 3.87 Å, and 3.10 Å respectively. A vacuum region of 40 Å was also included. The recipe for glass production was implemented in the 2D ( $x - y$ ) plane, with atomic movements constrained along the  $z$ -direction. Following force minimization, the number densities of the A-Gra, A-Si, and A-SiC structures were calculated to be  $3.32 \times 10^{15} \text{ cm}^{-2}$ ,  $1.38 \times 10^{15} \text{ cm}^{-2}$  and  $2.18 \times 10^{15} \text{ cm}^{-2}$ , respectively. A comparison of the produced structures in the 10×10 and 50×50 supercells showed good agreement with each other and with the literature [37, 38, 40, 41, 42, 28, 43, 47, 48, 46], in terms of radial, angular distributions and ring statistics. The 10×10 structures were deemed suitable for DFT calculations to analyze the electronic and optical properties of 2D A-Gra, A-Si, and A-SiC. The structural relaxation of the structures at 0 K is depicted in Fig. 7.1, which also shows the variations in bond lengths, angles, and rings. Side views of the

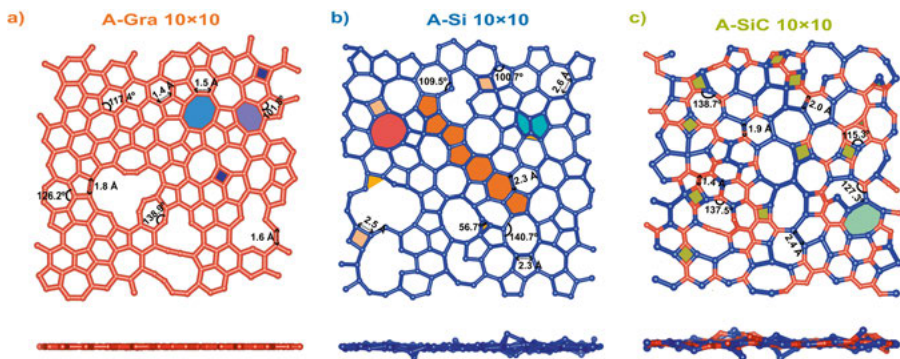


*Figure 7.1.* The side and top views of the small ( $10 \times 10$ ) systems, a) A-Gra, b) A-Si, and c) A-SiC, are shown along with their varying bond lengths and angles at 0 K. Selected rings specific to each system are also depicted with different color fills. For A-Gra, the smallest 4-fold rings and larger 7-fold and 8-fold rings are indicated. For A-Si, rings of varying sizes from 3-fold to 8-fold are marked, and a “chain defect” is shown in orange. For A-SiC, examples of existing 3-fold to 7-fold rings are shown in shades of green.

structures reveal similarities between crystalline and amorphous graphene and silicene in terms of planarity and buckling at 0 K, while appearing wavy at 300 K. In contrast, A-SiC retains its buckled nature at both temperatures.

## 7.2 Electronic Properties

All the studied structures were found to have metallic properties. Previous research has confirmed the metallic nature of A-Gra’s electronic structure [40, 28]. While A-Si was previously assumed to be a semiconductor [43], our findings indicate that it is actually metallic. This is the first time A-SiC’s electronic nature has been reported as in Fig. 7.2.

The charge distribution around the Fermi level varies with ring size, from small to large. In A-Gra, hexagonal rings have equal charge distribution, while pentagons near large rings and large rings with dangling bonds have higher charge density. Some atoms bound in large rings also show high, equally shared charge density. The charge density of A-Gra and A-Si around the Fermi energy is due solely to contributions from  $p_z$  orbitals, as in their crystalline semimetallic phases. A-SiC’s charge distribution around the Fermi level has  $p_y$  and  $p_z$  orbitals contributions, while crystalline SiC has a 2.55 eV gap [134]. Unlike A-Gra, A-Si has a high charge density for all ring types. Si atoms on the edge of large rings with dangling bonds have a larger charge, which is also greater than the charge densities of A-Gra’s large rings’ dangling bonds. In A-SiC, the charge densities of Si and C atoms vary due to differences in hy-

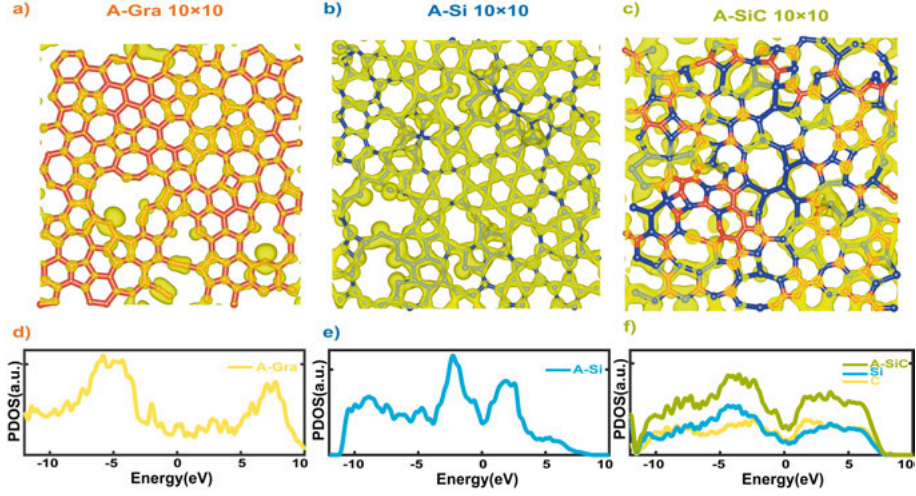


Figure 7.2. The small systems' partial charge distributions at the Fermi level at 0 K are depicted for a) A-Gra; b) A-Si; and c) A-SiC. The electronic density of states for these systems is shown in figures d) to f) in the same order. The atom-projected density of states for A-SiC is also displayed in f).

bridization depending on neighboring atoms. In isolated rings, C or Si atoms in A-Gra or A-Si can have comparable charge distributions.





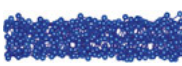
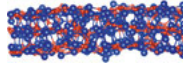
### 7.3 Layered 2D Amorphous Structures: Bilayer, Trilayer

We studied bilayer and trilayer amorphous structures by including van der Waals interactions [94, 95] and using 20 Å vacuum distance with DFT. We tested two stacking styles: one with all layers oriented in the same direction, and another with the second layer rotated 90 degrees relative to the first layer for bilayer systems. For trilayer systems, only the second layer was rotated 90 ° relative to the first and third layers. The examined scenarios for all structures were demonstrated in Table 7.1. The calculation of the interlayer binding energy per atom ( $BE_{interlayer}$ ) was performed utilizing Eq. 7.1:

$$BE_{inter-layer} = \frac{(N_{layer} \times E_{SL}) - E_{ML}}{N_{atom} \times N_{layer}}, \quad (7.1)$$

where  $E_{SL}$  represents the energy of the single-layer, while  $E_{ML}$  denotes the energy of the bi- or tri-layers. The number of layers in the multilayer structure is indicated by  $N_{layer}$ , and  $N_{atom}$  refers to the number of atoms per layer [135].

The layer binding energy per atom, as calculated for A-Gra, in Table 3.3, is consistent with the values reported for crystalline van der Waals-bonded bilayer graphene in previous studies [135, 136]. A-Si tends to form covalent

			A-Gra	A-Si	A-SiC
BE <sub>interlayer</sub> (meV)	Bilayer	Identical	21.13	378.35 	174.68 
		Rotated	21.75 	353.83	172.18
	Trilayer		20.04 	459.31 	234.38 

**Table 7.1.** Calculated interlayer binding energies between A-Gra, A-Si, and A-SiC layers in the multi-layered systems. Bilayer structures were classified into two groups; identical, referring to the case that the same layer being top of each other, and rotated, referring to the case of the second layer being rotated by 90 °. The energetically more favorable structures' side view was appended below the calculated energies of that specific bilayer system. Trilayer structures were modeled by keeping the up and bottom layers the same and only rotating the mid layers by 90 ° cases.

bonds between its layers, resulting in an increase in binding energy per layer. Interestingly, our observations indicate that in A-SiC, the Si atoms form covalent bonds with Si atoms in the adjacent layer, while the C atoms maintain van der Waals bonding with C atoms in the adjacent layer. The metallic nature of all the structures (bilayer and trilayer) is preserved.

## 7.4 Optical Properties

Initially, our attention was directed towards the absorption spectrum, represented by the imaginary component of dielectric functions as shown in Fig. 7.3 (a, d, g), in the absence of LFE. Our findings revealed that the optical properties of A-Gra, A-Si, and A-SiC were similar to their crystalline equivalents. With the exception of A-Si's parallelly polarized components, all calculated spectra for the three structures exhibited a red-shift relative to their crystalline equivalents. We discovered that all three structures absorbed light from the IR to UV range and had plasmon frequencies in the UV range. The plasmon peak of A-Si is sharp and 6 times higher than the second plasmon peak of crystalline silicene. The rising static refractive index of A-Gra, A-Si, and A-SiC indicates that their absorption range and capacity exceed those of their crystalline equivalents, making them more suitable for use in optoelectronic devices.



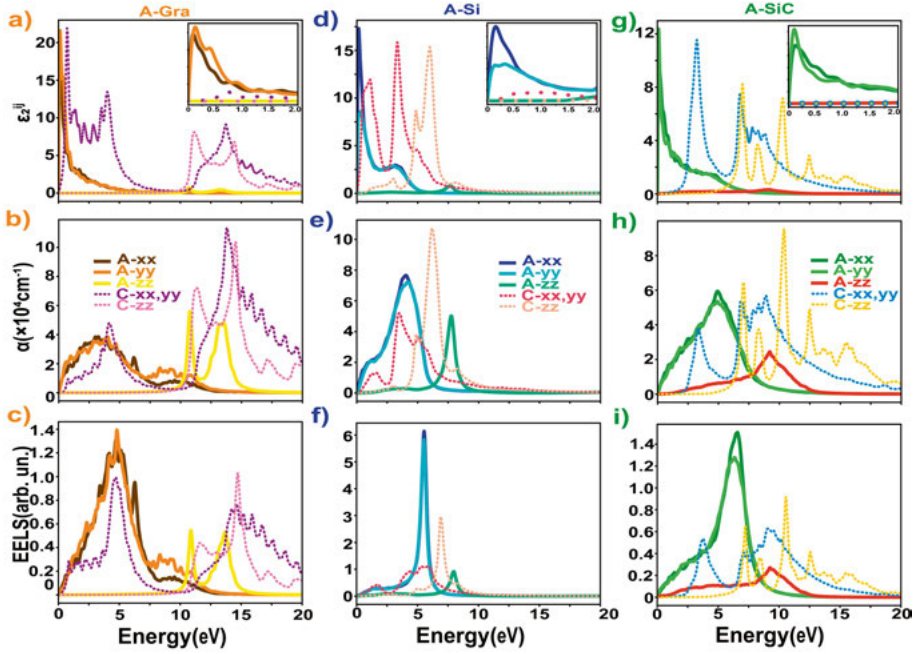


Figure 7.3. The optical properties of amorphous graphene (A-Gra), amorphous silicon (A-Si), and amorphous silicon carbide (A-SiC) are compared with their crystalline counterparts. The first row of figures (a, d, g) displays the calculated imaginary part of the dielectric functions for both perpendicular (in-plane: A-xx; A-yy; C-xx,yy) and parallel (out of plane: A-zz; C; ZZ) light polarizations, with IPA and without the inclusion of local field effects. To facilitate comparison the crystalline counterparts (C-xx,yy; C-zz) are multiplied by a factor of 8, 6, or 6, respectively. The insets show the spectrum from 0 - 2 eV without multiplication. The second row (b, e, h) shows the absorption coefficients, while the third row (c, f, i) displays the electron energy loss spectra of the systems.



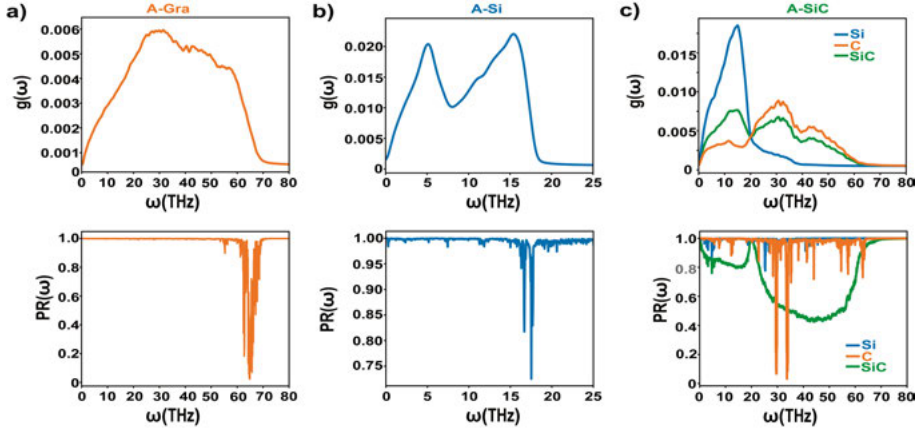


Figure 7.4. The top row displays the VDOS plots for the systems, while the bottom row shows the PR plots. The systems are represented as follows: a) A-Gra, b) A-Si, and c) A-SiC, along with their total and atom-projected VDOS and PR.

## 7.5 Thermal Conductivity and Vibrational Properties

We utilized  $(50 \times 50)$  big cells for thermal conductivity with CMD. Prior research has demonstrated that thermal conductivity is influenced by the degree of amorphicity in the structure [37, 38]. Antidormi et al [37]. found that the rate of quenching during production is inversely proportional to thermal conductivity. In our study, we selected a fixed quenching rate and calculated the thermal conductivity of A-Gra, A-Si, and A-SiC. Our results showed that thermal conductivity values of  $55.30 \pm 11.01$  W/Km for A-Gra,  $2.68 \pm 0.59$  W/Km for A-Si, and  $70.29 \pm 12.03$  W/Km for A-SiC. The calculated value for A-Gra is consistent with the range reported in previous studies and differs significantly from the thermal conductivity of pristine graphene, which falls within the range of 2600 – 3050 W/Km [37]. A-Si's thermal conductivity was calculated as similar to the thermal conductivity of bulk amorphous Silicon reported in the literature [44, 45]. Zhou et al. also reported a value of  $2.4 \pm 0.25$  W/Km for amorphous Si-Nanowire [44], which decreases with dimension compared to their calculated value for amorphous bulk Si. Despite differences in structural quality between their reference work and our study, our calculated value is in good agreement with the literature. Compared to A-Gra and A-Si, we found that A-SiC had a higher thermal conductivity, which is acceptable given the calculated statistical error range for A-Gra and A-SiC.

We analyzed the low thermal conductivity of  $(50 \times 50)$  big cells A-Gra, A-Si, and A-SiC by examining their vibrational density of states (VDOS) and mode participation ratios (PR). It is well known that the VDOS of amorphous structures exhibits broader merged peaks compared to their crystalline counterparts. Our work, as shown in Fig. 7.4, demonstrates that the vibrational properties of amorphous structures follow similar trends to 3D-bulk cases as dimensions

decrease. The density can alter these similarities by increasing or decreasing mode intensity and shifting mode frequency relative to the new webbing and hybridization of the constituent atoms. Our calculated VDOS for A-Gra shows broadening similar to both its crystalline counterparts and literature data at different densities and structural quality. While we cannot quantify extendon (propagons, diffusion) and locon modes due to the Green-Kubo method's equipartitioning of all modes, extendon modes are the primary heat carriers. The cases we studied are neither at low nor high density. In structurally denser systems, we expect to see an increase in  $sp^3$  hybridization states. As a result, our A-Gra system exhibits a thermal conductivity of approximately 55.30 W/Km, which is reflected in the VDOS and PR as an increase in extendon modes. Without performing an Allen-Fellman modal analysis, it is difficult to distinguish between the transition frequencies of propagon, diffusion, and locon modes. Although our calculated PR for A-Gra shows a phonon-like contribution ( $PR = 1$ ) until the sharp decrease of locon modes ( $PR = 0.2$ ), this is due to the inclusion of all modes' contributions in equilibrium MD-based calculations. Furthermore, the regime between 10 THz and 50 THz is dominated by diffusions, indicating that they are significant heat carriers in the system, along with propagons. Nonetheless, the increase in extendons is sufficient to account for the thermal conductivity of A-Gra, as compared to the lower thermal conductivities reported in previous studies [38, 37, 137]. The VDOS of our A-Si system is consistent with the literature VDOS of bulk amorphous silicon at a similar density. In denser systems, the intensity of the first peak can decrease while the intensity of the second peak increases, resulting in a blueshift in the tail observed as locon frequencies. However, our PR differs from the literature in that our system does not exhibit a locon peak as defined for bulk cases. We hypothesize that this may be due to a decrease in dimension. Interestingly, our system exhibits low thermal conductivity despite the absence of locon modes, which is consistent with reference [45], where propagons were found to be the dominant heat carriers in amorphous silicene. The calculated VDOS of our A-SiC system exhibits characteristics of both A-Gra and A-Si, despite the differences in bonding nature and density between C and Si atoms. These differences are evident as sharp redshifts in the locon modes ( $\sim 30$  THz) of C atoms in the partial VDOS shown in Fig. 7.4. A similar redshift is also observed in the diffusion modes of Si atoms (beyond  $\sim 20$  THz). The overall VDOS is in reasonable agreement with Li et al.'s amorphous bulk SiC VDOS plot at a similar density. In the atom-projected VDOS plots, Si atoms contribute to the overall A-SiC VDOS as unified and red-shifted extendon modes, while C atoms' contributions are seen as an increase in the intensity of the second peak. However, redshifts in the frequency ranges of both Si and C atoms' modes are present in both plots. In the A-SiC webbing, C atoms' diffusion modes visibly increase to a wide range of  $\sim 63$  THz, while the frequency range of locon modes narrows and shifts forward to  $\sim 30$  THz, as seen in the PR plot. Although C atoms exhibit locon modes in the projected VDOS, over-

all A-SiC does not show localized modes but instead exhibits a wider range of diffusion modes.

## 7.6 Conclusion of Paper V

In conclusion, we conducted a detailed atomistic simulation study of 2D A-Gra, A-Si, and A-SiC. Our simulated amorphous structures are in reasonable agreement with the literature. All three structures exhibit unique bond lengths, angles, and ring sizes. We also analyzed their electronic properties and found them to be metallic with different charge distributions on local rings. Their optical properties are comparable to their crystalline counterparts, with redshifts observed in all calculated spectra except for A-Si's parallelly polarized components. We calculated thermal conductivity using the Green-Kubo method and found that extendons are the primary carriers of thermal transport in all three systems. A-SiC's carbon atoms show localized modes in the atom-projected DOS and PR, while this is not observed in the overall A-SiC. The dominance of extendons is thought to explain the relatively high thermal conductivity of A-Gra and A-SiC. These 2D amorphous structures with specific and tunable electronic and thermal properties can serve as alternative materials for future functional device designs.



Part III:  
Final Summaries & Remarks



## 8. Conclusion and Outlook

In this thesis, I discussed amorphous metallic glasses and 2D amorphous glasses' structural dependent properties by employing classical molecular dynamics simulations and density functional theory-based calculations.

I first focused on the  $\text{Fe}_{0.85}\text{Zr}_{0.15}$  metallic glass' lattice thermal conductivity tuning by nanostructured voids. The effects of local structural orderings, temperature, and pressure on these structures are investigated in detail. The results revealed that the voids and pressure can be used as efficient methods for tuning the lattice thermal conductivity of metallic glasses. The proposed glass model offers a convenient approach for designing case-specific materials, particularly for use in highly efficient thermoelectric modules, where the Zr-based MG's are employed as junction materials. In the second paper, I investigated experimentally observed structural disorder-sourced magnetic properties of CoZr MG's. The simulation results, in which the saturation magnetic moments of MG were calculated for Co concentrations in the range of ( $40 \leq x \leq 70$  at.%), showed a linearly increasing trend and a good agreement with experimental data was observed. Further theoretical simulations can shed light on the local magnetic interactions due to the short-to-medium range local orderings in a casual manner. In our third paper, I exhibited the compositional-structural relationship and superconductivity in MoGe metallic glass. Electron-phonon coupling parameters were calculated and the orbital channels responsible for the dominating contribution were identified.

Papers four and five include investigations of the structure-dependent properties of 2D amorphous structures. In paper four, the experimentally observed increase in defect density due to ion radiation on graphene, and the decrease in elastic modulus, are explained using different-sized amorphous graphene sheets and their binding energies. The findings offer crucial insights into the rational design of graphene-based nanodevices, particularly in terms of their mechanical properties. In paper five, I investigated the structural, thermal, electronic, and optical properties of 2D amorphous graphene, silicene, and silicon carbide structures. The analysis revealed that they are thermally low conductors, showing the metallic electronic density of states and unique charge distributions on their special ring structures. Their broad optical absorption spectrum is the first insight into the 2D amorphous structures' optical properties. Through our systematical analysis, we can conclude that with their unique and adjustable electronic and thermal properties, 2D amorphous structures present a promising porous alternative for the design of future electronic, optoelectronic, and on-demand devices such as gas sensors.

## Outlook

The discovery of hidden structural order and related properties in disordered structures has made amorphous materials as valuable as crystalline materials for the development of new functional materials. Metallic glasses, particularly those based on Zr, are a valuable member of the glass family due to their low cost, mass production capabilities, and low lattice thermal conductivity. We proposed a model for analyzing the decrease in lattice thermal conductivity in the presence of nanostructured voids in FeZr metallic glass. This route can be helpful in successfully overcoming heat-dependent efficiency loss in devices, making it easier to sensitize porous materials or tailor functional coatings. Further investigation into other Zr-based metallic glass compositions can reinforce the validity of the formula. In our model, we only used spherical voids to tune the lattice thermal conductivity. However, we were unable to obtain a shape-dependent decrease in these systems. Therefore, further investigation into symmetrical and asymmetrical shaped voids and relatively larger voids is needed. This will help to have a better formulation for predicting the void-dependent decrease in lattice thermal conductivity. Investigating the contribution of local structures in these systems is also essential to gain a deeper understanding of the amorphous nature of solids. Similarly, revealing the role of SRO to MRO local orderings in magnetic properties is a future aim, as demonstrated by Thórarinsdóttir et al who obtained proximity effect in magnetic nanolaminates [138]. Xi et al. showed that 2D hydrogenated germanene can show superconductivity [139]. After studying 3D-MoGe superconductivity, we can use our methodology to investigate the superconductivity of 2D amorphous germanene. This field has much room for discovery and modeling. Finally, 2D amorphous and layered structures should be studied and discovered in a broader context by including optical and electronic properties due to their open bonds and structure-dependent hybridization characteristics and properties. The transition from 3D to 2D presents an abundance of hidden properties in amorphous structures, and while this thesis has addressed the thermal, magnetic, superconductivity, and optical properties of selected amorphous structures, there is still much to explore and utilize in the pursuit of new materials research. This field holds tremendous potential for uncovering novel properties and developing cutting-edge materials with exceptional electronic, thermal, and mechanical properties, thereby propelling the advancement of materials science and technology.



## 9. Popular science summary

Glass is a versatile and durable material with a wide range of applications, from eyewear to cups and art crafts. Throughout human history, glass has been used for various purposes, including cutting and crafting. Silica-based glasses are particularly abundant and affordable, making them suitable for use in fiber optics and various industries. Furthermore, glass is not only found on Earth but also on the Moon and exoplanets such as “*HD 189733b*”. Namely, nature and humanity love glass and its products. However, our understanding of “*glass*” or “*amorphous systems*” or “*frozen liquids*” remains limited due to their complex structural nature, characterized by short-to-medium range local orderings without long-range ordering. Zachariassen’s definition of glass, along with both theoretical and experimental findings about its amorphous nature, has advanced our knowledge. However, our understanding of amorphous structure and its properties is still limited and needs to be discovered. One of the simplest ways of understanding the amorphous structure is through atomistic simulations using Newton’s equations of motion, which is known as molecular dynamics. The time evolution of a system can be used to understand its structure and structure-dependent properties. However, producing glassy systems is a challenge with time that limits our understanding. One realistic way of simulating glass is the melt-quench method that we can perform by employing thermostats on the system. Following production, the properties can be investigated based on the atomistic trajectories for some properties, i.e., thermal conductivity and vibrational. However, the classical approach is not enough for some properties, i.e., electronic and optical due to obligatory quantum corrections, especially for low temperatures. Therefore, we used a deeper approach level of electrons. Both approaches have their own advantages and disadvantages. In the classical approach, we have an inter-atomic potential problem that acts on atoms to follow their trajectories. The potentials used are mostly empirical or semi-empirical based on experimental results and are mostly limited. Whereas an approach that includes quantum corrections requires a limited system size of hundreds of atoms. This is also far from a realistic material size. At this point, a benchmark calculation enables the transfer between two methods, allowing for efficient usage and broader property analysis of amorphous systems. In this thesis, I first focused on benchmark calculations for glass production. After obtaining an agreeing receipt, property analysis was done by using the strengths of both approaches. We studied both 3D and lower-dimensional (2D) amorphous structures. Especially we focused on metallic glasses (MG). MG are thermally low conductors and are used in

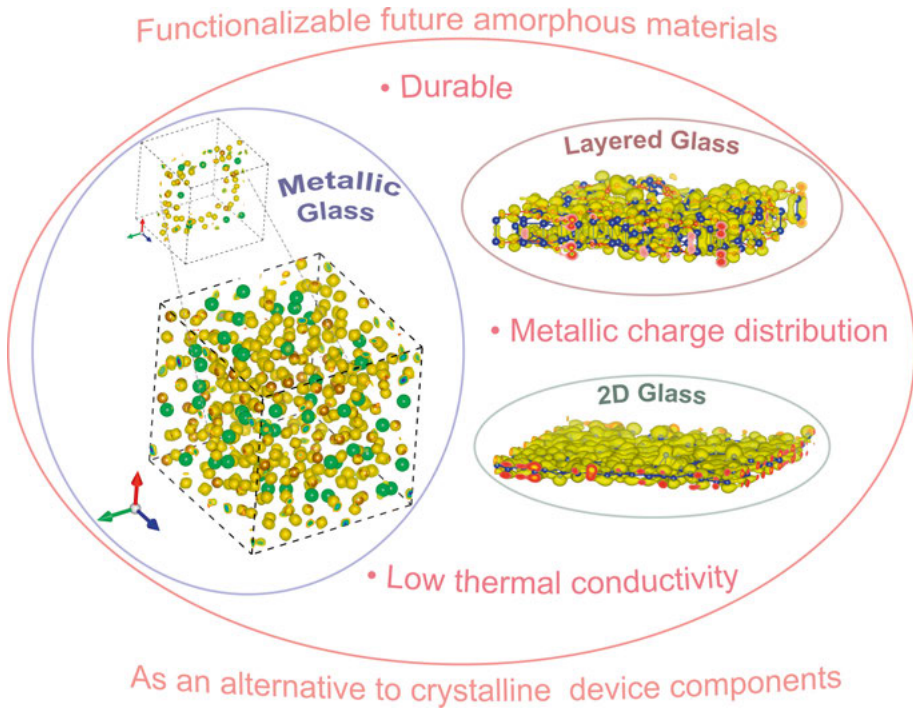


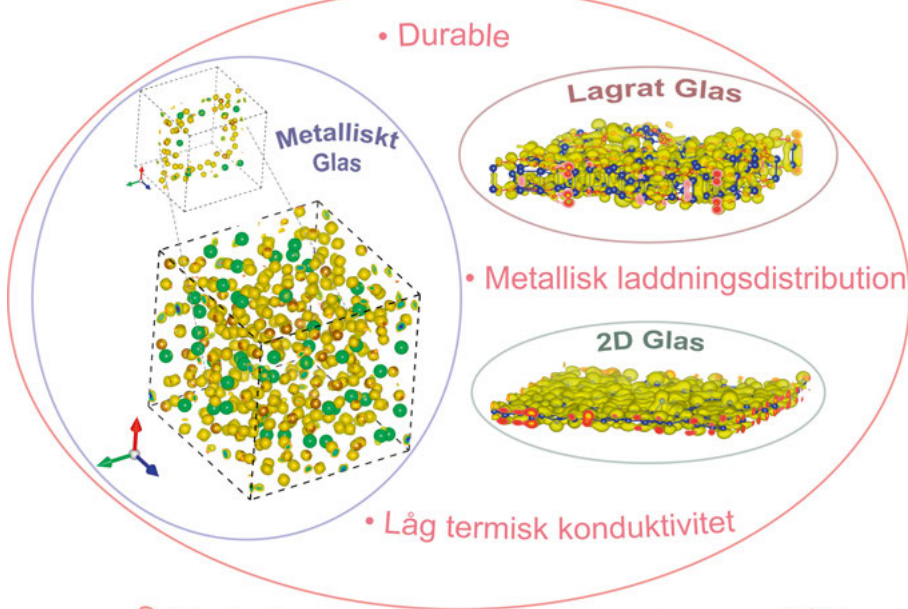
*Figure 9.1.* Amorphous structures (glasses) are a future alternative to their crystalline counterparts, with their functionalizability from three-dimensional (i.e., metallic glasses (MG)) to low-dimensional structures (i.e., layered structures and two-dimensional (2D) structures). Amorphous structures are known for their durability and low thermal conductivity. The examples shown are also metallic but thermally low conductors, which is more advantageous than crystalline metals that suffer from heat in device applications.

thermoelectric modules. Heat is one of the biggest problems in all electronic devices limiting the device's efficiency, durability, and life. Therefore, MG are in focus in industries to develop new materials and/or functionalization of materials for increasing the device efficiency, durability, and also life. In the first paper, we focused on tuning the thermal conductivity of  $\text{Fe}_{0.85}\text{Zr}_{0.15}$  MG by nanostructures and pressure. In this study, it's shown that their lattice thermal conductivities can be tuned by employing the suggested void size-dependent glass thermal conductivity obtaining model. We also focused on the effect of local structures on the global properties of the studied glass structure. In the second paper, we focused on experimentally obtained saturation magnetization of CoZr MG, which is affected by the structural composition of Co atoms. The theoretically and experimentally obtained results show that structures determine the magnetic properties, and this may include a short-to-medium-range ordering effect. Similarly, in the third paper, structural-dependent superconductivity is obtained in MoGe MG. In addition to MG, in the fourth and fifth papers, we show the dimensionality effect on properties. In the fourth paper, graphene's elastic modulus decrease is explained as a structural change from an ordered to a disordered phase by causing a binding energy decrease. In the fifth paper, both 2D and layered graphene, silicene, and silicon carbide's structural, thermal, vibrational, electronic, and optical properties are discussed in detail. These structures are found to have metallic electronic properties and uneven charge distribution, which can increase their functionalizability for specific applications such as gas sensing. Together with their low thermal conductivity, they can be used as alternative materials to their crystalline counterparts in future electronic, optoelectronic, and many other areas. Last, but not least, there is still much to discover and learn about amorphous materials' structurally dependent properties and their potential applications in functional devices.

## 10. Populärvetenskaplig sammanfattning

Glas är ett mångsidigt och hållbart material med en mängd olika användningssområden, från glasögon till koppar och konsthantverk. Genom hela mänsklighetens historia har glas använts för olika ändamål, till exempel skärning och hantverk. Silikabaserade glas är särskilt vanliga och prisvärda, vilket gör dem lämpliga för användning inom fiberoptik och olika industrier. Dessutom finns glas inte bara på jorden utan också på månen och exoplaneter som "*HD 189733b*". Det verkar som älskar naturen och mänskligheten glas och dess produkter. Men vår förståelse av "*glas*" eller "*amorfa system*" eller "*frusna vätskor*" är fortfarande begränsad på grund av deras komplexa strukturella natur, som kännetecknas av kort-till-medellånga lokala ordningar utan långdistansordning. Zachariasens definition av glas, tillsammans med både teoretiska och experimentella resultat om dess amorfa natur, har utvecklat vår kunskap. Men vår förståelse av amorfa strukturer och dess egenskaper är fortfarande begränsad och behöver expanderas. Ett av de enklaste sätten att förstå den amorfa strukturen är genom atomistiska simuleringar med Newtons rörelseekvationer, vilket går under beteckningen molekylodynamik. Tidsutvecklingen av ett system kan användas för att förstå dess struktur och strukturberoende egenskaper. Men att producera glasartade system är en utmaning, där tidsåtgången utgår en begränsande faktor för vår förståelse. Ett realistiskt sätt att simulera glas är smält-kylmetoden som vi kan utföra genom att använda termostater på systemet. Efter produktionen kan egenskaperna undersökas baserat på de atomistiska banorna för vissa egenskaper, dvs. värmeledningsförmåga och vibrationer. Men den klassiska metoden räcker inte för vissa egenskaper, dvs. elektroniska och optiska på grund av obligatoriska kvantkorrigeringar, särskilt vid låga temperaturer. Därför använde vi en djupare metod på elektronnivå. Båda metoderna har sina egna fördelar och nackdelar. I den klassiska metoden beskriver vi atomerna och deras banor med hjälp av parpotentialer. De potentialer som används är mestadels empiriska eller semi-empiriska baserade på experimentella resultat och är mestadels begränsade. Medan en metod som inkluderar kvantkorrigeringar kräver att vi begränsar systemets storlek till något hundratals atomer. Detta är också långt ifrån en realistisk vilket är långt ifrån en realistisk beskrivning av materialen. Idag har vi nått en punkt där vi kan göra benchmarkberäkningar mellan de två metoderna, vilket möjliggör effektiv användning och bredare analys av egenskaper hos amorfa system. I denna avhandling fokuserade jag först på benchmarkberäkningar för glasproduktion. Efter att ha fått ett recept på överensstämmelse mellan metoderna, gjordes egenskapsanalysen med hjälp av styrkorna hos båda metoderna. Vi

## Funktionaliserbara framtida amorfa material



## Som ett alternativ till kristallina enhetskomponenter

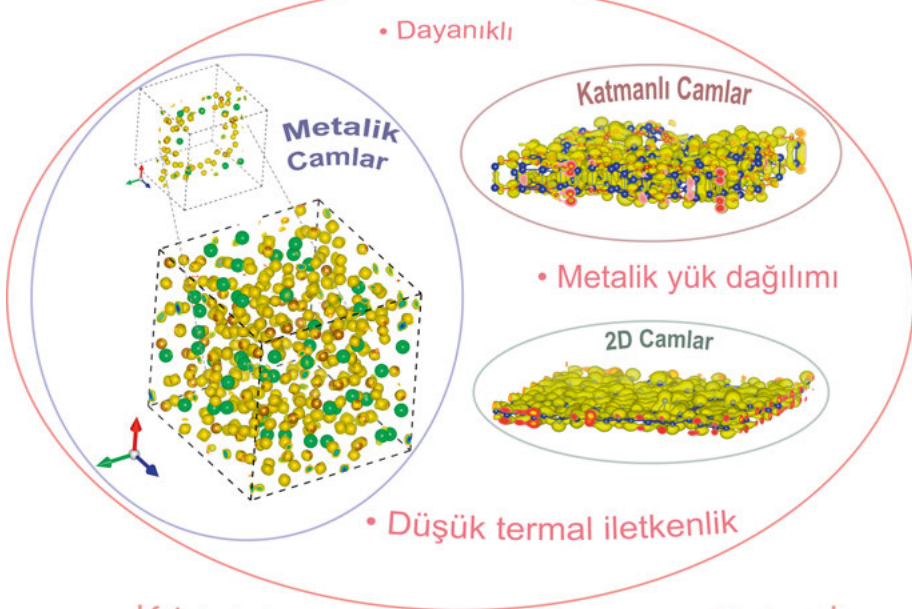
Figure 10.1. Amorfa strukturer (glas) är ett framtida alternativ till deras kristallina motsvarigheter, med deras funktionalitet från tredimensionella (t.ex. metalliska glas (MG)) till lågdimensionella strukturer (t.ex. skiktade strukturer och tvådimensionella (2D) strukturer). Amorfa strukturer är kända för sin hållbarhet och låga värmeledningsförmåga. De exempel som visas är också metalliska, men har låg termisk ledningsförmåga, vilket är fördelaktigt i jämförelse med kristallina metaller där värme leder till prestandaförluster i tillämpningar.

studerade både 3D och lägre dimensionella (2D) amorfa strukturer. Särskilt fokuserade vi på metalliska glas (MG). MG är termiskt låga ledare och används i termoelektriska moduler. Värme är ett av de största problemen i all elektronik, och begränsar effektivitet, hållbarhet och livslängd. Därför finns ett industriellt fokus på MG för utvecklingen av nya material och/eller funktionalisering av material för att förbättra komponenters effektivitet, hållbarhet och livslängd. I den första artikeln fokuserade vi på att justera termisk ledningsförmåga hos  $\text{Fe}_{0.85}\text{Zr}_{0.15}$  MG genom nanostrukturer och tryck. I denna studie visar vi att gittrets bidrag till den termiska ledningsvärmeförmågan kan justeras genom att använda den föreslagna glasmodellen för termisk ledningsförmåga beroende på tomrummets storlek. Vi fokuserade också på effekten av lokala strukturer på globala egenskaper hos den studerade glasstrukturen. I den andra artikeln fokuserade vi på experimentellt erhållna mättnadsmagnetiseringen för CoZr MG, som påverkas av Co-atomernas strukturella position. De teoretiskt och experimentellt erhållna resultaten visar att strukturen bestämmer magnetiska egenskaper, och detta kan inkludera effekter på kort-till-medellång räckvidd. På liknande sätt erhöles i den tredje artikeln strukturberoende supraledning i MoGe MG. Förutom MG visar vi i den fjärde och femte artikeln dimensionseffekten på egenskaper. I den fjärde artikeln förklaras minskningen av grafens elasticitetsmodul som en strukturell förändring från ordning till en ordnad fas genom att orsaka en minskning av bindningsenergin. I den femte artikeln diskuteras både 2D och lagergrafens, silicen och kiselkarbidens strukturella, termiska, vibrerande, elektroniska och optiska egenskaper i detalj. Dessa strukturer har metalliska elektroniska egenskaper och ojämn laddningsfördelning, vilket kan öka deras funktionalitet för specifika tillämpningar som gassensorer. Tillsammans med deras låga värmeledningsförmåga kan de användas som alternativa material till deras kristallina motsvarigheter inom framtida elektronik, optoelektronik och många andra områden. Sist men inte minst finns det fortfarande mycket att upptäcka och lära sig om amorfa materials strukturberoende egenskaper och deras potentiella tillämpningar i funktionella enheter.

## 11. Populer Bilim Özeti

Camsı yapılar çok yönlü ve dayanıklı bir malzemedir ve gözlükten bardaklara ve sanat eserlerine kadar geniş bir uygulama yelpazesine sahiptir. İnsanlık tarihi boyunca cam, kesme ve el işçiliği gibi çeşitli amaçlarla kullanılmıştır. Silika bazlı camlar özellikle bol ve uygun fiyatlıdır, bu da onları fiber optik ve çeşitli endüstrilerde kullanım için uygun hale getirir. Ayrıca, cam sadece Dünya’da değil, aynı zamanda Ay ve “*HD 189733b*” gibi egzoplanetlerde de bulunur. Yani doğa ve insanlık camı ve ürünlerini sever. Ancak, “*cam*” veya “*amorfsistemler*” veya “*dondurulmuş sıvılar*” hakkındaki anlayışımız, uzun menzilli yapısal düzen olmadan kısa-orta menzilli yerel düzenle karakterize edilen karmaşık yapısal doğaları nedeniyle sınırlıdır. Zachariasen’in cam tanımı, amorf doğası hakkındaki teorik ve deneysel bulgularla birlikte bilgimizi ilerletmiştir. Ancak, amorf yapı ve özellikleri hakkındaki anlayışımız hala sınırlıdır ve keşfedilmeye ihtiyaç duymaktadır. Amorf yapının en basit yollarından biri, Newton hareket denklemlerini kullanarak atomistik simülasyonlar yoluyla anlaşılabilir, bu da moleküler dinamik olarak bilinir. Bir sistemin zaman evrimi, yapısını ve yapıya bağımlı özelliklerini anlamak için kullanılabilir. Ancak, camsı sistemlerin üretimi zamanla yavaş ve bu sistemleri anlamamızı zorlaştırır. Camın gerçekçi bir şekilde simüle edilmesinin bir yolu, sisteme termostatlar uygulayarak ısıtma-soğutma yöntemini gerçekleştirebilmemizdir. Üretimden sonra, bazı özellikler atomistik yörüngelerine dayalı olarak incelenebilir, örneğin termal iletkenlik ve titreşim gibi özellikler incelenebilir. Ancak, klasik yaklaşım bazı özellikler için yeterli değildir, örneğin elektronik ve optik özelliklerin hesaplanması için zorunlu kuantum düzeltmeleri nedeniyle, ve özellikle düşük sıcaklık hesaplamaları için. Bu nedenle, elektron seviyesinde daha derin bir yaklaşım kullandık. Her iki yaklaşımın da kendi avantajları ve dezavantajları vardır. Klasik yaklaşımda atomların yörüngelerini izlemeleri için atomlar üzerinde etki eden bir atomlar arası tanımlanması gereken potansiyel problemimiz var. Kullanılan potansiyeller çoğunlukla deneysel sonuçlara dayalı ampirik veya yarı ampiriktir ve çoğunlukla sınırlıdır. Öte yandan, kuantum düzeltmelerini içeren bir yaklaşım yüzlerce atomdan oluşan sınırlı bir sistem boyutu gerektirir. Bu da gerçekçi bir malzeme boyutundan oldukça uzaktır. Bu noktada, bir referans hesaplama iki yöntem arasındaki transferi sağlar ve verimli bir şekilde amorf sistemlerin daha geniş özellik analizine izin verir. Bu tezde, ben ilk olarak cam üretimi için referans hesaplamalara odaklandım. Sistemler arasında uyumlu bir yöntem elde ettikten sonra, her iki yaklaşımın güçlerini kullanarak özellik analizi yapıldı. Hem 3D hem de düşük boyutlu (2D) amorf yapıları inceledik. Özellikle metalik camlara

## Fonksiyonelleştirilebilen gelecek amorf malzemeler



## Kristal devre elemanlarına alternatif olarak

Figure 11.1. Amorf yapılar (camlar), üç boyutlu (örneğin, metalik camlar (MG'ler)) ile düşük boyutlu yapılar (örneğin, katmanlı yapılar ve iki boyutlu (2D) yapılar) arasında işlevselleştirilebilirlikleri ile kristal karşılıklarına gelecekte bir alternatiftir. Amorf yapılar dayanıklılıkları ve düşük ısı iletkenlikleri ile bilinirler. Gösterilen örnekler de metalik ancak termal olarak düşük iletkenlerdir, bu da cihaz uygulamalarında ısıdan muzdarip kristal metallerden daha avantajlıdır.



(MG) odaklandık. MG'ler termal olarak düşük iletkenlerdir ve termoelektrik modüllerde kullanılır. Isı, tüm elektronik cihazlarda cihaz verimliliğini, dayanıklılığını ve ömrünü sınırlayan en büyük sorunlardan biridir. Bu nedenle, MG'ler kullanılarak endüstrilerde cihaz verimliliğini, dayanıklılığını ve aynı zamanda ömrünü artırmak için yeni malzemeler geliştirmek ve/veya malzemelerin işlevselleştirilmesine odaklanmaktadır. İlk makalede,  $\text{Fe}_{0.85}\text{Zr}_{0.15}$  MG'nin termal iletkenliğini nano yapılar ve basınç ile ayarlamaya odaklandık. Bu çalışmada, önerilen boşluk boyutuna bağlı cam termal iletkenlik elde etme modelini kullanarak kafes termal iletkenliklerinin ayarlanabileceği gösterilmiştir. Ayrıca, çalışılan cam yapısının genel özelliklerine yerel yapıların etkisine de odaklandık. İkinci makalede, deneysel olarak elde edilen CoZr MG'nin doyma mıknatıslanmasına odaklandık, bu da Co atomlarının yapıdaki derişiminden etkilenir. Teorik ve deneysel olarak elde edilen sonuçlar, yapıların manyetik özellikleri belirlediğini ve bu kısa-orta menzilli bir düzenleme etkisini içerebileceğini göstermektedir. Benzer şekilde, üçüncü makalede MoGe MG'de yapıya bağımlı süperiletkenlik elde edilmiştir. MG'ye ek olarak, dördüncü ve beşinci makalelerde özellikler üzerinde boyut etkisini gösteriyoruz. Dördüncü makalede, grafenin elastik modülündeki azalma, bağ enerjisi azalmasına neden olan düzenli bir fazdan düzensiz bir faza yapısal bir deęişiklik olarak açıklanmaktadır. Beşinci makalede, hem 2D hem de katmanlı grafen, silisen ve silikon karbürün yapısal, termal, titreşimli, elektronik ve optik özellikleri ayrıntılı olarak tartışılmaktadır. Bu yapılar metalik elektronik özelliklere ve düzensiz bir yük dağılımına sahip olarak bulunmuştur, bu da gaz sensörleri gibi belirli uygulamalar için işlevselleştirilebilirliklerini artırabilir. Düşük termal iletkenlikleri ile birlikte gelecekteki elektronik, optoelektronik ve dięer birçok alanda kristal karşılıklarına alternatif malzemeler olarak kullanılabilirler. Son olarak önemli noktalaradan biri, amorf malzemelerin yapıya bağımlı özellikleri ve işlevsel cihazlardaki potansiyel uygulamaları hakkında hala keşfedilecek ve öğretilcek çok şey var.

## 12. Acknowledgements

I would like to express my sincerest appreciation to my supervisor, Biplab Sanyal, for his unwavering support, guidance, and mentorship throughout my Ph.D. journey. I have learned a great deal from his expertise and knowledge, and it has been a privilege to work in his group. I would also like to thank my co-advisor, Peter Broqvist, for his support. I am deeply grateful to Olle Eriksson for believing in me and supporting me. This thesis would not have been possible without Biplab and Olle.

I would also like to acknowledge my collaborators Ivan, Sukanya, Parul, Hu, Ersoy, and Murat who have collaborated with me on various projects during my PhD. I would like to thank my senior collaborators Gabriella Andersson, Björgvin Hjörvarsson, Klaus Leifer, Iosif Galanakis, and Ingrid Mertig. I have enjoyed being part of the Sanyal group and would like to thank the group members Sukanya, Masoumeh, Soheil, Suhas, and Duo. Thank you all for the fruitful discussions and collaborations.

I would also like to express my thanks to Ersoy Şaşıoğlu for his collaboration, scientific guidance, and assistance in proofreading this thesis. I would like to express my gratitude to Oscar Grånäs for his invaluable contributions to the Swedish summary of this thesis. I would also like to thank my previous advisors Engin Durgun and Salim Çiracı.

I would like to thank all members of the Materials Theory Division for the friendly atmosphere. It was a pleasure to be the Fika organizer and to connect with everyone in the division for more than a year until the Covid-19 pandemic. I would like to thank all lunch and coffee group members for the interesting talks and laughs. I am especially grateful to one of my best friends, Erna; we have shared many things over the years. Your support and friendship are priceless, and I will always have two extra plates for you and Lorand; there are many foods to enjoy. I have had many office mates and would like to thank all of you for the shared memories. I also want to say my sincere thanks to my final officemate, XiaoYong Yang, for her friendship, lunch memories, and for proofreading my thesis. I would like to thank all of my friends in Uppsala. In particular, I thank Seda for our priceless friendship. I would also like to thank my neighbor Claudia for her support and neighborhood; I am happy to have met her.

My heartfelt thanks to my son Kont, who was my constant source of love, support, and inspiration. Though I lost him while I was writing this thesis, he was my biggest motivation to finish it and dedicate it to him. Your loyalty, emotional support, and patience were my guiding lights during the darkest of

times. I am forever grateful for the privilege of being his mother and for the precious moments, we shared. Thank you for everything, my sweet baby. I will always love you and cherish our memories until we meet again in heaven.

I want to express my appreciation to Merve Aydınlı for her expertise, priceless support, and suggestions for Kont even from miles away. I would also like to thank Betül Bilgebey for almost 20 years of friendship. I am grateful to you two for your unwavering support, and long phone calls whenever I needed you (especially regarding Kont).

Last, but not least, I would like to thank my mother Fatma Özer Gürbüz for her support and patience. Thank you for being everything to me along with Kont... I must say that you did a great job with the corrections to this thesis, mommy. With this thesis, I have fulfilled my promise to my grandfather, İbrahim Özer; Rest in peace, my lovely grandpa.

# Bibliography

- [1] S. R. Elliott. Physics of amorphous materials. In *Physics of amorphous materials*, pages 58–64. Longman Group Ltd., first edition edition, 1985.
- [2] F. Bouchy, S. Udry, M. Mayor, C. Moutou, F. Pont, N. Iribarne, R. Da Silva, S. Illovaisky, D. Queloz, N. C. Santos, D. Ségransan, and S. Zucker. Elodie metallicity-biased search for transiting hot jupiters - ii. a very hot jupiter transiting the bright k star hd733. *A&A*, 444(1):L15–L19, 2005.
- [3] Gaia Collaboration, Brown, A. G. A., and et al. Gaia data release 2 - summary of the contents and survey properties. *A&A*, 616:A1, 2018.
- [4] W.-J. Joo, J.-H. Lee, Y. Jang, S.-G. Kang, Y.-N. Kwon, J. Chung, S. Lee, C. Kim, T.-H. Kim, C.-W. Yang, U. J. Kim, B. L. Choi, D. Whang, and S.-W. Hwang. Realization of continuous zachariasencarbon monolayer. *Sci. Adv.*, 3:1601821, 2017.
- [5] L. Lichtenstein, M. Heyde, and H.-J. Freund. Crystalline-vitreous interface in two dimensional silica. *Phys. Rev. Lett.*, 109:106101, Sep 2012.
- [6] L. Lichtenstein, M. Heyde, and H.-J. Freund. Atomic arrangement in two-dimensional silica: From crystalline to vitreous structures. *The Journal of Physical Chemistry C*, 116(38):20426–20432, 2012.
- [7] L. Lichtenstein, C. Büchner, B. Yang, S. Shaikhutdinov, M. Heyde, M. Sierka, R. Włodarczyk, J. Sauer, and H.-J. Freund. The atomic structure of a metal-supported vitreous thin silica film. *Angewandte Chemie International Edition*, 51(2):404–407, 2012.
- [8] W. Jr. Klement, R. H. Willens, and P. Duwez. Non-crystalline structure in solidified gold–silicon alloys. *Nature*, 187:869, 1960.
- [9] Y. Liu, J. Liu, S. Sohn, Y. Li, J. J. Cha, and J. Schroers. Metallic glass nanostructures of tunable shape and composition. *Nat. Commun.*, 6:7043, 2015.
- [10] G. Kumar, A. Desai, and J. Schroers. Bulk metallic glass: The smaller the better. *Adv. Mater.*, 23:461, 2011.
- [11] M. Chen. A brief overview of bulk metallic glasses. *NPG Asia Mater*, 3:82, 2011.
- [12] H. J. Fecht, G. Han, Z. Fu, and W. L. Johnson. Metastable phase formation in the zr-al binary system induced by mechanical alloying. *J. Appl. Phys.*, 67:1744, 1990.
- [13] M. D. Demetriou, M. E. Launey, G. Garrett, D. C. Schramm, J. Pand Hofmann, W. L. Johnson, and R. O. Ritchie. A damage-tolerant glass. *Nat. Mater.*, 10:123, 2011.
- [14] W. Zhou, Y. Cheng, K. Chen, G. Xie, T. Wang, and G. Zhang. Thermal conductivity of amorphous materials. *Adv. Func. Mater.*, 30:1903829, 2020.
- [15] J. Song, X. Feng, and Y. Huang. Mechanics and thermal management of stretchable inorganic electronics. *Natl. Sci. Rev.*, 3:128, 11 2016.

- [16] S.-H. Bae, R. Shabani, J.-B. Lee, S.-J. Baeck, H. J. Cho, and J.-H. Ahn. Fully current-based sub-bandgap optoelectronic differential ideality factor technique and extraction of subgap dos in amorphous semiconductor tfts. *IEEE Trans. Electron Devices*, 61:3566, 10 2014.
- [17] K.-H. Kim, S. Hyun Jo, S. Gaba, and W. Lu. Nanoscale resistive memory with intrinsic diode characteristics and long endurance. *Appl. Phys. Lett.*, 96:053106, 2 2010.
- [18] Y. Lu, A. Alvarez, C.-H. Kao, J.-S. Bow, S.-Y. Chen, and I.-W. Chen. An electronic silicon-based memristor with a high switching uniformity. *Nat. Electron*, 2:66, 2 2019.
- [19] A. P. Gonçalves, E. B. Lopes, O. Rouleau, and C. Godart. Conducting glasses as new potential thermoelectric materials: the cu–ge–te case. *J. Mater. Chem.*, 20:1516, 2010.
- [20] M. Yamasaki, S. Kagao, and Y. Kawamura. Thermal diffusivity and conductivity of  $\text{Zr}_{55}\text{Al}_{10}\text{Ni}_5\text{Cu}_{30}$  bulk metallic glass. *Scr. Mater.*, 53:63, 2005.
- [21] C.-C. Yu, H.-J. Wu, P.-Y. Deng, M. T. Agne, G. J. Snyder, and J. P. Chu. Thin-film metallic glass: an effective diffusion barrier for se-doped agsbte<sub>2</sub> thermoelectric modules. *Sci. Rep.*, 7:45177, 2017.
- [22] R. Y. Umetsu, R. Tu, and T. Goto. Thermal and electrical transport properties of zr-based bulk metallic glassy alloys with high glass-forming ability. *Mater. Trans.*, 53:1721, 2012.
- [23] K. A. Thórarinsdóttir, N. Strandqvist, V. V. Sigurjónsdóttir, E. B. Thorsteinsson, B. Hjörvarsson, and F. Magnus. Finding order in disorder: Magnetic coupling distributions and competing anisotropies in an amorphous metal alloy. *APL Materials*, 10(4):041103, 2022.
- [24] X. F. Yao, J. P. Wang, T. J. Zhou, and T. C. Chong. Microstructure and magnetic properties of CoZr thin film. *Journal of applied physics*, 93(10):8310–8312, 2003.
- [25] H. Kim, A. Ghimire, S. Jamali, T. K. Djidjou, J. M. Gerton, and A. Rogachev. Effect of magnetic gd impurities on the superconducting state of amorphous mo-ge thin films with different thickness and morphology. *Phys. Rev. B*, 86:024518, Jul 2012.
- [26] H. Kim, S. Jamali, and A. Rogachev. Superconductor-insulator transition in long mo-ge nanowires. *Phys. Rev. Lett.*, 109:027002, Jul 2012.
- [27] C. T. Pan, J. A. Hinks, Q. M. Ramasse, G. Greaves, U. Bangert, S. E. Donnelly, and S. J. Haigh. In-situ observation and atomic resolution imaging of the ion irradiation induced amorphisation of graphene. *Sci. Rep.*, 4:6334, 2014.
- [28] C.-H. Toh, H. Zhang, J. Lin, A. S. Mayorov, Y.-P. Wang, C. M. Orofeo, D. B. Ferry, H. Andersen, N. Kakenov, Z. Guo, I. H. Abidi, H. Sims, K. Suenaga, S. T. Pantelides, and Özyilmaz B. Synthesis and properties of free-standing monolayer amorphous carbon. *Nature*, 577:199–203, 2020.
- [29] Z. Huang, T. Zhang, J. Liu, L. Zhang, Y. Jin, J. Wang, K. Jiang, S. Fan, and Q. Li. Amorphous mos<sub>2</sub> photodetector with ultra-broadband response. *Appl. Electron. Mater.*, 1:1314–1321, 2019.
- [30] Z. Yang, J. Hao, S. Yuan, S. Lin, H. M. Yau, J. Dai, and S. P. Lau. Field-effect transistors based on amorphous black phosphorus ultrathin films by pulsed laser deposition. *Adv. Mater.*, 27:3748–3754, 2015.

- [31] K. K. Chattopadhyay, D. Banerjee, N. S. Das, and D. Sarkara. Easy synthesis of amorphous graphene and related hybrids for cold cathode application. *Carbon*, 72:4–14, 2014.
- [32] M. M. Bhunia, K. Panigrahi, S. Das, K. K. Chattopadhyay, and P. Chattopadhyay. Amorphous graphene – transformer oil nanofluids with superior thermal and insulating properties. *Carbon*, 139:1010–1019, 2018.
- [33] L. Wu, A. Longo, N. Y. Dzade, A. Sharma, M. M. R. M. Hendrix, A. A. Bol, N. H. de Leeuw, E. J. M. Hensen, and J. P. Hofmann. The origin of high activity of amorphous mos2 in the hydrogen evolution reaction. *Chem. Sus. Chem.*, 12:4383–4389, 2019.
- [34] W. Fu, S. Yang, H. Yang, B. Guo, and Z. Huang. 2d amorphous mos3 nanosheets with porous network structures for scavenging toxic metal ions from synthetic acid mine drainage. *J. Mater. Chem. A*, 7:18799–18806, 2019.
- [35] Y. He, L. Liu, C. Zhu, and et al. Amorphizing noble metal chalcogenide catalysts at the single-layer limit towards hydrogen production. *Nat. Catal.*, 5:212–221, 2022.
- [36] N. R. Glavin, C. Muratore, M. L. Jespersen, J. Hu, P. T. Hagerty, A. M. Hilton, and A. T. Blake. Amorphous boron nitride: A universal, ultrathin dielectric for 2d nanoelectronics. *Adv. Func. Mater.*, 26:2640–2647, 2016.
- [37] L. Antidormi, A. Colombo and S. Roche. Thermal transport in amorphous graphene with varying structural quality. *2D Mater.*, 8:015028, 2021.
- [38] T. Zhu and E. Ertekin. Phonons, localization, and thermal conductivity of diamond nanothreads and amorphous graphene. *Nano Lett.*, 16:4763–4772, 2016.
- [39] B. Mortazavi, Fan Z., L. F. C. Pereira, A. Harju, and T. Rabczuk. Amorphized graphene: A stiff material with low thermal conductivity. *Carbon*, 103:318–326, 2016.
- [40] B. Bhattarai, P. Biswas, R. Atta-Fynn, and D. A. Drabold. Amorphous graphene: a constituent part of low density amorphous carbon. *Phys. Chem. Chem. Phys.*, 20:19546–19551, 2018.
- [41] R. Ravinder, R. Kumar, Agarwal M., and N. M. A. Krishnan. Evidence of a two-dimensional glass transition in graphene: Insights from molecular simulations. *Sci. Rep.*, 9:4517, 2019.
- [42] F. R. Geder, J. Kotakoski, U. Kaiser, and J. C. Meyer. A journey from order to disorder-atom by atom transformation from graphene to a 2d carbon glass. *Sci. Rep.*, 4:4060, 2014.
- [43] V. V. Hoang and N. T. Long. Amorphous silicene—a view from molecular dynamics simulation. *J. Phys.: Condens. Matter*, 28:195401, 2016.
- [44] Y. Gao, Y. Zhou, X. Zhang, and M. Hu. Extremely low thermal conductivity of polycrystalline silicene. *J. Phys. Chem. C*, 122:9220–9228, 2018.
- [45] Y. Zhou and M. Hu. Record low thermal conductivity of polycrystalline si nanowire: Breaking the casimir limit by severe suppression of propagons. *Nano Lett.*, 16:6178–6187, 2016.
- [46] V. V. Hoang, N. H. Giang, and T. Q. Dong. Amorphous and ‘crystalline’ penta-silicene. *Philos. Mag.*, 100:1962–1981, 2020.
- [47] N. T. Long, H. A. Huy, T. Q. Tuan, O. K. Le, V. V. Hoang, and Giang N. H. Crystallization of supercooled liquid and amorphous silicene. *J. Non-Cryst.*

- Solids*, 487:87–95, 2018.
- [48] H. A. Huy, L. T. Nguyen, D. L. T. Nguyen, T. Q. Truong, L. K. Ong, V. V. Hoang, and Giang N. H. Novel pressure-induced topological phase transitions of supercooled liquid and amorphous silicene. *J. Phys.: Condens. Matter*, 31:095403, 2019.
  - [49] M. Li and Y. Yue. A molecular dynamics study of thermal transport in amorphous silicon carbide thin film. *RSC Adv.*, 4:23010–23016, 2014.
  - [50] D. T. N. Tranh, V. V. Hoang, and T. T. T. Hanh. Modeling glassy sic nanoribbon by rapidly cooling from the liquid: An affirmation of appropriate potentials. *Phys. B: Condens. Matter*, 608:412746, 2021.
  - [51] V. V. Hoang, N. H. Giang, T. Q. Dong, and V. Bubanja. Atomic structure and rippling of amorphous two-dimensional sic nanoribbons – md simulations. *Comput. Mater. Sci.*, 203:111123, 2022.
  - [52] N. H. Giang and V. V. Hoang. Influences of cooling rate on formation of amorphous germanene. *Physica E Low Dimens. Syst. Nanostruct.*, 126:114492, 2021.
  - [53] M. Durandurdu. Hexagonal nanosheets in amorphous bn: A first principles study. *J. Non-Cryst. Solids*, 427:41–45, 2015.
  - [54] Y.Q. Cheng and E. Ma. Atomic-level structure and structure–property relationship in metallic glasses. *Progress in Materials Science*, 56(4):379–473, 2011.
  - [55] J. Schroers. Flying to the bottom. *Physics Today*, 66:32, 2013.
  - [56] G. Parisi and F. Scortino. Flying to the bottom. *Nat. Mater*, 12:94, 2013.
  - [57] P. G. Debenedetti and F. H. Stillinger. Supercooled liquids and the glass transition. *Nature*, 410:259, 2001.
  - [58] W. Klement Jun, R. H. Willens, and P. Duwez. Non-crystalline structure in solidified gold–silicon alloys. *Nature*, 187:869–870, 1960.
  - [59] N. Amigo, P. Cortes, and F.J. Valencia. Research on metallic glasses at the atomic scale: a systematic review. *SN Appl. Sci.*, 4:281, 2022.
  - [60] J. Cai and Y. Y. Ye. Simple analytical embedded-atom-potential model including a long-range force for fcc metals and their alloys. *Phys. Rev. B*, 54:8398–8410, Sep 1996.
  - [61] J. Tersoff. New empirical approach for the structure and energy of covalent systems. *Phys. Rev. B*, 37:6991–7000, Apr 1988.
  - [62] M. I. Mendelev, M. J. Kramer, Ott R. T., D. J. Sordelet, D. Yagodin, and P. Popel. Development of suitable interatomic potentials for simulation of liquid and amorphous cu–zr alloys. *Philosophical Magazine*, 89(11):967–987, 2009.
  - [63] S. Plimpton. Fast parallel algorithms for short-range molecular-dynamics. *J. Comput. Phys.*, 117:1, 1995.
  - [64] G. Kresse and J. Furthmüller. Efficiency of ab-initio total energy calculations for metals and semiconductors using a plane-wave basis set. *Comput. Mater. Sci.*, 6:15, 1996.
  - [65] E. Takeshi and S. J.L. Billinge. Chapter 3 - the method of total scattering and atomic pair distribution function analysis. In T. Egami and Billinge S. J.L., editors, *Underneath the Bragg Peaks*, volume 16 of *Pergamon Materials Series*, pages 55–111. Pergamon, 2012.

- [66] A.M. Ovrutsky, A.S. Prokhoda, and M.S. Rasshchupkyna. 6 - simulation techniques for atomic systems. In *Computational Materials Science*, pages 151–186. Elsevier, Oxford, 2014.
- [67] X. J. Liu, Y. Xu, X. Hui, Z. P. Lu, F. Li, G. L. Chen, J. Lu, and C. T. Liu. Metallic liquids and glasses: Atomic order and global packing. *Phys. Rev. Lett.*, 105:155501, Oct 2010.
- [68] V. P. Voloshin and Yu. I. Naberukhin. On the origin of the splitting of the second maximum in the radial distribution function of amorphous solids. *J Struct Chem*, 38:62–70, 1997.
- [69] P. Häussler. Interrelations between atomic and electronic structures-liquid and amorphous metals as model systems. *Physics Reports*, 222(2):65–143, 1992.
- [70] G. Voronoi. Nouvelles applications des paramètres continus à la théorie des formes quadratiques. deuxième mémoire. recherches sur les paralléloèdres primitifs. *Journal für die reine und angewandte Mathematik (Crelles Journal)*, 1908(134):198–287, 1908.
- [71] C. H. Rycroft. VORO++: A three-dimensional Voronoi cell library in C++. *Chaos: An Interdisciplinary Journal of Nonlinear Science*, 19(4), 10 2009. 041111.
- [72] H.W. Sheng, Y.Q. Cheng, P.L. Lee, S.D. Shastri, and E. Ma. Atomic packing in multicomponent aluminum-based metallic glasses. *Acta Materialia*, 56(20):6264–6272, 2008.
- [73] X. Yuan and A.N. Cormack. Efficient algorithm for primitive ring statistics in topological networks. *Computational Materials Science*, 24(3):343–360, 2002.
- [74] J. M. Haile. Molecular dynamics simulations, elementary methods. In *Molecular Dynamics Simulations, Elementary Methods*. Wiley, first edition edition, 1992.
- [75] W. C. Swope, H. C. Andersen, P. H. Berens, and K.R. Wilson. A computer simulation method for the calculation of equilibrium constants for the formation of physical clusters of molecules: Application to small water clusters. *The Journal of Chemical Physics*, 76(1):637–649, 01 1982.
- [76] D. Frenkel and B. Smit. Understanding molecular simulation: From algorithms to applications. *Academic Press*, 2nd edition, 2007.
- [77] H. J. C. Berendsen, J. P. M. Postma, W.F. van Gunsteren, A. Dinola, and J. R. Haak. Molecular-dynamics with coupling to an external bath. *J. Chem. Phys.*, 81:3684, 1984.
- [78] S. Munetoh, M. Teruaki, K. Moriguchi, and A. Shintani. Interatomic potential for si-o systems using tersoff parameterization. *Computational Materials Science*, 39(2):334–339, 2007.
- [79] R. Kubo. Statistical-mechanical theory of irreversible processes .1. general theory and simple applications to magnetic and conduction problems. *J. Phys. Soc. Jpn.*, 12:570, 1957.
- [80] R. Zwanzig. Time-correlation functions and transport coefficients in statistical mechanics. *Annu. Rev. Phys. Chem.*, 16:67, 1965.
- [81] J. Kang and L.-W. Wang. First-principles green-kubo method for thermal conductivity calculations. *Phys. Rev. B*, 96:020302, 7 2017.
- [82] P. K. Schelling, S. R. Phillpot, and P. Keblinski. Comparison of atomic-level simulation methods for computing thermal conductivity. *Phys. Rev. B*,



- 65:144306, 4 2002.
- [83] S. Gonçalves and H. Bonadeo. Vibrational densities of states from molecular-dynamics calculations. *Phys. Rev. B*, 46:12019–12021, Nov 1992.
  - [84] P. B. Allen, J. L. Feldman, J. Fabian, and F. Wooten. Diffusons, locons and propagons: Character of atomic vibrations in amorphous si. *Philosophical Magazine B*, 79(11-12):1715–1731, 1999.
  - [85] M. Zhou, T. Liang, B. Wu, J. Liu, and P. Zhang. Phonon transport in antisite-substituted hexagonal boron nitride nanosheets: A molecular dynamics study. *Journal of Applied Physics*, 128(23), 12 2020. 234304.
  - [86] P. Hohenberg and W. Kohn. Inhomogeneous electron gas. *Phys. Rev.*, 136:B864, 1964.
  - [87] W. Kohn and L. J. Sham. Self-consistent equations including exchange and correlation effects. *Phys. Rev.*, 140:A1133, 1965.
  - [88] M. Levy. Electron densities in search of hamiltonians. *Phys. Rev. A*, 26:1200, 1982.
  - [89] T. Kaewmaraya. First-principles studies of materials properties. *Uppsala University*, 2015.
  - [90] J. P. Perdew, K. Burke, and M. Ernzerhof. Generalized gradient approximation made simple. *Phys. Rev. Lett.*, 77:3865–3868, 10 1996.
  - [91] D. Vanderbilt. Soft self-consistent pseudopotentials in a generalized eigenvalue formalism. *Phys. Rev. B*, 41:7892, 1990.
  - [92] P. E. Blöchl. Projector augmented-wave method. *Phys. Rev. B*, 50:17953–17979, 12 1994.
  - [93] R. P. Feynman. Forces in molecules. *Phys. Rev.*, 56:340–343, Aug 1939.
  - [94] S. Grimme, J. Antony, S. Ehrlich, and S. Krieg. A consistent and accurate ab initio parametrization of density functional dispersion correction (dft-d) for the 94 elements h-pu. *J. Chem. Phys.*, 132:154104, 2010.
  - [95] S. Grimme, S. Ehrlich, and L. Goerigk. Effect of the damping function in dispersion corrected density functional theory. *J. Comp. Chem.*, 32:1456, 2011.
  - [96] S. Grimme. Semiempirical gga-type density functional constructed with a long-range dispersion correction. *J. Comp. Chem.*, 27:1787, 2006.
  - [97] A. Tkatchenko and M. Scheffler. Accurate molecular van der waals interactions from ground-state electron density and free-atom reference data. *Phys. Rev. Lett.*, 102:073005, 2009.
  - [98] M. Nishiwaki and H. Fujiwara. Highly accurate prediction of material optical properties based on density functional theory. *Computational Materials Science*, 172:109315, 2020.
  - [99] K. Harun, N. A. Salleh, B. Deghfel, M. K. Yaakob, and A. A. Mohamad. Dft + u calculations for electronic, structural, and optical properties of zno wurtzite structure: A review. *Results in Physics*, 16:102829, 2020.
  - [100] S. J. Yadav, J. Jasani, D. V. Shah, and Y. Sonvane. Study of optical and elastic properties of fe<sub>3</sub>se<sub>4</sub> through dft. *Materials Today: Proceedings*, 2023.
  - [101] M. Gajdoš, K. Hummer, G. Kresse, J. Furthmüller, and F. Bechstedt. Linear optical properties in the projector-augmented wave methodology. *Phys. Rev. B*, 73:045112, Jan 2006.
  - [102] S. Shahrokhi and C. Leonard. Tuning the band gap and optical spectra of silicon-doped graphene: Many-body effects and excitonic states. *Journal of*

- Alloys and Compounds*, 693:1185–1196, 2017.
- [103] N. G. Dou, R. A. Jagt, C. M. Portela, J. R. Greer, and A. J. Minnich. Ultralow thermal conductivity and mechanical resilience of architected nanolattices. *Nano Lett.*, 18:4755, 7 2018.
  - [104] D. S. Mukhopadhyay, S. and Parker, B. C. Sales, A. A. Puretzky, M. A. McGuire, and L. Lindsay. Two-channel model for ultralow thermal conductivity of crystalline  $\text{tl}_3\text{vse}_4$ . *Science*, 360:1455, 6 2018.
  - [105] W.-X. Zhou and K.-Q. Chen. First-principles determination of ultralow thermal conductivity of monolayer  $\text{wse}_2$ . *Sci. Rep.*, 5:15070, 10 2015.
  - [106] F. DeAngelis, M. G. Muraleedharan, J. Moon, R. S. Seyf, A. J. Minnich, A. J. H. McGaughey, and H. Asegun. Thermal transport in disordered materials. *NANOSC. MICROSC. THERM. ENG*, 23:81, 12 2019.
  - [107] R. S. Seyf, A. J. H. McGaughey, and H. Asegun. A method for distinguishing between propagons, diffusions, and locons. *J. Appl. Phys.*, 120:025101, 5 2016.
  - [108] L. Yang, H. Y. Li, P. W. Wang, S. Y. Wu, G. Q. Guo, B. Liao, Q. L. Guo, X. Q. Fan, P. Huang, H. B. Lou, F. M. Guo, Q. S. Zeng, T. Sun, Y. Ren, and L. Y. Chen. Structural responses of metallic glasses under neutron irradiation. *Sci. Rep.*, 7:16739, 2017.
  - [109] C. C. Wang, K. J. Dong, and A. B. Yu. Analysis of voronoi clusters in the packing of uniform spheres. *AIP Conference Proceedings*, 1542:353, 2013.
  - [110] F. C. Li, T. Liu, J. Y. Zhang, S. Shuang, Q. Wang, A. D. Wang, J. G. Wang, and Y. Yang. Amorphous-nanocrystalline alloys: Fabrication, properties, and applications. *Materials Today Advances*, 4:100027, 2019.
  - [111] C. Li, A. J. Freeman, and C. L. Fu. Electronic structure and magnetic properties of the hcp Co (0001) surface. *Journal of magnetism and magnetic materials*, 94(1-2):134–140, 1991.
  - [112] B. Wiendlocha, J. Tobola, and S. Kaprzyk. Search for  $\text{sc}_3x\text{B}$  ( $x = \text{In, Tl, Ga, Al}$ ) perovskites superconductors and proximity of weak ferromagnetism. *Phys. Rev. B*, 73:134522, Apr 2006.
  - [113] W. L. McMillan. Transition temperature of strong-coupled superconductors. *Phys. Rev.*, 167:331–344, Mar 1968.
  - [114] D. A. Papaconstantopoulos, M. J. Mehl, and P.-H. Chang. High-temperature superconductivity in  $\text{lah}_{10}$ . *Phys. Rev. B*, 101:060506, Feb 2020.
  - [115] O. Krogh Andersen. Linear methods in band theory. *Phys. Rev. B*, 12:3060–3083, Oct 1975.
  - [116] M. Gurvitch, A. K. Ghosh, B. L. Gyorffy, H. Lutz, O. F. Kammerer, J. S. Rosner, and Myron Strongin. Effects of disorder on the transition temperature and transport properties of a low- $T_c$   $a15$  superconductor:  $\text{mo}_3\text{ge}$ . *Phys. Rev. Lett.*, 41:1616–1619, Dec 1978.
  - [117] George F. Hardy and John K. Hulm. The superconductivity of some transition metal compounds. *Phys. Rev.*, 93:1004–1016, Mar 1954.
  - [118] W. H. Butler. Electron-phonon coupling in the transition metals: Electronic aspects. *Phys. Rev. B*, 15:5267–5282, Jun 1977.
  - [119] B. T. Matthias. Empirical relation between superconductivity and the number of valence electrons per atom. *Phys. Rev.*, 97:74–76, Jan 1955.
  - [120] A. H. Castro Neto, F. Guinea, N. M. R. Peres, K. S. Novoselov, and A. K.

- Geim. The electronic properties of graphene. *Rev. Mod. Phys.*, 81:109–162, Jan 2009.
- [121] D. Berman, S. A. Deshmukh, S. K. R. S. Sankaranarayanan, A. Erdemir, and A. V. Sumant. Macroscale superlubricity enabled by graphene nanoscroll formation. *Science*, 348(6239):1118–1122, 2015.
  - [122] S. P. Koenig, N. G. Boddeti, M. L. Dunn, and J. S. Bunch. Ultrastrong adhesion of graphene membranes. *Nature Nanotechnology*, 6:543–546, 2011.
  - [123] S. M. Hollen and J. A. Gupta. Painting magnetism on a canvas of graphene. *Science*, 352(6284):415–416, 2016.
  - [124] A. Lundstedt, R. Papadakis, H. Li, Y. Han, K. Jorner, J. Bergman, K. Leifer, H. Grennberg, and H. Ottosson. White-light photoassisted covalent functionalization of graphene using 2-propanol. *Small Methods*, 1(11):1700214, 2017.
  - [125] H. Li, R. Papadakis, S. H. M. Jafri, T. Thersleff, J. Michler, and K. Ottosson, H. Leifer. Superior adhesion of graphene nanoscrolls. *Communications Physics*, 1:44, 2018.
  - [126] I. H. Wani, S. H. M. Jafri, J. Wani, A. Hayat, H. Li, V. A. Shukla, A. Orthaber, A. Grigoriev, R. Ahuja, and K. Leifer. A sub 20 nm metal-conjugated molecule junction acting as a nitrogen dioxide sensor. *Nanoscale*, 11:6571–6575, 2019.
  - [127] H. Li, T. Duan, S. Haldar, B. Sanyal, O. Eriksson, H. Jafri, S. Hajjar-Garreau, L. Simon, and K. Leifer. Direct writing of lateral fluorographene nanopatterns with tunable bandgaps and its application in new generation of moiré superlattice. *Applied Physics Reviews*, 7(1):011403, 01 2020.
  - [128] H. Li, R. Papadakis, T. Hussain, A. Karton, and J. Liu. Moiré patterns arising from bilayer graphone/graphene superlattice. *Nano Research*, 13:1060–1064, 2020.
  - [129] H. Li, E. Gürbüz, S. Haldar, T. Hussain, X. Zheng, X. Ye, S. W. Makumi, T. Duan, S. H. M. Jafri, L. Daukiya, L. Simon, A. Karton, B. Sanyal, and K. Leifer. Observation of defect density dependent elastic modulus of graphene. *Applied Physics Letters*, 123(5):053102, 08 2023.
  - [130] C. D. Zeinalipour-Yazdi and C. Christofides. Linear correlation between binding energy and Young’s modulus in graphene nanoribbons. *Journal of Applied Physics*, 106(5):054318, 09 2009.
  - [131] C. Li, C. Zheng, F. Cao, Y. Zhang, and X. Xia. The development trend of graphene derivatives. *J. Electron. Mater.*, 51:4107–4114, 2022.
  - [132] S. Z. Butler, S. M. Hollen, L. Cao, Y. Cui, J. A. Gupta, H. M. Gutiérrez, T. F. Heinz, S. S. Hong, J. Huang, A. F. Ismach, E. Johnston-Halperin, M. Kuno, V. V. Plashnitsa, R. D. Robinson, R. S. Ruoff, S. Salahuddin, J. Shan, L. Shi, M. G. Spencer, M. Terrones, W. Windl, and J. E. Goldberger. Progress, challenges, and opportunities in two-dimensional materials beyond graphene. *ACS Nano*, 7:2898–2926, 2013.
  - [133] H. Zhang, M. Chhowalla, and Z. Liu. 2d nanomaterials: graphene and transition metal dichalcogenides. *Chem. Soc. Rev.*, 47:3015–3017, 2018.
  - [134] M. Polley, H. Fedderwitz, T. Balasubramanian, A. A. Zakharov, R. Yakimova, O. Bäcke, J. Ekman, S. P. Dash, S. Kubatkin, and S. Lara-Avila. Bottom-up growth of monolayer honeycomb sic. *Phys. Rev. Lett.*, 130:076203, 2023.
  - [135] X. Chen, F. Tian, C. Persson, W. Duan, and N.-X. Chen. Interlayer interactions

- in graphites. *Sci. Rep.*, 3:3046, 2013.
- [136] E. Mostaani, N. D. Drummond, and Fal’ko V. I. Quantum monte carlo calculation of the binding energy of bilayer graphene. *Phys. Rev. Lett.*, 115:115501, 2015.
- [137] A. Giri, C. J. Dionne, and P. E. Hopkins. Atomic coordination dictates vibrational characteristics and thermal conductivity in amorphous carbon. *Npj Comput. Mater.*, 8:55, 2022.
- [138] K. A. Thórarinsdóttir, H. Palonen, G. K. Pálsson, B. Hjörvarsson, and F. Magnus. Giant magnetic proximity effect in amorphous layered magnets. *Phys. Rev. Mater.*, 3:054409, May 2019.
- [139] Y. Xi, X. Jing, Z. Xu, N. Liu, Y. Liu, M.-L. Lim, M. Yang, Y. Sun, J. Zhuang, X. Xu, W. Hao, Y. Li, X. Li, X. Wei, P.-H. Tan, Q. Li, B. Liu, S. X. Dou, and Y. Du. Superconductivity in layered van der waals hydrogenated germanene at high pressure. *J. Am. Chem. Soc.*, 144:18887–18895, 2022.
- [140] G. Kresse and J. Hafner. Ab initio molecular-dynamics simulation of the liquid-metal–amorphous-semiconductor transition in germanium. *Phys. Rev. B*, 49:14251–14269, 5 1994.
- [141] G. Kresse and J. Furthmüller. Efficiency of ab-initio total energy calculations for metals and semiconductors using a plane-wave basis set. *Computational Materials Science*, 6(1):15–50, 1996.
- [142] J. P. Perdew, K. Burke, and M. Ernzerhof. Generalized gradient approximation made simple. *Phys. Rev. Lett.*, 77:3865–3868, 10 1996.
- [143] A. P. Thompson, S. J. Plimpton, and W. Mattson. General formulation of pressure and stress tensor for arbitrary many-body interaction potentials under periodic boundary conditions. *J. Chem. Phys.*, 131:154107, 2009.
- [144] R. Zallen. The physics of amorphous solids. *Wiley-VCH Weinheim*, 2004.
- [145] R. Jana, D. Savio, V. L. Deringer, and L. Pastewka. Structural and elastic properties of amorphous carbon from simulated quenching at low rates. *Modelling Simul. Mater. Sci. Eng.*, 27:085009, 2019.
- [146] A. Giri, B. F. Donovan, and P. E. Hopkins. Localization of vibrational modes leads to reduced thermal conductivity of amorphous heterostructures. *Phys. Rev. Materials*, 2:056002, 5 2018.
- [147] N. T. Tien, P. T. B. Thao, L. V. P. Thuan, and D. H. Chuong. First-principles study of electronic and optical properties of defective sawtooth penta-graphene nanoribbons. *Comput. Mater. Sci.*, 15:111065, 2022.
- [148] Y. Ding and Y. Wang. Hydrogen-induced stabilization and tunable electronic structures of penta-silicene: a computational study. *J. Mater. Chem. C*, 3:11341, 2015.
- [149] J. E. Padilha and R. B. Pontes. Free-standing bilayer silicene: The effect of stacking order on the structural, electronic, and transport properties. *J. Phys. Chem. C*, 119:3818–3825, 2015.
- [150] T. Susi, V. Skákalová, A. Mittelberger, P. Kotrusz, M. Hulman, T. J. Pennycook, C. Mangler, J. Kotakoski, and J. C. Meyer. Computational insights and the observation of sic nanograin assembly: towards 2d silicon carbide. *Sci. Rep.*, 7:4399, 2017.
- [151] M. C. Wingert, J. Zheng, S. Kwon, and R. Chen. Thermal transport in amorphous materials: a review. *Semicond. Sci. Technol.*, 31:113003, 2016.

- [152] S. Grimme, J. Antony, S. Ehrlich, and S. Krieg. A consistent and accurate ab initio parametrization of density functional dispersion correction (dft-d) for the 94 elements h-pu. *J. Chem. Phys.*, 132:154104, 2010.
- [153] F. R. Eder, J. Kotakoski, U. Kaiser, and J. C. Meyer. A journey from order to disorder — atom by atom transformation from graphene to a 2d carbon glass. *Sci. Rep.*, 4:4060, 2014.
- [154] S. R. Sellers, W. Man, S. Sahba, and M. Florescu. Local self-uniformity in photonic networks. *Nat. Commun.*, 8:14439, 2017.
- [155] H. Zhao, X. Chen, G. Wang, Y. Qui, and L. Guo. Two-dimensional amorphous nanomaterials: synthesis and applications. *2DMater.*, 6:032002, 2019.
- [156] Z. Yang, J. Hao, and S. P. Lau. Synthesis, properties, and applications of 2d amorphous inorganic materials. *J. Appl. Phys.*, 127:220901, 2020.
- [157] B. Özyilmaz, C.-T. Toh, H. Zhang, A. Mayorov, D. B. Ferry, H. Andersen, C. Cetin, and I. H. Abidi. Two dimensional amorphous carbon as overcoat for heat assisted magnetic recording media. *United States Patent Application Publication*, US 2019 / 0080713 A1, 2019.
- [158] R. A. Street. Technology and applications of amorphous silicon. *Springer*, 2000.
- [159] J. Tersoff. Chemical order in amorphous silicon carbide. *Phys. Rev. B*, 49:16349–16352, 1994.
- [160] K. S. Novoselov, A. Mishchenko, A. Carvalho, and A. H. Castro Neto. 2d materials and van der waals heterostructures. *Science*, 353:461, 2016.
- [161] D. L. Duong, S. J. Yun, and Y. H. Lee. van der waals layered materials: Opportunities and challenges. *ACS*, 11:11803–11830, 2017.
- [162] A. G. Marinopoulos, Lucia Reining, Angel Rubio, and Valerio Olevano. Ab initio study of the optical absorption and wave-vector-dependent dielectric response of graphite. *Phys. Rev. B*, 69:245419, Jun 2004.
- [163] M. L. Ould Ne, A. Abbasi, A. G. El hachimi, A. Benyoussef, H. Ez-Zahraouy, and A. El Kenz. Electronic optical, properties and widening band gap of graphene with ge doping. *Opt Quant Electron*, 49:218, 2017.
- [164] B. Mohan, A. Kumar, and P. K. Ahluwalia. A first principle calculation of electronic and dielectric properties of electrically gated low-buckled mono and bilayer silicene. *Physica E*, 53:233–239, 2013.
- [165] M. S. Shell. Principles of modern molecular simulation methods. *Lecture Notes*, 2012.

# Acta Universitatis Upsaliensis

*Digital Comprehensive Summaries of Uppsala Dissertations from the Faculty of Science and Technology 2287*

Editor: The Dean of the Faculty of Science and Technology

A doctoral dissertation from the Faculty of Science and Technology, Uppsala University, is usually a summary of a number of papers. A few copies of the complete dissertation are kept at major Swedish research libraries, while the summary alone is distributed internationally through the series Digital Comprehensive Summaries of Uppsala Dissertations from the Faculty of Science and Technology. (Prior to January, 2005, the series was published under the title "Comprehensive Summaries of Uppsala Dissertations from the Faculty of Science and Technology".)



Distribution: [publications.uu.se](http://publications.uu.se)  
urn:nbn:se:uu:diva-508514

ACTA UNIVERSITATIS  
UPSALIENSIS  
2023